PREVENTION AND MANAGEMENT OF WILDFIRES: VULNERABILITY MAPPING AND MACHINE LEARNING-BASED ALGORITHM DEVELOPMENT FOR FUEL MAPPING USING HYPERSPECTRAL IMAGERY

Thesis submitted in partial fulfilment of the requirements for the degree of Doctor of Philosophy in Energy and Environment (Science and Technology for the Industrial Innovation) at the Faculty of Engineering, La' Sapienza University of Rome, Italy

PhD Student

Riyaaz Uddien Shaik

Supervisor

Prof. Giovanni Laneve

XXXIV Cycle

Department of Astronautics Electrical and Energy Engineering (DIAEE)

La' Sapienza University of Rome, Italy

January 2022

CONTENTS

LIST OF FIGURES

LIST OF TABLES

LIST OF ACRONYMS

Acronym	Definition
HSI	Hyperspectral Imagery
PRISMA	PRecursore IperSpettrale della Missione Applicativa
ASI	Italian Space Agency
DEM	Digital Elevation Model
LUCAS	Land Use/Cover Area Frame Survey
GIS	Geographic Information System
JMSAM	Jeffries Matusita Spectral Angle Mapper
UNESCO	United Nations Educational, Scientific and Cultural Organization
RAS	Regional Administration of Sardinia
AVIRIS	Airborne Visible/Infrared Imaging Spectrometer
EO	Earth Observation

PUBLICATIONS

CONFERENCE PROCEEDINGS

[1] Riyaaz Uddien Shaik, Giovanni Laneve, Lorenzo Fusilli. 'New Approach of Sample Generation and Classification for Wildfire Fuel Mapping on Hyperspectral (PRISMA) Image'. IEEE International Geoscience and Remote Sensing Symposium 2021.

[2] Riyaaz Uddien Shaik, Valerio Pampanoni, Giovanni Laneve. 'Support Wildfire Management in Mediterranean Territories Using Multi-Source Satellite Data'. October 2019, 12th EARSeL eProceedings.

[3] Valerio Pampanoni, Riyaaz Uddien Shaik. 'Daily Fire Hazard Index for the Prevention and Management of Wildfires in the Region of Sardinia'. September 2019, AIDAA eProceedings, Rome, Italy.

[4] Riyaaz Uddien Shaik, Giovanni Laneve, Lorenzo Fusilli. 'Dynamic Wildfire Fuel Mapping Using Sentinel-2 and PRISMA Hyperspectral Imagery'. IEEE International Geoscience and Remote Sensing Symposium 2022.

JOURNAL ARTICLES

[1] Riyaaz Uddien Shaik, Giovanni Laneve, Lorenzo Fusilli. 'An Automatic Procedure for Forest Fire Fuel Mapping Using Hyperspectral (PRISMA) Imagery: A Semi-Supervised Classification Approach'. March 2022, Remote Sensing 14(5):1264.

[2] Riyaaz Uddien Shaik[#], Giovanni Laneve[#], Valerio Pampanoni[#]. 'The Daily Fire Hazard Index: A Fire Danger Rating Method for Mediterranean Areas'. July 2020, Remote Sensing 12(15): 2356.

ABSTRACT

Fire is a major ecological disturbance and threatening factor of ecosystem sustainability around the world and specifically in Mediterranean regions. Natural vegetation ecosystems are important environmental resources that provide various benefits to the human society whereas it also acts as fuel for wildfires. Hyperspectral imagery (HSI) is a passive technology which has the ability to classify the wildfire fuel types in a scene by means of several (hundreds) narrow band spectral acquisitions. This PhD thesis focused on developing a wildfire vulnerability map using GIS data for Sardinia and a procedure for wildfire fuel mapping using PRISMA HSI.

Firstly, wildfire vulnerability map was generated using the vulnerability index comprising of the three main components: exposure, sensitivity and coping capacity. Exposure, representing the presence of assets (people, property and ecosystems) in areas where wildfires occur. Sensitivity, representing the degree to which these assets can be affected by a wildfire, linked to their predisposition to suffer certain type and magnitude of losses. Coping capacity, related to the measures applied to anticipate potential effects or to respond in case of fire occurs, based on institutional practices within several countries. Composite indices for each of the components were created using GIS data of population density, fuel types, location of protected areas, roads infrastructure and surveillance activities, taking into account the effect of the third dimension wherever is necessary. The additive type model was selected for the aggregation of components by allocating weights in the order of importance, mainly to differentiate the effects of individual elements and to streamline the interpretation of the outputs. Specifically, non-coping capacity was improved by including road density along with other institutional variables such as firefighters and surveillance areas. The vulnerability map of Sardinia

developed by combining exposure map, sensitivity map and non-coping capacity map was shown. In this map, the value ranges from 0 to 1 representing from lower to higher vulnerable pixels correspondingly.

Secondly, a semi-supervised machine learning approach for discriminating the wildfire fuel types was developed for the hyperspectral imagery (HSI) of PRISMA, a recently launched satellite of Italian Space Agency. Though machine learning classifiers provide better accuracy comparatively, many remote sensing specialists hesitate to use them because of the unavailability of required datasets. So, here, a procedure was developed to generate samples using single spectral signature as input data point for each class to apply support vector machine classifier and followed by, unmixing of mixed pixels by fully constrained linear mixing model. The procedure developed for classifying the fuel types available in the image of south-west Sardinia covering a part of Monte-Arcosu Forest and 18 different fuel types were classified in this region of interest.

In order to correlate the classified fuel types to fuel models of Anderson or Scott/Burgan, further classification was carried out. Fuel types were classified according to the sparse/dense type, plain/mountainous type, open/closed type, and climatic conditions and for which available maps such as biomass, DEM, Tree Cover Density Map and iso-bioclimatic condition map were used respectively. Relative Greenness map was generated using time-series Sentinel-2 data. Then, the procedure of conversion from classified map to fuel map according to the JRC Anderson Codes and Scott/Burgan standard fuel models has been presented. The procedure was implemented on the HSI images obtained for south of Sardinian Island and for north-west of Latium in Italy as demonstration purpose. The classified map has been validated in different ways i.e. by using reference data, ground data and field data and obtained an overall accuracy of greater than 80% for all the cases. The stability of this approach was also tested by repeating the

procedure on another HSI obtained on Latium in Italy and obtained degree of confidence greater than 95%. The proposed approach in this work can be used to generate wildfire fuel map using hyperspectral (PRISMA) data with higher accuracy over any part of Europe using LUCAS points as input. SWOT analysis has been conducted to understand the Strengths, Weaknesses, Opportunities and Threats of PRISMA hyperspectral imagery for wildfire fuel mapping. Though it is not possible to overcome all the weaknesses and threats, strategies to overcome some of them were discussed.

Thus, the most vulnerable spots of wildfires can be referred using the developed vulnerability map whereas the wildfire fuels can be mapped-in for the areas of interest with hyperspectral image of PRISMA as per the proposed approach. Fuel map is useful to fire managers, researchers, policy makers and systems in applications such as study of fire behaviours, fire potential, fire emissions, carbon budget, fuel management, fire effects and ecosystem modelling. With this, it can be considered that this work has a major role in the prevention and management of wildfires.

Keywords: Wildfires; Vulnerability Map; Fuel Map; Machine Learning; Fuel Models;

INTRODUCTION

1.1. Overview on Wildfires

Fire is a significant ecological disturbance and threatening factor in ecosystem sustainability worldwide, specifically in Mediterranean regions. A researcher has considered the fire as the most giant "herbivore" on Earth with general dietary preferences (Bond and Keeley 2005). Fire occurs in variety of forms including high intensity crown fires to long-duration ground fires in organic soil with relatively low intensities (van der Werf et al. 2017). Fire regimes and ecosystems are rapidly changing at historically unprecedented rates. For example, fire activity has significantly increased in boreal forest ecosystems and declines in savannas (Veraverbeke et al. 2018a; Stavros et al. 2014; Dennison et al. 2006).

Fire is the main cause of forest destruction in the countries of the Mediterranean basin. The main reasons for the forest fires can be divided into two as natural (temperature, wind etc.,) and anthropogenic (human-made) causes. The predominating climatic conditions of the Mediterranean basin are significantly affecting the forest situation. Long summers (extending from June to October and sometimes even longer), with virtually no rain and average daytime temperatures well over 30°C, reduce the moisture content of forest litter to below 5%. Under these conditions, even a small addition of heat (a lightning, a spark, a match, a cigarette butt) can be enough to start a violent conflagration. Together with the heat and lack of moisture, wind is another influential climatic factor. The inland summer winds characterized by high speeds and strong desiccating power, for example, the mistral of France, the khamsin in Lebanon and Syria, the sirocco of Catalonia and Italy, the sharav in Israel, and the sirocco in the Maghreb, as well as the poniente in Valencia and the levante in the Straits of Gibraltar, cause atmospheric humidity to fall below 30% and contribute to the spread of fires by carrying sparks over great distances.

The dry and cold winds of the Mediterranean winters can also increase the danger of fire. For example, the foehn that blows southwards over the northern Italian Alps, and the southerly wind that blows across the north of Spain from the Central Meseta, often fan small, deliberately set fires out of control (Arbez, Birot, and Carnus 2002). For the anthropogenic, humans have become an increasingly important driver of fire occurrence (Bowman et al. 2011). Human activity has enhanced fire activity in locations such as deforestation zones, while fire suppression and conversion of fire prone landscapes such as savannas to agriculture in Africa, or of fire-maintained open lands to closed-canopy forests in the eastern US has generally decreased fire activity (van der Werf et al. 2017; Bowman et al. 2009).

The fire disturbance continuum discriminates between discrete temporal phases during which fire processes occur (Jain et al. 2004). The fire disturbance continuum includes pre-fire, active, and post-fire environments as shown in Fig 1. The pre-fire environment refers to the type, and condition of fuels as influenced by climate, weather and land management. The active fire environment is the phase during which fires spread over the landscape. Topography, fuels and fire weather influence active fire behavior and intensity. Fire intensity describes the physical combustion process of energy release from organic matter (Keeley 2009) and is directly related to fire emissions (Wooster et al. 2005). Finally, the post-fire environment is what is left after the fire is extinguished. The post-fire environment is often described interchangeably with the terms fire and burn severity (Boer et al. 2008; Keeley 2009). Here, we define fire severity as the degree of environmental change caused by a fire as evidenced immediately after the fire without recovery effects (Lentile et al. 2006; Morgan et al. 2014; Veraverbeke et al. 2018b). Conversely, burn severity gauges both the immediate fire-induced change and vegetation recovery. Fire and burn severity include fire effects on vegetation and soil (Morgan et al. 2014; Parsons et al. 2010).

Fig 1. Temporal phases in the fire disturbance continuum (Jain et al. 2004)

Over the last five decades, researchers have paid much attention to the ecological impacts of fire. The study of fire includes a broad spectrum of scientific disciplines including ecology, forestry, mechanical engineering (fire propagation patterns), atmospheric chemistry (gas emissions) and geography (spatial analysis of fire occurrence), to name just a few examples (Arroyo, Pascual, and Manzanera 2008). Fire behaviour helps determine the impact of fire to a more considerable extent. Fire behaviour is one of the reasons for causing different ecological impacts, and also it helps to determine the optimal suppression strategy for any given fire (Vakalis et al. 2004a, 2004b; Keramitsoglou et al. 2004; Whelan 2009). Fire intensity and rate of spread are two important determinants of fire behaviour that are affected, among other factors, by the fuel load, the type of fuel, and the fuel continuity (Whelan 2009). Fuel types vary with different species; for instance, *Pinus halepensis* is more flammable than others (Vakalis et al. 2004a) due to the highly flammable resins and oils content, producing high-intensity fires. At the same time, fuel continuity and fuel load relate to the percentage of the surface covered by vegetation, in other words, by potential fuels (Whelan 2009). The accuracy and effectiveness of any tool for simulation of fire behaviour or fire risk assessment depend on the accuracy and availability of data related to the vegetation ecosystem. Spatially and thematically

accurate vegetation cover is critical for the suppression and prevention of fire in fire-prone areas and ecosystems (Vakalis et al. 2004a, 2004b).

1.2. Forest as Fuels

As a reflection of the prevailing climate with its long summer droughts, Mediterranean forests are frequently characterized by fire climax species, i.e., those that depend on the presence of fire in their reproductive cycle (Aretano and Giovanni, 2015). Pines form the largest tree stands on both the northern and the southern shores of the Mediterranean. These species are characterized by physiological mechanisms that link natural seeding with fire, e.g., the opening of pine cones exposed to intense heat. These species also tend to have a particularly high content of resin or essential oils, making them extremely inflammable. Other species, particularly the evergreen sclerophyll oaks, have developed a morphological resistance to fire. For example, *Quercus Suber* has developed a characteristically thick bark that isolates the cambium, enabling it to resist sporadic fires. Likewise, the presence of a large number of dormant buds in oaks ensures the production of shoots and sprouts if the aerial part of the plant is reduced by fire. However, these adaptive reactions do not provide permanent protection. After repeated fires, the trees are replaced by a woody shrub cover that is not merely resistant to fire but typically pyrophytic, as with the dehiscence of rockroses (Cistus), or other species that produce seed with a thick isolating tegument or rhizomes or running roots. To this natural evolution of flora must be added human-induced changes caused by attempts to restore the tree cover in areas where excessive fire or other uses, such as overgrazing and fuelwood extraction, have caused a high level of degradation (Bonazountas and Toukiloglou, 2014). Reforestation is usually carried out using pioneer species, predominantly pines established in mono-species stands. This in itself increases the risk of fire due to the

continuity of fuels in closely spaced plantations as well as the concentration of fine, highly inflammable fuels (Arbez, Birot, and Carnus 2002).

1.3. Overview on Remote Sensing

The innate human desire to explore and understand the intangible pushes the boundaries of the scientific and technical limits, and is what made remote sensing the field of science of today. Aristotle, in De Anima, exposes the nature of light as a state of actual transparency in a potentially transparent medium and thus represents the necessary condition for vision. Eighteen hundred years after him, Leonardo da Vinci sets in detail the principles underlying the "camera obscura", while Isaac Newton, in 1666, using a prism proves that the light could be dispersed into a spectrum of colours, and using a second prism, the colour could be re-combined into white light, giving birth to the science and art of "drawing with light", broadly known as "photography". Not long after, the first photograph in history of humanity was taken by Niepce (1827), while Gaspard-Félix Tournachon (Nadar) took in 1858 the first aerial photograph from a balloon from an altitude of 1,200 feet over Paris. New methods and technologies for sensing of the Earth's surface going beyond the traditional black and white aerial photograph, required a new, more comprehensive term to be established. The term remote sensing came to fill in this gap, initially introduced in 1960. Remote Sensing (RS) is the field of science that includes all those activities necessary for the observation, acquisition and interpretation of information related to objects, events, phenomena or any other item under investigation, without making physical contact with the object, event, or phenomenon under investigation. Since the launch of the first satellite for space exploration (Sputnik-1) in the late fifties, advances in the satellite technology burst, offering a multitude of spaceborne and airborne platforms with on-board sensors able to detect a great number of heterogeneous sources of information, for the study

not only of distant celestial objects but also for the Earth Observation (EO) (J. A. Richards and X. Jia 2006).

Remote sensing systems collect data by detecting the energy that is reflected from an object or area under investigation. Considering the electromagnetic radiation as the principal physical carrier of information, a main differentiation of remote sensing systems is based on the typology of the source of energy exploited. Depending on whether these systems measure the radiation that is naturally available, or the energy used to illuminate the target under investigation is emitted by the sensor, are defined as passive or active, respectively. Passive sensors rely on the energy provided by the Sun, which is either reflected, or absorbed and then re-emitted from the Earth's surface. While the reflected energy (e.g., visible radiation) is available only when the Sun illuminates the Earth, the emitted energy (e.g., thermal infrared radiation) can be detected at any time, as long as the amount of energy is large enough to be recorded. Examples of the most popular passive sensors are cameras, scanning sensors and microwave radiometers. Active sensors instead, emit the energy required to illuminate the target under investigation, and then detect the backscattered radiation. Examples of broadly used active systems are the RAdio Detection and Ranging (RADAR) and Light Detection and Ranging (LiDAR). In this case, being the sensor as the source of radiation, the data acquisition can be performed at any time (J. R. Schott. 2007).

The vast variety of available sensors, which provide data either in image or signal formats, allows to tackle a large number of applications with remarkable advantages. In general, each family of sensors is characterised by properties such as spatial, spectral, radiometrical and temporal resolutions, which are strictly related to their physical implementation resulting more or less suitable for a precise application. This entails the development of advanced techniques for data processing and interpretation that are sensor and application dependent. Space

exploration is the RS domain that leads by far the technological advances, providing important know-how also for the Earth monitoring and for its understanding as a celestial object (Lentile and Nate C. Benson, 2006.). Another main application is related to the environmental monitoring, where remote sensing techniques are used for studying human activities, such as urban planning, agriculture land usage, and natural phenomena, such as damage assessment due to earthquakes or floods, eruptions, climate change (e.g., glaciers), deforestation. Protected areas with fragile ecosystems can be studied by means of non-invasive remote sensing-based monitoring, without carrying any risk of environmental damage, replacing in this way costly field campaigns. Other important applications include meteorology, national security and natural resource management. The dissemination of remote sensing data is another important topic and is strictly connected to geographic information systems (GIS). Such platform allows remote sensing data obtained by different sources to be combined in order to make the information readily understandable to the final users (L. Bruzzone and B. Demir, 2014.).

1.4. Introduction to Hyperspectral Images

Earth remote sensing includes data collection on the environment, geology, climate, and other characteristics of the Earth by means of sensors positioned in the air or in Earth orbit. An important distinction between the systems broadly used to this end, refers to the coverage of electromagnetic spectrum. Focusing on passive optical systems, the sensor acquires data as in image format, detecting a portion of the electromagnetic radiation reflected from the Earth's surface in a range of wavelengths that includes the visible, near-infrared and short-wavelength infrared regions of the electromagnetic spectrum. The sensor system, for instance the scanner, is composed by detectors that scan the scene and store the radiance detected as a quantised sample of the continuous data stream, forming a pixel

characterised by a digital number, DN. To create multi-channel images that show specific portions of the EM field, the detected beam is split into different spectral components by inserting a system of spectral filters and optical components (e.g., prism, grating). For a more detailed review on sensor systems and different typology of scanners, please refer to (R. A. Schowengerdt 2007; J. R. Schott 2007; J. A. Richards and X. Jia 2006).

According to the characteristics of the scanner, sensor systems are distinguished by their different resolutions, which also define the characteristics of the acquired images. Measure of the sensor's ability to image closely spaced objects so that they are distinguishable as separate objects represents the spatial resolution, and depends on the altitude of the sensor and its angle of view (i.e., the angle subtended by the sensor), which is defined in terms of Instantaneous Field of View (IFOV). In digital imaging, the resolution is limited by the pixel size. The spectral resolution is related to the bandwidth of the specific spectral channel at which the instrument is sensitive, while the radiometric resolution is defined as the minimum energy able to be detected by the sensing system. The intrinsic radiometric resolution of a sensor depends on the detector's signal to noise ratio. In a digital image, the radiometric resolution is limited by the number of discrete quantisation levels used to digitise the continuous intensity value. Considering a three-dimensional space (x, y, λ), where x and y are spatial coordinates and λ the spectral coordinate, each pixel is the integral of the radiance in a small volume (cube). The minimum value obtained by the integral represents the radiometric resolution, whereas the spatial resolution is represented by the size of a cube in the plane (x, y). The spectral resolution is the minimum bandwidth on which the measured radiation is integrated. Although the acquisition system could detect signals with high resolutions, it counts on various critical points due to physical constraints and instrumental limitations. Indeed, the acquisition of the images is usually affected by the sensor's noise, bad pixel location and atmospheric contribution, requiring different levels of pre-processing in order

to ensure the image quality in terms of spectral, spatial and radiometric accuracy (J. A. Richards and X. Jia 2006) and make the data available for further analysis. According to criteria that include spectral range, spectral and spatial resolutions and number of bands, the acquired images are identified as panchromatic, multispectral and hyperspectral. Panchromatic images are mono-channel data, which spatial resolution is maximised with a consequently minimisation of the spectral resolution. In such images, the high geometrical detail permits objects on the ground to be represented in detail, however, the information of the target's spectral characteristic results poor, meaning that objects of different nature can be represented in the same range of pixel values, making their discrimination difficult to achieve. In multispectral images, the augmented spectral dimension, which is represented by a few wide spectral channels that cover wide portions of the electromagnetic spectrum, provides useful information on the nature of the targets and facilitates their discrimination and classification. In hyperspectral images, the spectral resolution is further improved, where the spectral information is maximised, providing data characterised by hundreds of narrow and contiguous spectral-channels. Consequently, each pixel can be represented as a vector in which a given value corresponds to the radiation at a given spectral band. The high dimensionality of this vector intrinsically provides a finer representation of the spectral signature of the target, leading to a better discrimination among different materials with respect to multispectral images, which are characterised by only few spectral channels. Moreover, recent technological advances in sensor technology have led to the development of a new generation of hyperspectral sensors able to provide images with improved spatial resolution. For instance, an image acquired by Hyperion sensors (mounted on EO-1 satellite) has a spatial resolution of 30 m, while ROSIS-3 (airborne spectrometer) can provide images with a spatial resolution of 1.7 m if the acquisition is taken at the altitude of 3 km. CASI-1500 can provide a data cube of 144 spectral bands with a spectral resolution of 1.25 m. From these few

examples, we can see that the contextual information, becomes an important source of information that can be exploited for distinguishing different objects on the ground. Hyperspectral images have been widely exploited in different applications, ranging from forestry management, pollution detection and mineral exploration. Table 1 provides a summary of the most commonly used sensors usually mounted on aircraft or spacecraft, reporting the principal spectral characteristics.

Table 1: Technical characteristics of some hyperspectral sensors developed over last years (Atiya et al. 2022)

Sensor	Manufacturer	Platform	Number of bands	Spectral Resolution	Spatial Resolution
PRISMA	Selex	Satellite	239	12nm	0.4 – 2.5 µm
EnMAP	OHB	Satellite	232	10nm	0.4 – 2.5 µm
Hyperion	NASA GSFC	Satellite	220	10nm	0.4-2.5 µm
CHRIS Proba	ESA	Satellite	up to 63	1.25nm	0.415-1.05 µm
AVIRIS	NASA JPL	Aerial	224	10nm	0.4-2.5 µm
HYDICE	Naval Research Lab	Aerial	210	7.6nm	0.4-2.5 µm
PROBE-1	Earth Search Science	Aerial	128	12nm	0.4-2.45 µm
CASI 550	ITRES Research Ltd	Aerial	288	1.9nm	0.4-1 µm
CASI 1500	ITRES Research Ltd	Aerial	288	2.5nm	0.4-1.05 µm
SASI 600	ITRES Research Ltd	Aerial	100	15nm	0.95-2.45 µm
TASI 600	ITRES Research Ltd	Aerial	64	250nm	8-11.5 µm
HyMap	Integrated Spectronics	Aerial	125	17nm	0.4-2.5 µm
ROSIS-3	DLR	Aerial	115	4nm	0.43-0.85 µm
EPS-H	GER Corporation	Aerial	133	0.67nm	0.43-12.5 µm
EPS-A	GER Corporation	Aerial	31	23nm	0.43-12.5 µm

DAIS 7915	GER Corporation	Aerial	79	15nm	0.43-12.3 μm
AISA Eagle	Spectral Imaging	Aerial	244	2.3nm	0.4-0.97 μm
AISA Eaglet	Spectral Imaging	Aerial	200	-	0.4-1.0 μm
AISA Hawk	Spectral Imaging	Aerial	320	8.5nm	0.97-2.45 μm
AISA Dual	Spectral Imaging	Aerial	500	2.9nm	0.4-2.45 μm
MIVIS	Daedalus	Aerial	102	20nm	0.43-12.7 μm
AVNIR	OKSI	Aerial	60	10nm	0.43-1.03 μm

1.5. Hyperspectral Image Classification: Challenges

The Earth Observation domain entails numerous open research issues to overcome, ranging from the hardware technology itself to the higher-level data analysis algorithms for the remote sensing image understanding. Focusing on the later, remote sensing image classification emerges as one of the major challenges. Image classification refers to the process of identifying the diverse objects, materials or items of interest with common properties that are group into the so-called "classes" of coverage present on the ground of the investigated area of interest. Product of this process is a thematic map, where pixels are characterised by a given label, usually represented by a colour or symbol, used to uniquely identify the items within a class. A general scheme of image classification is illustrated in Fig 2, in which available information can be exploited in both the data processing and the classification stage. If on the one hand the burst of informative content conveyed in hyperspectral images, represented by both high spectral and spatial resolutions, provides the base for obtaining high accuracy in the identification of different land-covers, on the other hand it introduces a number of challenges that need to be

efficiently addressed. First, the high dimensionality of the data causes a variety of issues in hyperspectral classification referred to in literature as the "curse of dimensionality". The high dimensionality, which is represented by the spectral dimension, makes the analysis computationally expensive, limiting the exploitation of traditional classification approaches, usually employed in multispectral image analysis. In the context of supervised classification, in which labelled samples are used in the classification process, the ratio between the number of available training samples (which is usually small) and the spectral dimension (which is high), affects the generalization capability of the classifier. In general, it has been observed that, beyond a certain point, the inclusion of additional features, while keeping the number of training samples constant, leads to a decrease of both the accuracy and the generalization of the classification process in the machine learning domain, this behaviour is known as the Hughes phenomenon (named after Gordon F. Hughes) (G. F. Hughes 1968). Second, the increase of the spatial resolution in the new generation of spectrometers introduces other important issues in the analysis and classification of hyperspectral images. The high geometrical detail of the scene leads to the presence of objects that are composed by several spatial correlated pixels, resulting in an increase of the intraclass variability (L. Bruzzone and B. Demir. 2014). The aforementioned phenomenon decreases the effectiveness of the analysis when only the spectral information is considered, enforcing the need of strategies that integrate the analysis of both spectral and contextual domains in order to maximize the exploitation of the information combined in these images.
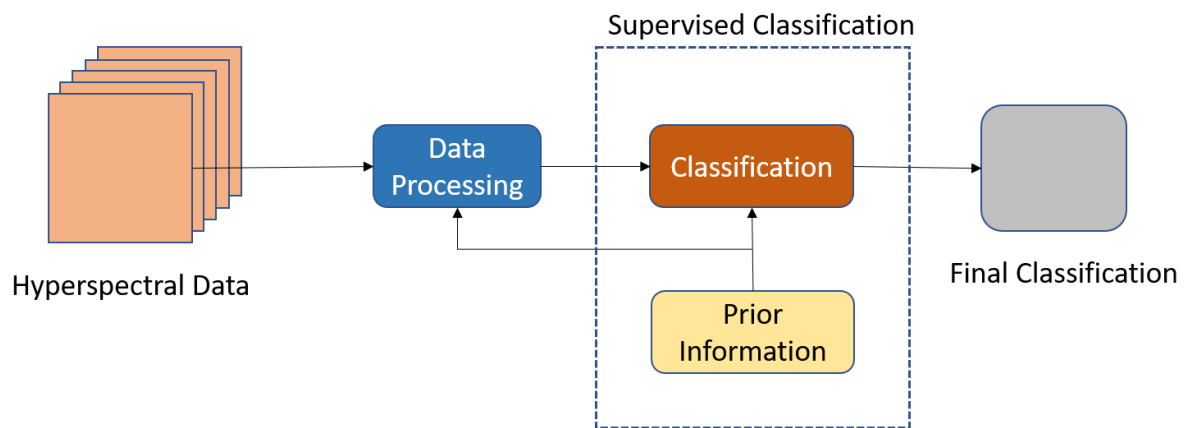
Fig 2. General scheme of a supervised image classification approach. Available prior information can be used in both the classification stage and the data processing stage.

1.6. State-of-the-Art

1.6.1. Related Work on Wildfire Vulnerability Map

In this context, evaluating the impacts of wildfire occurrence and developing approaches to prevent potential damages are critical for fire management. Vulnerability assessment provides particular tools to analyse the potential for loss and has received growing attention at the international level (Susan L. Cutter 2015; United Nations 2015). Previous efforts have been made to define logical and consistent vulnerability assessment approaches;

Some studies focused specifically on the ecological dimension of wildfires as follows:

(Aretano et al. 2015) has conducted has mapped ecological vulnerability to fire for effective conservation management of natural protected areas. Their research integrated the use of GIS–based Decision Support System (DSS) with a conceptual linear model of vulnerability to foster conservation strategies in protected areas, by identifying: (1) the most vulnerable areas, requiring specific protection measures to enhance the natural features, as well as the prevention of natural and human risks;

(2) the most effective management interventions to reduce system vulnerability to fire.

(Duguy et al. 2012) modelled the ecological vulnerability to forest fires in Mediterranean ecosystems using Geographic Information Technologies. An innovative GIS-based modelling approach to evaluate the ecological vulnerability to fire of an ecosystem, considering its main components (soil and vegetation) and different time scales was developed. The evaluation was structured in three stages: short-term (focussed on soil degradation risk), medium-term (focussed on changes in vegetation), and coupling of the short- and medium-term vulnerabilities. The model was implemented in two pilot sites: Arago´n (inland North-eastern Spain) and Valencia (eastern Spain).

Whereas some studies were centred at socio-economic aspects as follows:

(Rodríguez Silva, Ramón Molina Martínez, and Castillo Soto 2012) has developed a methodological approach for assessing the economic impact of forest fires using MODIS remote sensing images. They have summarised as, the ability to incorporate satellite image processing into economic damage assessment allows identifying with greater precision the delimitation of the affected areas based on the 'normalized vegetation index'. Analysis and interpretation of MODIS images, combined with the energy intensity emitted by the spread of fire, can be integrated into econometric models in order to obtain, in a geo-referenced manner, the economic value per hectare resulting from wildfire damage.

(Román, Azqueta, and Rodrígues 2013) has conducted methodological approach to assess the socio-economic vulnerability to wildfires in Spain. Their study aimed to develop a methodology for the assessment of the socio-economic vulnerability to fire using Geographic Information Systems. We have conducted the vulnerability assessment by estimating the potential losses fire might cause during the time required for the recovery of the pre-fire environmental conditions.

1.6.2. Related Work on Wildfire Fuel Map

Spatially and thematically accurate vegetation cover is critical for the suppression and prevention of fire in fire-prone areas and ecosystems. In order to generate wildfire fuel maps, researchers around the world are trying to develop techniques for fuel mapping using hyperspectral data as follows:

(Goodenough et al. 2003) have compared forest classification accuracies between EO-1's Hyperion and ALI sensors and Landsat 7 ETM+ and concluded that hyperspectral sensors provide better discrimination with greater accuracy in comparison with multi-spectral sensors in several forest types.

The potential of wildfire fuel mapping using hyperspectral data of Hyperion was evaluated by (Yeosang Yoon and Yongseung Kim 2007) almost a decade ago and concluded that the Hyperion imagery has good potential for wildfire fuel mapping.

(Smith et al. 2021) has mapped Boreal Forest fuel types for interior Alaskausing AVIRIS-NG hyperspectral data with 80 percent accuracy when LANDFIRE's Existing Vegetation Type product derived from Landsat-8 has 33 percent accuracy.

For the same region of interest, (Badola et al. 2021) has simulated hyperspectral data using Sentinel-2 was used to map boreal forest fuel type with 89 percent accuracy, which was better than the accuracy obtained using multi-spectral Sentinel-2.

A detailed review was conducted by (Veraverbeke et al. 2018c) on hyperspectral remote sensing of fire. The authors commented that hyperspectral data had proven utility in the temporal stage of the fire disturbance continuum, including pre-fire applications, i.e., in exact fuel type and condition assessment. Also, added that till 2018 there was only airborne hyperspectral data, and the upcoming spaceborne missions like PRISMA, EnMAP, and HyspIRI will provide opportunities to explore further the linkages between ecosystem properties and fires at regional to global scale.

1.7. Objectives of this Dissertation

This dissertation was carried under the framework of two projects:

1. S2IGI: An Integrated System for Forest Fire Management funded by Regional Administration of Sardinia under the POR (Programma Operativo Regionale) FESR (Fondo Europeo di Sviluppo Regionale) Sardegna 2014 – 2020. Supporting wildland fire prevention and management is the key objective of the S2IGI (Sistema Satellitare Integrato Gestione Incendi) project, which aims to provide a short- and medium-term forecasting of wildfire danger, an early detection of wildland fires, a real-time forecast of wildland fire propagation, and an assessment of fire damages, based on the use of advanced technologies as Earth Observation (EO) data exploitation.

2. ASI_HYP (Progetto per sviluppo di prodotti iperspecttrali prototipali evoluti) project funded by Italian Space Agency and coordinated by e-geos SpA for developing various prototypes viz., fuel map, vegetation indicators, water quality, forest fire front, volcanic parameters etc., using PRISMA (a satellite of Italian Space Agency) hyperspectral imagery. A real-time forecast of various environmental factors using PRISMA is the major goal.

The objectives of this dissertation are as follows:

(1) To develop a wildfire vulnerability map for the Sardinian Island of Italy using the vulnerability index developed in the previous project PREFER.

(2) To develop a procedure to classify wildfire fuel types using hyperspectral imagery from PRISMA launched by the Italian Space Agency (ASI) in 2019.

(3) To develop forest fires fuel map based on Anderson fuel models that can support in extracting parameters such as fuel load [t/ha] for the living and dead component of the vegetation, the height of the fuel (litter) to the ground, extinction humidity [%], flame height [m] and propagation rate [m/sec].

(4) To develop wildfire dynamic fuel map based on Scott/Burgan models that can support in extracting parameters such as fuel parameters such as fuel bed depth (ft), fine fuel load (t/ha), characteristic SAV (1/m), packing ratio (dimensionless), heat content (KJ/kg) and extinction moisture content (percent).

(5) To automate the process of fuel mapping using Graphic User Interface so that any part of Europe can be mapped for wildfire fuel types using LUCAS points as input.

(6) To conduct SWOT (Strength, Weakness, Opportunities and Threat) analysis to evaluate the feasibility and maturity of PRISMA hyperspectral imagery for mapping wildfire fuel types.

1.8.   Structure of the Thesis

Chapter 2 is about wildfire vulnerability map. The procedure used for mapping vulnerable areas on the Island of Sardinia. Chapter 3 focusses on classification of fuel types using PRISMA hyperspectral imagery. The procedure developed for classifying the fuel types implementing machine learning techniques were explained in this chapter. Chapter 4 presents the procedure of correlating the classified fuel types to Anderson fuel models. Similarly, chapter 5 presents the procedure of Scott/Burgan based fuel mapping. Chapter 6 explains the system architecture i.e., the procedure used to automate the process of fuel mapping. Then, next chapter concludes the thesis by summarizing the important points in this thesis.

WILDFIRE VULNERABILITY MAP

2.1. Introduction to Vulnerability Map

The analysis of vulnerability is a main requirement for the assessment of fire risk. In a general sense, vulnerability means the potential for loss (M. A. Cutter 2006) and, despite differences in the precise definition of this concept, it is rather well established that it relates to the degree of loss that can affect different types of assets, either biophysical or anthropogenic (M. A. Cutter 2006; Birkmann et al. 2013a).

The United Nations (United Nations 2015) defines vulnerability as "the conditions determined by physical, social, economic and environmental factors or processes which increase the susceptibility of a community to the impact of hazards". As such, the assessment of vulnerability to forest fires requires the analysis of a rather large set of variables that represent the different types of assets or elements potentially affected by fires.

The vulnerability approach applied in PREFER is comprehensive, combining variables that reflect multiple dimensions: social, environmental, economic and institutional. The vulnerability level results from the combination of three different components: exposure, sensitivity and coping capacity.

Exposure refers specifically to the presence of people, property, systems, or other elements in hazard zones that are, for that reason, subject to potential losses (United Nations 2015). Sensitivity represents the conditions that influence the predisposition of the exposed elements to suffer a certain level and extension of damages (Rodrigues et al. 2013; Birkmann et al. 2013b; S. L. Cutter 2011). Coping capacity is related to the circumstances that reduce or amplify the ability of the elements to respond and recover from the impacts of a hazard (Birkmann et al. 2013b).

2.2. Fire Vulnerability Indices

From the conceptual approach defined for vulnerability assessment, a proposal for the analysis of data, for the integration of the variables and for the creation of the composite indices that represent each component as shown in Fig 3, as well as the production of the final vulnerability and economic value maps, was outlined and it is explained in detail in this section. Examples of the results obtained for the AOI of Sardinia are also presented.
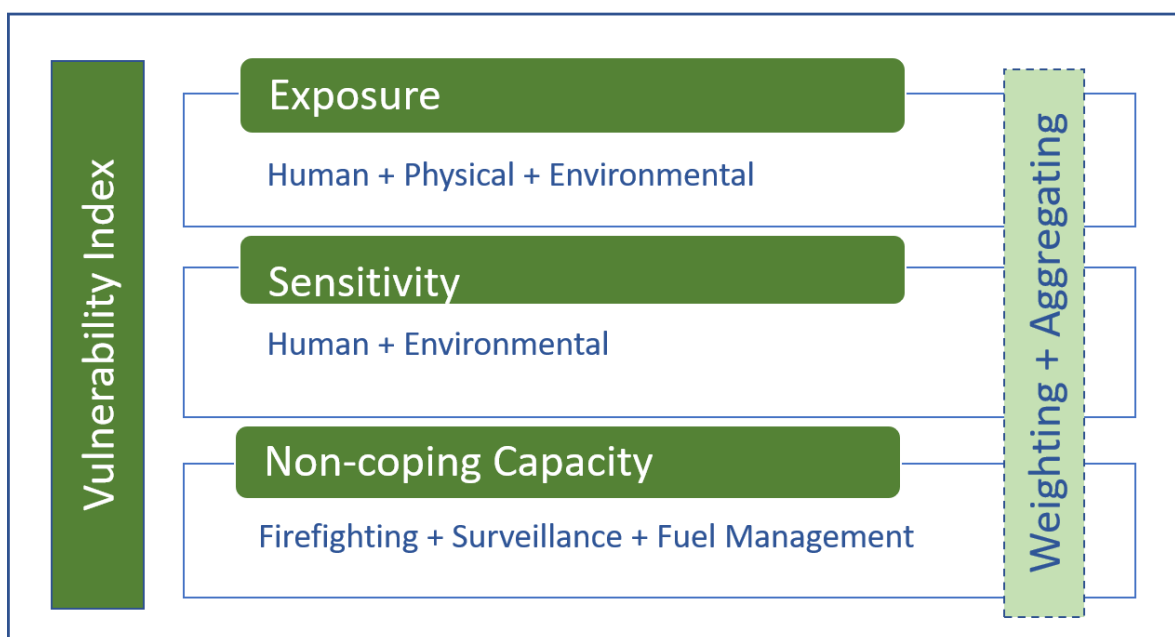
Fig 3. Description of Vulnerability Index

As vulnerability results from the combination of different datasets and variables, which are obtained from diverse sources and at different scales and/or formats, a set of rules and conditions were defined for the processing chain of the data, to ensure the consistency of the products, as explained below:

a) Vulnerability assessment is comprehensive but it should be rather simple to interpret, in order to be applied by different users;

b) The processing chain is defined considering the possibility to integrate new or better data when these become available. It was verified that, for specific

areas within Mediterranean Europe, and depending on the quality of the national data sources, if additional data are available; as such, better maps can be produced for these areas. Furthermore, the processing chain allows for maps to be updated seasonally, as defined in the products requirements, and these maps can then include other data that was not available beforehand;

c) Each component of vulnerability is, first, analysed individually, creating composite indexes. The three indexes (components) are then combined in a vulnerability map;

d) For each component, the variables represent different dimensions of vulnerability (social, environmental or institutional); each variable can also be represented cartographically;

e) The spatial resolution of the maps is 1 ha (100 x 100 m), resulting as the best compromise between the spatial resolution of data obtained from different sources (e.g.: remote sensing data at very high resolution and statistical data at municipality level); a grid at 100 m was created based on the European grid available from the EEA at 1 km (http://www.eea.europa.eu/data-and-maps/data/eea-reference-grids-2);

f) Similar methodologies are applied to analyse and integrate the variables and components:

i. Variables: each variable is transformed in a numerical scale, representing proportions, densities, distances or ratios; there is a value per each 1 ha cell; all variables are normalized to a common scale;

ii. Components: are analysed in an ascending order, i.e., higher values represent higher levels of exposure or sensitivity. The component of coping capacity is, instead, presented in an inverted scale, to be consistent with the other components and to represent the higher values as the areas where more urgent attention is

needed. Table 2 shows the components, definitions of considered components and their variables.

Table 2: Definition of the three components of vulnerability and the corresponding variables collected

Components	Definition	Variables
Exposure	Presence of elements in hazardous areas that can suffer losses in case a fire occurs. It is related to the location of urban areas and forests, to the density of buildings and the location of infrastructures, among others.	✓ Population density ✓ Building's density ✓ Road's density ✓ Land cover type ✓ Presence of protected areas
Sensitivity	Conditions that influence the predisposition of the exposed elements to suffer different types and levels of damages. It is associated with their intrinsic characteristics (species type, buildings' materials, population characteristics) and/or with their degree of protection, for example.	✓ Elderly (> 64 years) ✓ Education level ✓ % People working in primary sector **Protected Areas (JRC)** ✓ Number of classifications (national, international) ✓ International Union for Conservation of Nature categories (IUCN)
Coping Capacity	Implementation of actions to reduce the probability and susceptibility of the exposed elements to suffer losses. They can be anticipation measures (surveillance activities, prevention campaigns) or response measures (fire-fighting planning, emergency services available), among others.	✓ Density of forest access roads ✓ Nr. Firefighters/forest area ✓ Surveillance towers (visibility area)

For each component, a set of variables was selected, each of them representing one type of element potentially affected by fires and one of the dimensions of vulnerability, or, in the case of coping capacity, the elements or activities that potentially influence the ability to prevent or to fight a fire. Figure 1 below presents the variables collected hitherto for each component.

2.3. Study Area

The study area is Sardinia, Italy, the second largest island of the Mediterranean Basin. The island has a topography characterized by the most relevant hills and mountains on the eastern side and plains located in the western part, with two main flat areas: Campidano in the South, and Nurra in the North. The highest peak is situated in central Sardinia and reaches about 1850 m a.s.l. The climate, albeit with some gradients from the coastal areas to the mountains, and from South to North, is characterized by a mild and rainy period, from October to May, and a warmer one, from June to September, with peaks above 30 °C in several days, and with a low incidence of rainfall. The annual cumulative precipitation ranges from 500 mm in the coastal areas to about 1200 mm in the mountain peaks. Approximately half of Sardinia is covered by broadleaf forests (about 16 %), in particular Quercus spp., and Mediterranean shrubs and garrigue (about 30 %) (Fig. 4) (Sardinia land use map of 2003, www.sardegnageoportale.it). Unlike other Mediterranean areas, the presence of Pinus spp. is limited (nearly 3 %). A significant part of the island is represented by grasslands and mixed agricultural areas (approximately 40 %), while the remainder is composed by herbaceous pastures, vineyards and orchards, and urban areas.

Fig 4. Region of Interest for Wildfire Vulnerability Analysis

This Island has the characteristics of frequent fire occurrences. In the last decade, 1008 fires per year have been recorded only in Sardinia, which is 20% of the total fires at the national level. Sardinia has a typical Mediterranean climate, with mild and rainy winters and warm and dry summers with evaporation exceeding precipitation from April to September. Mean annual precipitation rises with increasing altitude and is lowest at the coast.

2.4. Materials and Methods

2.4.1. Exposure

The analysis of exposure required the integration of variables that represent the different types of elements that may suffer losses in case a fire occurs. Table 3 shows the data, parameters and variables considered for the exposure component.

Table 3: Parameters and variables for the analysis of exposure

ID	Parameters	Dimension	Variables	Sources
1	Population	Social	Population density	JRC Earth Observation Data and Processing Platform (www.cidportal.jrc.ec.europa.eu)
2	Land cover / use	Environmental	Categories of land cover (weighting)	Remote sensing Corine Land Cover 2018 (www.eea.europa.eu)
3	Buildings	Social	Building's density	www.download.geofabrik.de
4	Infrastructures	Social	Road's density	www.download.geofabrik.de
5	Protected natural areas	Environmental	% Area occupied by protected areas	Protected Planet (http://www.protectedplanet.net) National sources (www.sardegnageoportale.it/)

Processing of exposure component was carried out for each variable as described in Table 4.

Table 4: Brief description of the process of analysis of the variables included in exposure assessment

ID	Variables	Processing
1	Population density	Population density map available at 1 ha resolution; the vulnerability grid at 1 ha was overlapped and each cell received the corresponding value of population density
2	Categories of land cover	6 categories of land cover were created by aggregating CLC classes; a specific weighting was given to each category depending on their relationship with fire and based on literature review
3	Building's density	Number of buildings calculated per ha for the minimum spatial unit available (municipality, LAU5 or below); the vulnerability grid at 1 ha was overlapped and each cell received the corresponding value; in case the cell overlapped more than one spatial unit, the weighted mean of the spatial unit's values was calculated and attributed to the respective cell
4	Road's density	Length of roads per ha for each cell of the vulnerability grid
5	Area occupied by protected areas	The polygons of all the classified protected areas (Natura 2000 ZSP and SCA, UNESCO Biosphere Reserve, national classifications and Ramsar wetlands) were merged and overlapped with the vulnerability grid. The proportion of area occupied by protected areas, regardless of their classification, was retrieved for each grid cell

CORINE land cover map of 2018 was considered and weightage to each land cover type was given as shown in Table 5. Non-fuels were given a weightage of zero whereas other fuel types were given a weightage according to the proneness to fire.

Table 5: Weighting of land cover categories, relation with fire and references

Category	Weighting	Characteristics
Water and other non-fuels (bare rocks, glaciers…)	0	Non-burnable due to lack of vegetation
Artificial surfaces	0	Non-burnable due to lack of vegetation

Agricultural areas (excluding pastures)	0.3	Burnable, with less susceptibility than shrubs and forests. Easily recovered
Discontinuous urban surfaces (proxy of WUI) + Burnt areas	0.6	WUI relation with fire; re-incidence of fires in burnt areas due to type of vegetation growth after fire
Shrubs and grasslands (including pastures)	0.8	Susceptible to fire. Moderate fuel loads
Forests	1	Susceptible to fire. Heavy fuel loads

All the variables described above were normalized to the [0-1] numerical scale, with the formula of minimum (min) and maximum (max) values:

$$Norm\ [0-1] = \frac{var\ (value) - \min\ (var)}{\max(var) - \min(var)}$$

with

- Norm, being the resulting normalized value in the scale 0 to 1,
- the var (value), the value of the variable processed,
- the min (var), the minimum value of that variable in the study area;

the max (var), the maximum value of that variable in the study area
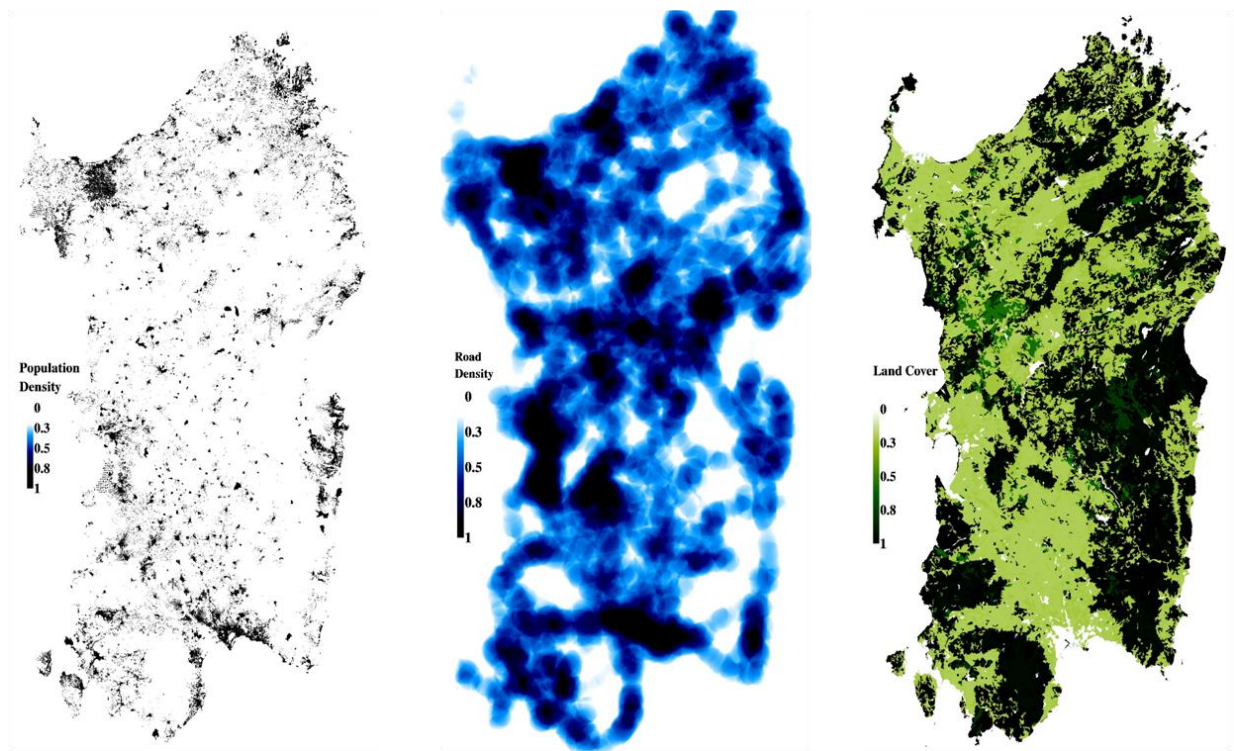
Fig 5. Map of population density, road density and land cover, with normalized values divided in 5 classes, for the AOI of Sardinian Island

The map of exposure was obtained with an additive model and maps of population density, road density and land cover were shown in Fig 5. Each variable received an equal weight (1/5 or 0.2), considering the relative importance of each dimension for forest fires. This weight was multiplied by the normalized value of the variable and, finally, these 5 values were summed up.

$Exposure\ Index = (Population\ Density * 0.2) + (land\ cover * 0.2) + (buildings * 0.2) + (roads * 0.2) + (protected\ areas * 0.2)$

The value of exposure, thus, represents the density or proportion of each element exposed and the number of exposed elements present in each grid cell (ha). Higher density of an element or proportion of area occupied by a variable is represented by higher exposure as shown in Fig 4; more variables present are expressed as higher exposure.
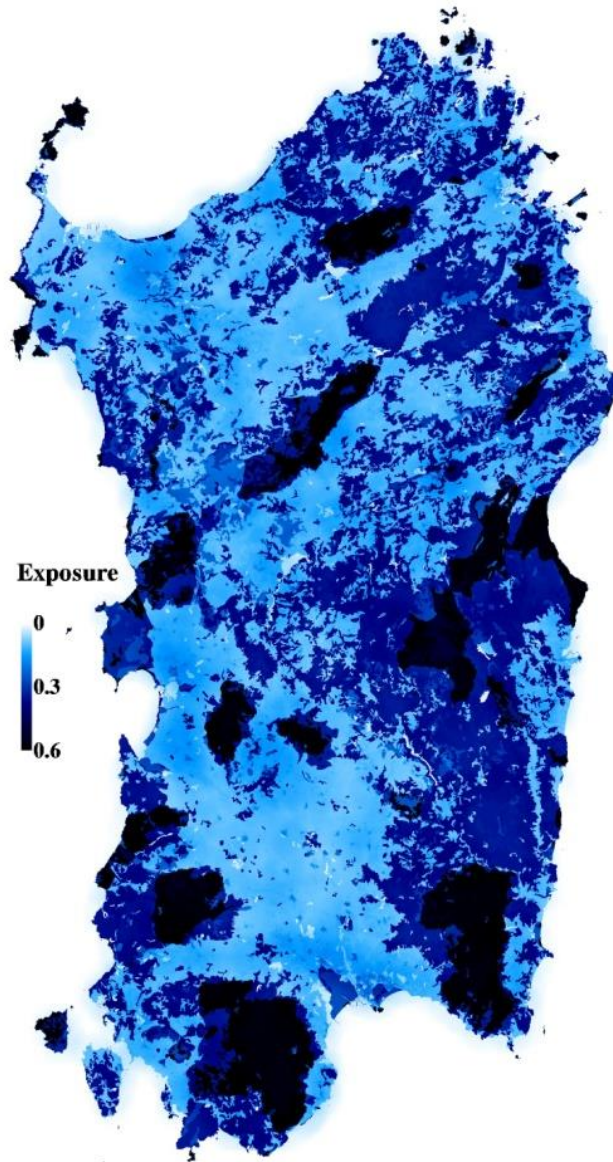
Fig 6. Map of exposure for the AOI of Sardinia

2.4.2. Sensitivity

The analysis of sensitivity includes the variables whose differentiated conditions can be assessed. Hitherto, only the conditions of population and the level of protection of protected areas were available (Table 6). As the exposure of land cover already included a weighting according to its relationship with fire, no further sensitivity analysis was done for this parameter, to prevent co-linearity. Building's

materials, whose sensitivity to fire may differ, are currently being explored by remote sensing data interpretation and were not yet included in this assessment.

For the analysis of sensitivity, parameters and variables considered are tabulated in Table 6. Other columns of table provide the dimension, justification and sources of the data considered.

Table 6: Parameters and variables for the analysis of sensitivity

No	Parameters	Dimension	Variables	Justification	Sources
1	Protected Natural Areas	Environmental	Number of classifications of protection (1 to 5)	Number of classifications in each 1 ha cell, from Natura 2000 SPA and SCA, UNESCO Biosphere Reserve, Ramsar wetlands and national classification	http://www.protectedplanet.net National sources (www.sardegnageoportale.it/)
			Level of sensitivity by IUCN category (1 to 6)	Each IUCN category is weighted according to the level of protection and management objectives it corresponds to	http://www.iucn.org
2	Fuel	Environmental	Level of fire proneness	Each category is weighted according to the level of fire proneness	Oliveira et al., 2014
3	Population	Social	% Elderly (> 64 years)	Elderly people are more susceptible to injuries and	www.istat.it

	require special care.

Processing of each parameter is as follows:

Protected Natural Areas

a) **Number of classifications (national and international importance–higher natural value)**

✓ National Protected Area (PA)

✓ Special Protection Areas (SPA, Natura 2000)

✓ Special Areas of Conservation (SAC, Natura 2000)

✓ Ramsar – Wetlands

✓ UNESCO – Biosphere Reserves

Each classification weights 0.2. Sum of classifications (maximum 5*0.2 = 1)

b) **Level of classification by IUCN**

6 categories, according to the management objectives and level of protection:

I (a e b)   – Natural Reserves and Wilderness Areas

II   – National Parks

III   – Monument or Natural Resource

IV   – Area of Management of Habitats or Species

V   – Protected Landscape

VI   – Protected Landscape with sustainable use of Natural Resources

Weightage given to each protected area: I – 6/6; II – 5/6; III – 4/6; IV – 3/6; V – 2/6; VI – 1/6. Areas not classified by IUCN get the value of 0.1

The final sensitivity map of protected areas results from the aggregation of (a) * (b).

Example: i) 2 classifications (0.2*2 = 0.4) * 5/6 (IUCN level II) = 0.33

ii) 5 classifications (0.2*5 = 1) * 6/6 (IUCN level I) = 1

Population

The sensitivity of population is calculated by using the most significant component, which is a combination of % *Elderly* and *% People with up to the elementary education level, each variable with correlation above 0.5.*

Fuel Map

The fuel map was generated according to the where weights to different categories of land cover type were given with standardised selection ratio (SR).

$$SR = \frac{Proportion\ of\ land\ cover\ type\ used\ in\ the\ burnt\ area}{Proportion\ of\ land\ cover\ type\ available\ in\ the\ buffer}$$

The map of sensitivity was obtained with an additive model, similar to the method applied for exposure. Each variable received different weight according to its importance, which can change as other variables are added to the sensitivity analysis. This weight was multiplied by the normalized value of the variable and, finally, the all values are summed up.

$$Sensitivity\ Index = (Population\ Sensitivity * 0.4) + (fuel * 0.4) + (protected\ areas\ sensitivity * 0.2)$$

Fig 7 shows the sensitivity map with values ranging from [0-0.9]. The value of sensitivity represents the predisposition of the elements present in an area to suffer a higher level of losses in case a fire occurs.
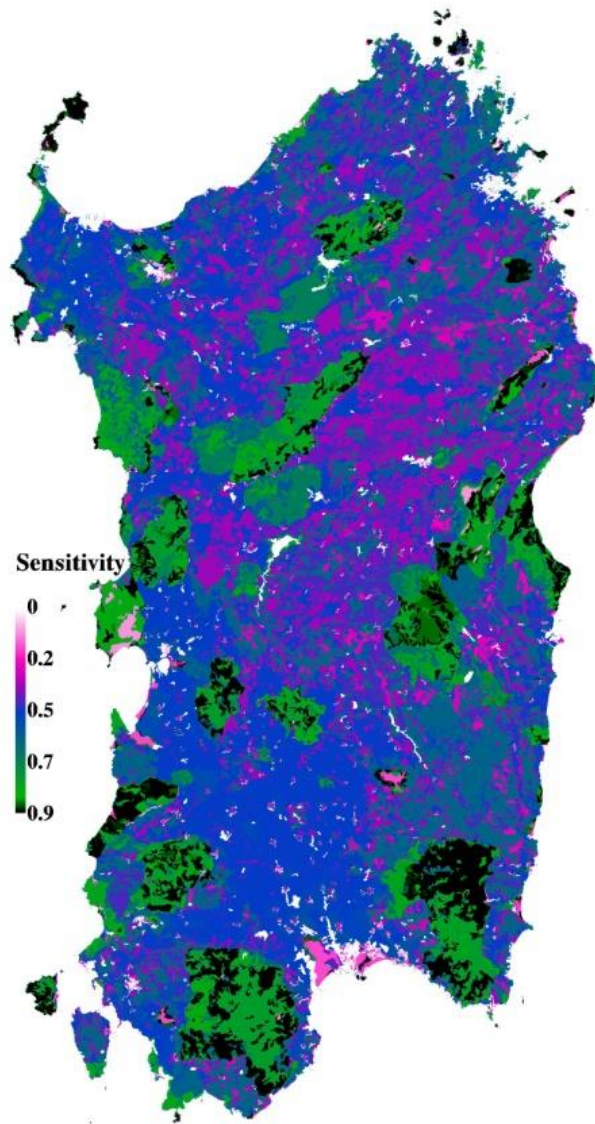
Fig 7. Map of sensitivity for the AOI of Sardinia

2.4.3. Coping Capacity

The variables included in the analysis of coping capacity are mainly obtained from national sources (civil protection and forest services). Furthermore, it is likely that not all the variables exist in the different countries nor that they will be directly available to researchers, thus the processing of this index may include a different number of variables in each area. Despite this limitation on data availability, the structure of the processing chain is maintained.

Table 7 explains the parameters and variables considered in the coping capacity. Dimensions include surveillance and firefighters and the source of this data was also shown.

Table 7: Parameters and variables for the analysis of coping capacity

No	Dimension	Variables	Source
1	Surveillance	Sedi_postazioni_avvistamento_Forestas _2019 **(SS)**	Regional Administration of Sardinia (RAS)
2	Firefighters	Sedi_organizzazioni_volontari_2019 **(FF1)**	RAS
3		Sedi_presidi_VVF_2019 **(FF2)**	RAS
4		Sedi_squadre_Forestas_2019 **(FF3)**	RAS
5		Sedi_Stazioni_Forestali_2019 **(FF4)**	RAS
6		Compagnie_barracellari_2019 **(FF5)**	RAS

Processing of sensitivity map is as follows. The map of coping capacity is obtained with an additive model. Each variable receives different weight, which is multiplied by the normalized value of each variable. These values are then summed up.

$$Coping\ Capacity = 1 - [\left(FF1 * \frac{1}{6}\right) + \left(FF2 * \frac{1}{6}\right) + \left(FF3 * \frac{1}{6}\right) + \left(FF4 * \frac{1}{6}\right) + \left(FF5 * \frac{1}{6}\right) + \left(FF6 * \frac{1}{6}\right) + \left(SS * \frac{1}{6}\right)]$$
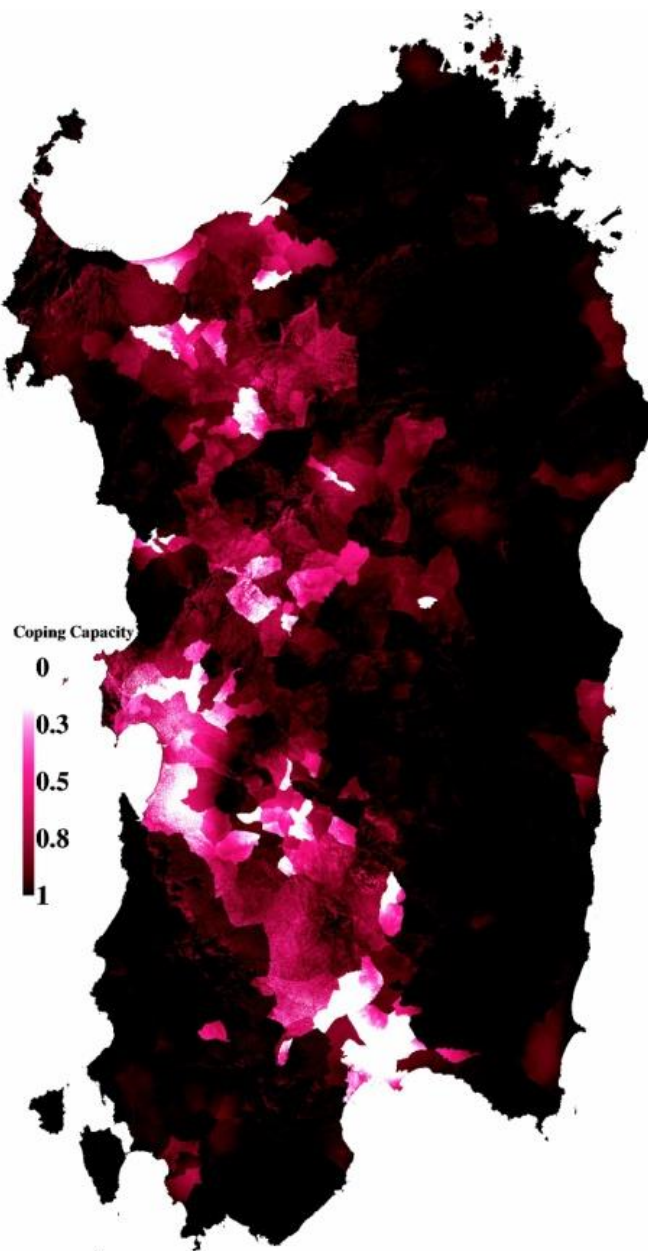
Fig 8. Coping Capacity in the AOI of Sardinia

The method of analysis is similar to exposure and sensitivity, except in what concerns the scale of values, which are presented in an inverted form (1-value), to be consistent with the other indexes: the higher values of coping capacity represent the areas with less resources for prevention, preparedness or fire-fighting, contributing to higher values of vulnerability. Coping capacity map is shown in Fig 8 and the values are ranging from [0-1].

In this work, density of different categories of fire-fighters were found for each municipality and in some cases, according to the scope of their area. For surveillance, towers visibility considering the tower height as 15 metres and Digital Elevation Model (DEM) were found for all the towers.

2.5. Results and Discussions

2.5.1. Vulnerability Map

The vulnerability value results from the combination of the three composite indexes, by applying an additive model. A similar weight is given to each component (1/3) and the value of each component is multiplied by this weight. The three resulting values are then summed up.

$$Vulnerability = \left(Exposure * \frac{1}{3}\right) + \left(Sensitivity * \frac{1}{3}\right) + \left(Coping\ Capacity * \frac{1}{3}\right)$$

Vulnerability is then expressed in 5 different classes, from 1 (low vulnerability) to 5 (very high vulnerability).
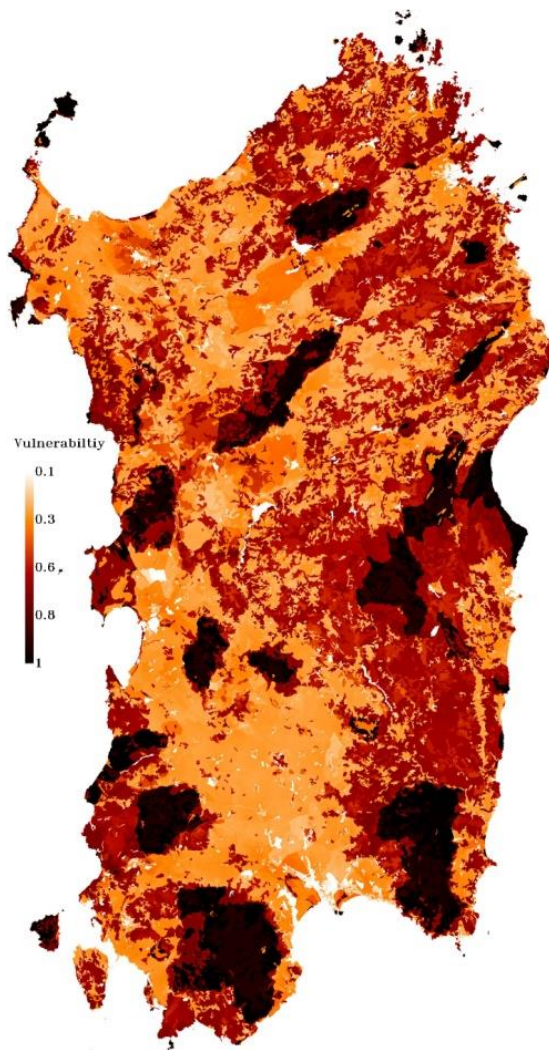
Fig 9. Vulnerability maps for the AOI of Sardinia, expressed in normalized value and by

classes

The Fig 9 shows the resulting map of vulnerability for the AOI of Sardinia, expressed in the normalized value [0-1]. For this area, the minimum value of vulnerability is above zero and the higher class (above 0.75) is not found. The maximum value recorded in this area is 0.73 which is equivalent to 1 after normalization.

FUEL TYPES CLASSIFICATION USING PRISMA HYPERSPECTRAL DATA

This chapter presents the procedure applied to develop the wildfire fuel map using hyperspectral imagery of PRISMA in a semi-supervised machine learning approach. The main objective of the work presented in this chapter is to develop an automatic procedure for wildfire fuel mapping using the maps from Copernicus / National / Regional portals as reference maps.

The steps followed to develop a wildfire fuel map that involves various steps *viz.*, pre-processing, pixels extraction, dataset preparation by pseudo-labelling, machine learning algorithm details, unmixing, further classification of fuel types, and fuel map are illustrated in the flowchart as shown in Fig. 10. Details of the process are described in subsections.
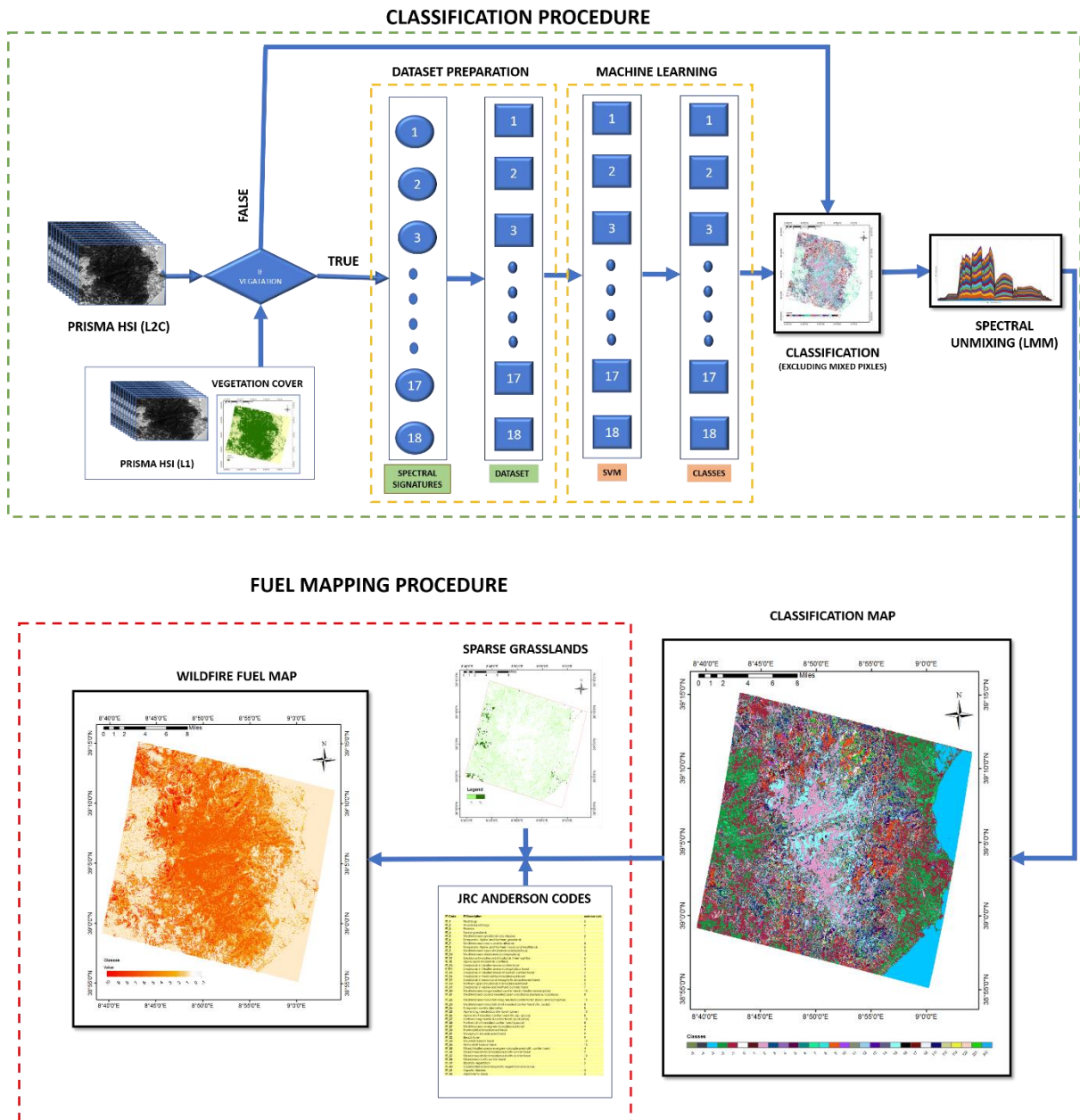
Fig 10: Process Flow Chart

3.1. PRISMA Hyperspectral Data

In this work, hyperspectral imagery from the PRISMA satellite is being used to map vegetation fuel types. PRISMA has taken us into a new era of hyperspectral imaging spectroscopy. This imaging spectrometer can capture a continuum of spectral bands with 400 to 2500 nm at a spatial resolution of 30 m. The sensor counts 173 bands in

the shortwave infrared (SWIR) within 920-2500 nm, and 66 bands are in the visible near-infrared (VNIR) portion of the spectrum (400-1010 nm). The widths and spectral sampling intervals are ≤12 nm. A panchromatic camera providing a single band (400 – 700 nm) image at 5 m spatial resolution is also onboard the ASI's satellite. PRISMA is an on-demand mission, and the available data in the archive (https://prisma.asi.it) are limited but acquires imagery for the required location upon request (Niroumand-jadidi, Bovolo, and Bruzzone 2020).

There are four different levels of PRISMA hyperspectral images with the name of L1, L2B, L2C and L2D.

- Level 1 products: TOA (Top of Atmosphere) radiometrically and geometrically calibrated HYP and PAN radiance images
- Level 2 products: Geolocated (L2B, L2C) and Geocoded (L2D) Atmospherically corrected HYP and PAN images; atmospheric constituents maps (aerosols, water vapour, thin cloud optical thickness) (for L2C and L2D products).

3.2. Study Area

Sardinia is an island in the south of Italy and is the second-largest island in the Mediterranean Sea, as shown in Fig. 9., which has the characteristics of frequent fire occurrences. In the last decade, 1008 fires per year have been recorded only in Sardinia, which is 20% of the total fires at the national level (J et al. 2021). This is a windy island with somewhat rainy winters, hot sunny summers, and an average temperature range of 10ºC in winter (January/February) to 24/25 ºC in summer (July/August).

As a demonstration, an image on the southern part of this Mediterranean island was selected from the archived data shown in Fig. 11. This image [acquired on 16/06/2021] comprises Monte-Arcosu Forest, one of the immense holm oak forests

of the Mediterranean region, which falls on the East of Cagliari city. The region of interest has a hilly and mountainous system with around 800m altitude and a total area of 32 km². Found in this forest is holm oak (Quercion ilicis) and mastic scrubs of two different families (Ericion arboreae and Oleo Ceratonian). The highest areas have low vegetation, specifically, the meadows of two different families (Teucrion mari and Periballio-Trifolion subterranei) whereas the lowest areas (around 200-300m altitude) have evergreen broadleaved trees (Quercetalia ilicis) (L. Mossa et al. 2016)(Caudullo et al. 2016).
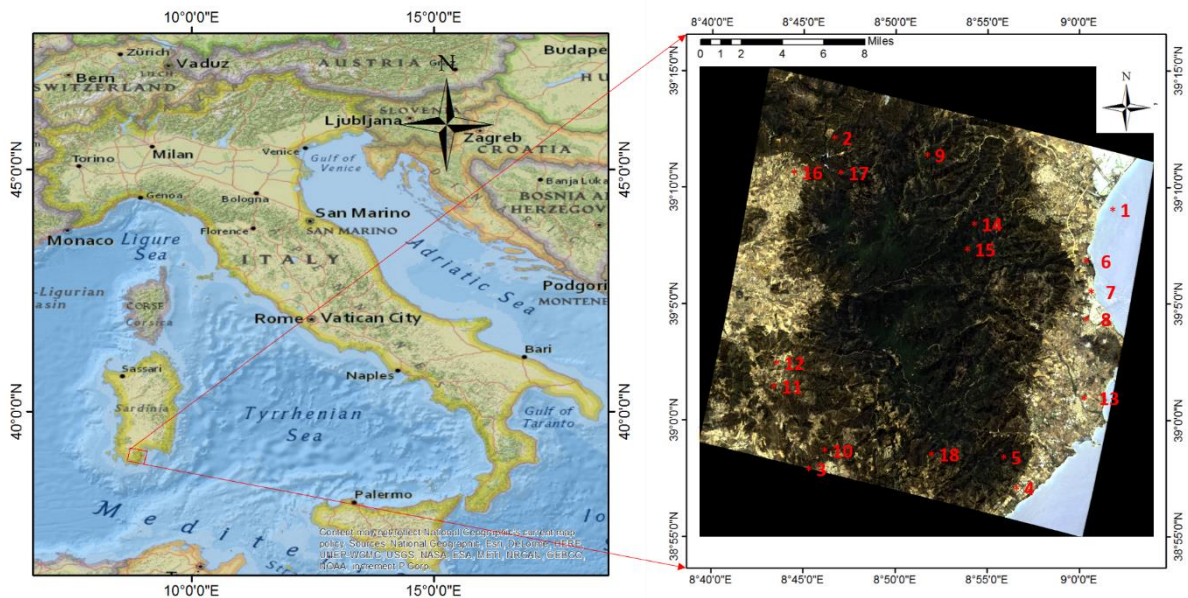
Fig 11. Geographic location of the image considered for processing [images are provided by e-geos under ASI-HYP project].

3.3. Materials and Methods

3.3.1. Pre-processing of Hyperspectral data
Level 2C and Level 1 products from the PRISMA archive with minimal cloud cover were considered. The atmospheric correction of the level 2C products is based upon inverting the radiative transfer model, i.e., minimizing a cost function representing the difference between the simulated spectrum and the measured one. The MODTRAN model has performed the simulations, and they are stored as a lookup-

table (LUT) to speed up the inversion. Geo-referencing of the image was carried out by creating a geographic look-up table (GLT) using the latitude and longitude values given in the image's metadata R software (Pepe et al. 2020). Further details about the mission and products are available in the PRISMA products specification document.

Removal of Deadlines: Fig. 12 shows the noisy lines of the PRISMA hyperspectral image on the region of interest. These lines are unstable and will be change depending upon the image. These lines were filled by assigning to a nearest value by linear interpolation.
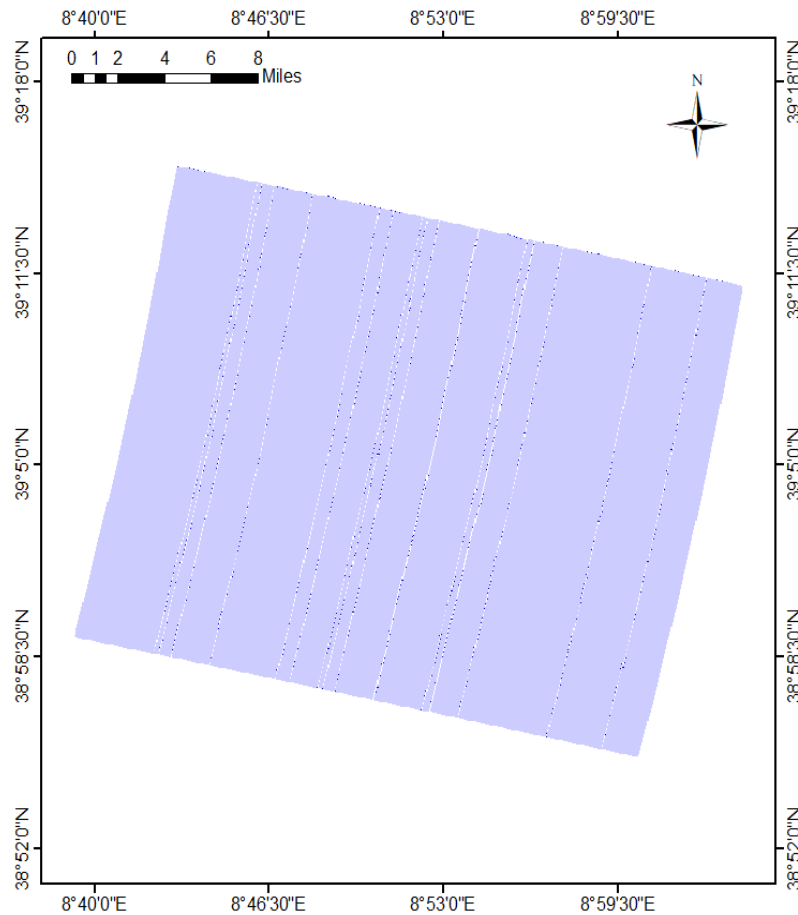
Fig 12. Noisy Lines on PRISMA Imagery

For most hyperspectral remote sensing applications, removing noisy bands is a required preprocessing step. In this work, noisy bands were removed by giving a threshold in algorithm that bands having greater than 20% as noisy values were removed. The 197 spectral bands in the 400 to 2500 nm range, with a spectral bandwidth within ~9–12 nm, were extracted from Level 2C data to perform the classification leaving 32 noisy and water absorption bands.

Extraction of Vegetation Pixels: Level 2C was considered for the fuel mapping, whereas the Level 1 product provides a basic land cover map with classes viz., water pixel, snow pixel, bare soil, cropland, forest, wetland, and urban component used to classify vegetation pixels from non-vegetated pixels as shown in Fig. 13. Thus, the processing time was reduced by applying the proposed procedure only to vegetation areas.
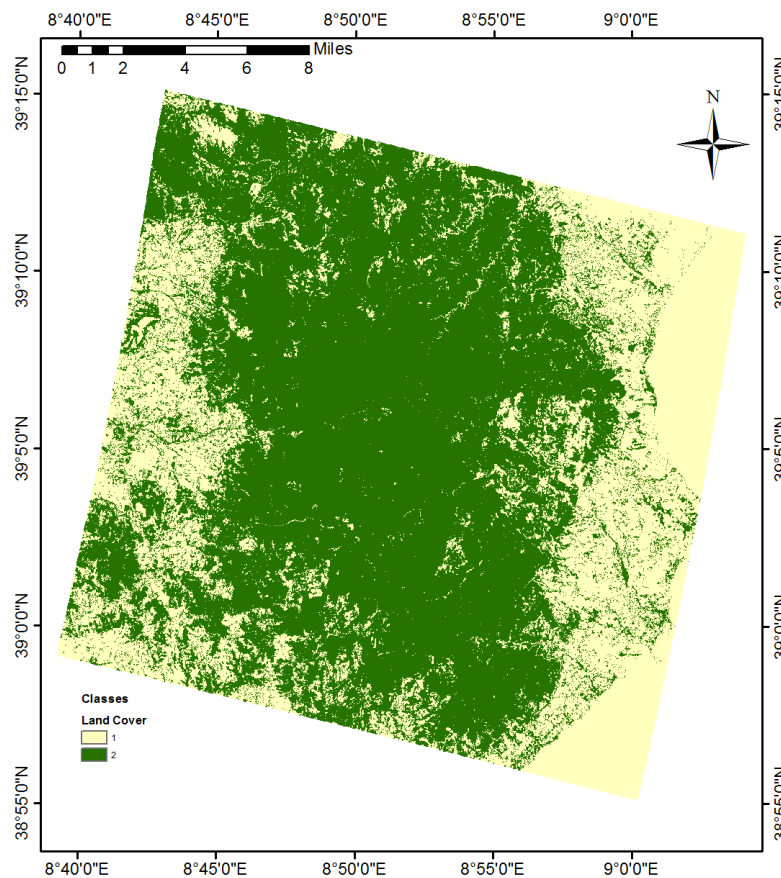
Fig 13. Classification Map (Vegetation and Non-Vegetation)

3.3.2. Reference Data

Reference data is necessary to train the machine learning model and to later validate the predicted output. Usually, remote sensing specialists conduct field campaigns to collect ground truth data as reference data, but field campaigns were not performed due to the COVID pandemic and also the goal is to use LUCAS points as input for the automatic algorithm. During the COVID situation, researchers around the world have tried other alternatives, such as using readily available maps / ground truth data collected by volunteers/ airborne data as the reference (Duveau 2021)(Jawak et al. 2021)(Global Development Lab, n.d.). In this work, Nature system map (Sardinia) accessed through Sardinia geoportal and CORINE land cover (CLC) and Grassland maps accessed from Copernicus Land Monitoring Service as reference data. The nature system map (Carta della natura) prepared by Italian National Institute for Environmental Protection and Research (ISPRA) is more detailed and accurate (Santarsiero et al. 2021)(Tucci et al. 2021) than the CLC having an accuracy of around 85% (Büttner et al., n.d.). Nature system map has 93 classes for Sardinian Island, CLC has 44 land cover types (Büttner et al., n.d.) at third level classification system for Europe whereas grasslands map shows presence/absence of grasslands. For the considered region of interest, the nature system map had 43 classes, among which 18 fuel types were selected, as shown in Fig. 14, depending upon the area covered by each class. These three maps were used to differentiate and cross-check the pixels corresponding to trees, shrubs, and grasslands. Three classes, namely coniferous vegetation, holm oak trees, and grasslands near the Mediterranean coast, were cross verified using CLC as shown in Fig 15 and grassland maps as shown in Fig 16.
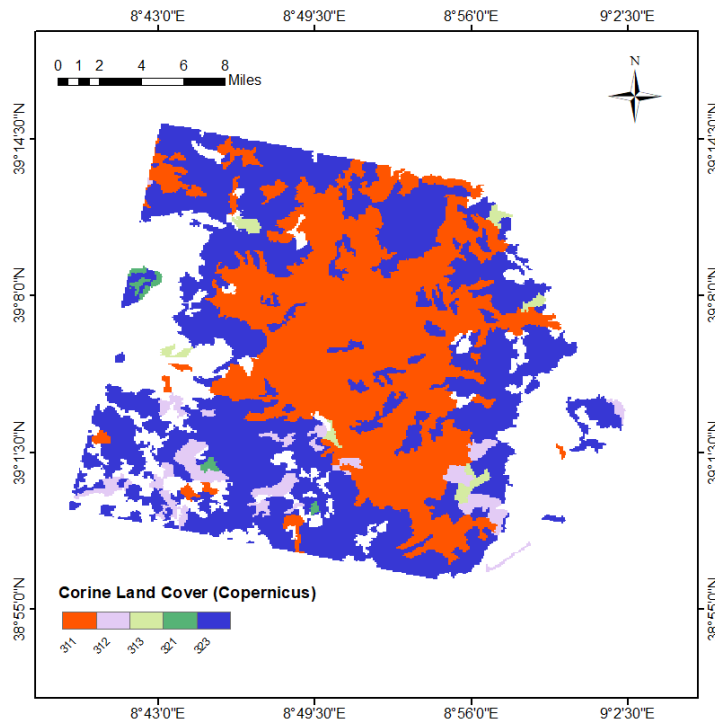
Fig 14. CORINE Land Cover Map
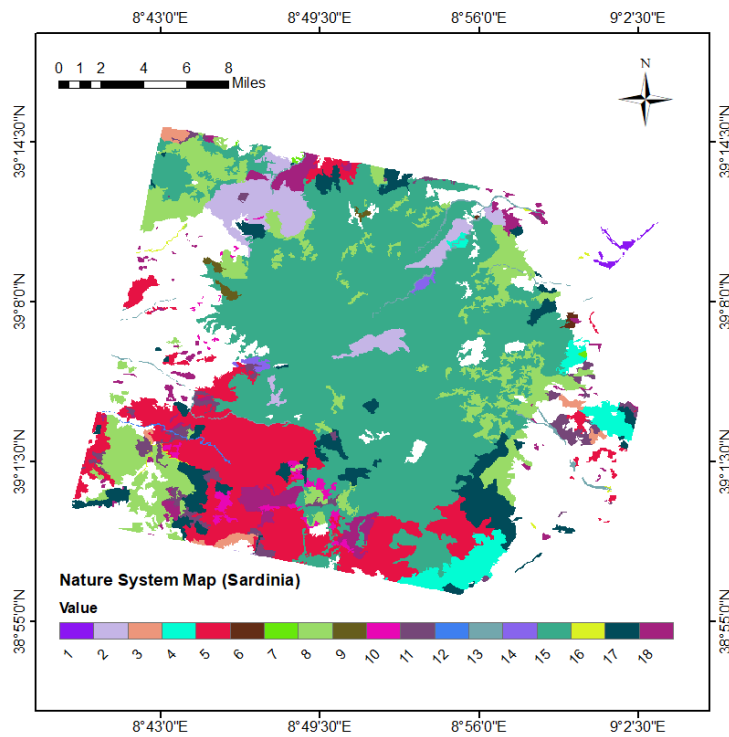
Fig 15. Nature System Map
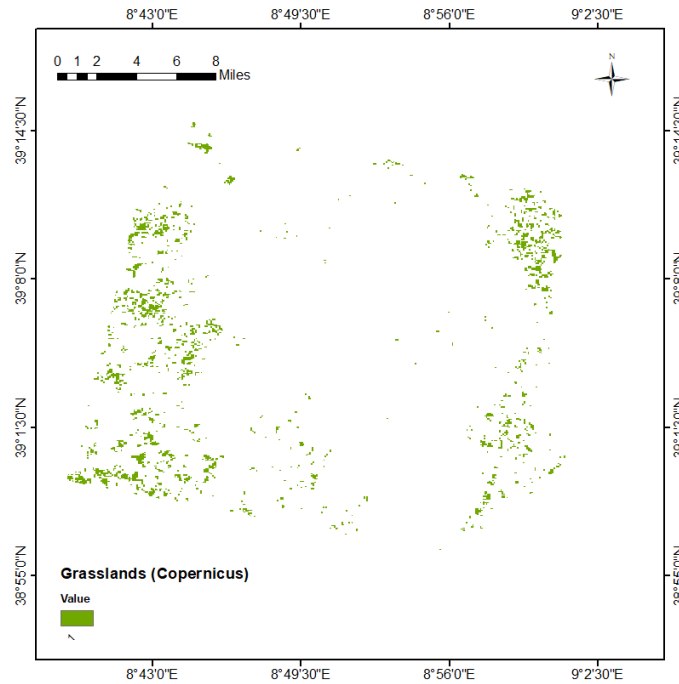
Fig 16. Grasslands Map

3.3.3. Pixel Extraction

Pixel's extraction of the HIS (Hyperspectral Image) is one of the imperative pre-processing mechanisms. It assists in handling the data and implementing the machine learning algorithms giving it as input data as shown in the flowchart (Fig. 4). The individual elements in this HSI are pixels of which the spectra are formed as vectors. Nature system map, CLC, and grassland maps obtained from sources such as Sardinia Geoportal and Copernicus Land Monitoring Service as described in section 3.3 were considered reference maps for input data. Pixels that correspond to fuel types were selected and inputted for dataset preparation. Fig. 11 shows the points selected for each vegetation type to be classified. Points marked in Fig. 11. represents: 1 - Halophyte vegetation with the dominance of annual succulent Chenopodiacea, 2 - Matorral of evergreen oaks, 3 - Matorral with olive and mastic, 4 - Matorral of Juniper, 5 - Low Olive and Mastic scrub, 6 - Low Shrubs (from Calicotome family), 7 - Formations at Euphorbia dendroids, 8 - Garrigues and

57

meso-mediterranean silicicole spots, 9 – Garrigue and meso-mediterraneal spots, 10 - Arid Mediterranean Meadow, 11 - Mediterranean Grassland (incl. Mediterranean and post-cultural sub-Mediterranean vegetation), 12 - Riparian Mediterranean Ash forest, 13 - Tamarisk and oleander, 14 - Tyrrhenian Cork, 15 - Sardinian Leccete (Holm Oak), 16 - Vegetation of reeds and similar species, 17 - Coniferous Vegetation and 18 - Eucalyptus plantations.

3.3.4. Techniques Used

Jeffries Matusita-Spectral Angle Mapper

Spectral Angle Mapper (SAM) is one of the popular techniques in the field of hyperspectral data analysis as it is a measure of the spectral angle between the reference spectra and the target spectrum. Angle decreases with increase in similarity between spectra.

$$\alpha = \cos^{-1}\left(\frac{\sum_{i=1}^{C} t_i r_i}{\sqrt{\sum_{i=1}^{C} t_i^2}\sqrt{\sum_{i=1}^{C} r_i^2}}\right) \qquad (1)$$

Given the test spectra t and a reference spectra r of length C, the SAM score α is calculated as in (1).

SAM has the ability to detect intrinsic properties of materials in terms of spectral angle but it is in-sensitive to shade and illumination effects. Thus, different materials/vegetation types having similar spectral shape with some offsets are classified with difficulty (Vishnu, Nidamanuri, and Bremananth 2013). To overcome this limitation, SAM is used in combination with the stochastic divergence measures (Chang 2004).

In the computation of transformed divergence or divergence, a priori probability of each spectral class is used as weights. The limitation of this approach is that divergence behaves as a function of normalized distance between the classes and

there will be a considerable difference from the behaviour of the probability of the correct match. Thus, Jeffries-Matusita (JM) distance measure was considered to combine with SAM for identifying the similar spectra. JM distance between two spectra is the measure of average distance between the spectra. The exponential factor involved in this method gives an exponentially decreasing weight to increasing separation between the spectra and this approach overcomes the limitation of transformed divergence (Laliberte, Browning, and Rango 2012). JM distance measure band wise information between spectral vectors (Padma and Sanjeevi 2014). JM distance between the target spectra (S_1) and reference spectra (S_2) can be represented as (2).

$$JM\ (S_1, S_2) = 2\ (1 - e^{-B}) \qquad (2)$$

Where Bhattacharya distance (B) measuring the mean (m) and variance (V) of the spectral vectors is defined as in (3).

$$B\ (S_1, S_2) = \frac{1}{8}(M_{S1} - M_{S2})^T \left[\frac{V_{S1} + V_{S2}}{2}\right]^{-1}(M_{S1} - M_{S2}) + \frac{1}{2}\ln\left[\frac{|V_{S1} + V_{S2}/2|}{\sqrt{|V_{S1}||V_{S2}|}}\right] \qquad (3)$$

In order to identify similar spectra, JM-SAM (TAN) was used in which the deterministic SAM was combined with stochastic JM distance using tangent function as it projects target spectrum and reference spectrum perpendicularly. This method considers both the geometrical aspects (angle, distance) and band-information between the spectral vectors. The least separable distance between the spectral vectors at each band along the least spectral angle between the vectors is considered to be the best match (Padma and Sanjeevi 2014; Chang 2004).

Guided Image Filtering

The guided filter is an edge preserving smoothing algorithm that could smooth out the fine details of the input image while retaining the sharp edges. Fine details could be noise, for example, a random pattern with a zero mean, or texture, such as a

repeated pattern with regular structure. So, applications of guided filtering include denoising, image mapping, dehazing and compression and tone mapping of high dynamic range (HDR) images (He, Sun, and Tang 2013, 2012; F. et al. 2017). Output image (q) can be obtained using input image (p) and a guided filter image (g) as in (4). Generally, q is a linear transform of g in a window ω_k centered at the pixel k. If the radius of k is r, the size of local window ω_k is (2r + 1)*(2r + 1).

$$q_i = a_k g_i + b_k \quad \forall i \in \omega_k \tag{4}$$

Where b_k and a_k are bias and linear coefficient which can be found as in (7) and (6), respectively. It can be observed from the model that output (q) will have a similar gradient with guidance image (g). Minimum cost function can be used to solve the bias and coefficient as in (5).

$$E\ (a_k, b_k) = \sum_{i \in \omega_k}((a_k g_i + b_k - p_i)^2 + \in a_k^2) \tag{5}$$

Here, $\in$ is the regularization parameter. Solution to this can be obtained from (He, Sun, and Tang 2013)

$$a_k = \frac{\frac{1}{\omega}\sum_{i \in \omega_k} g_{i-} - \mu_k - \overline{p_k}}{\sigma_k^2 + \in} \tag{6}$$

$$b_k = \overline{p_k} - a_k \mu_k \tag{7}$$

Where σ_k^2 and μ_k are the variance and mean of g in ω_k, $|\omega|$ is the number of pixels in ω_k, and $\overline{p_k}$ is the mean of p in ω_k. After obtaining the coefficient b_k and a_k, filtering output q_i can be computed. Through this process, linear transform image q can be obtained (Kang, Li, and Benediktsson 2014; He, Sun, and Tang 2013). Guidance image can be obtained by perform Principal Component Analysis (PCA). The first three principal components were considered as a color guidance image for the guided filtering process.

K-means clustering analysis

As it is a useful unsupervised learning technique that can divide unknown objects into several groups. The members in each group have similar characteristics and properties. K-means is a simple and popular machine learning algorithm used for clustering data where the number of clusters (K) is either known, presumed, or indicated beforehand. As per the suggestion of (Thai, Hai, and Thuy 2012) (Jones et al. 2020) it would be better if the number of clusters K is greater than the number of expected or actual classes, so three clusters were formed since it is a binary classification. The k-means algorithm was carried out using the Machine Learning Toolbox of MATLAB.

A certain initial number K of centroids of the given input data are determined randomly, then the data are divided in to several groups. The Euclidean distance (d) between data and centroids are calculated as in (8).

$$d\ (X_t, X_\epsilon) = \ \sqrt{\sum_{u=1}^{n}(X_{ut} - X_{\varepsilon u}^2)} \tag{8}$$

Where $X_t\ and\ X_\epsilon$ are input data and given centroids, respectively, l is the number of the properties and u is the data property.

By the first-time calculation of d, the result obtained is recorded as $D^{(o)} = \{D_1^{(o)},\ D_2^{(o)}, ... D_K^{(o)}\}$, and as the relationship shown in (9), the new centroids are updated.

$$X_\varepsilon^{(m)} = \ \frac{1}{h_\epsilon^{(m-1)}}\sum\nolimits_{X_t = D_{t\epsilon}^{(m-1)}} X_t \tag{9}$$

Where m is the number of iterations, $X_\varepsilon^{(m)}$ is the new centroid, $h_\epsilon^{(m-1)}$ is the amount of data in the new group based on new centroids. Iterating the above step and ending the calculation process when $D^{(m)} = D^{(m-1)}$ and $\epsilon^{(m)} = h\ \epsilon^{(m-1)}$. The obtained centroids are the clustering centroids of the data. Three groups were

formed having similar spectral signatures, dissimilar spectral signatures and very noisy spectral signatures respectively (Vakalis et al. 2004a; Jones et al. 2020).

Support Vector Machine for HSI Classification

There are numerous supervised learning-based algorithms in artificial intelligence field which can be applied for classification (Thai, Hai, and Thuy 2012). In the current framework, SVM (with Radial Basis Function, RBF) was applied because of its reputation in training data set to achieve high accuracy irrespective of the size of dataset and outstanding generalization capability. This method works on statistical learning theory and structural risk minimization principle (Guo et al. 2019). The optimal separating hyperplane with the maximum margin between the classes will be found using the strategy of this classifier using the training samples located at the edge of the class distribution (Thai, Hai, and Thuy 2012). The formula for the output of a linear SVM is shown in (10):

$$u = w.x - b \qquad (10)$$

Where x and w are the input and normal vectors respectively to the hyperplane. The separating hyperplane forms at the plane u=0 having the nearest points lying on the planes at u = ±1. The equation for margin m is shown in (11).

$$m = \frac{1}{||w||_2} \qquad (11)$$

Since it is a non-linear data, kernels are required for training the model. So, in our case, RBF kernels were implemented. RBF (Gaussian) kernels are a family of kernels where smoothening of distance measure is done by radian function (exponential function) (Cervantes et al. 2020; Sabat-Tomala, Raczko, and Zagajewski 2020), as shown in (12). This kernel, unlike the linear kernel, can handle the problem when relation between class labels and attribute is nonlinear and can map samples into a higher dimensional space (Maxwell, Warner, and Fang 2018).

$$k\left(x_i, x_j\right) = \exp\left(-\sigma\left|\left|x_i - x_j\right|\right|^2\right), \sigma > 0 \qquad (12)$$

The adjustable parameter plays a major role in the performance of the kernel and should be carefully tuned. If underestimated, the function will lack regularization and the decision boundary will be highly sensitive to noise in training data whereas if overestimated, the exponential will behave almost linearly. Highly sensitivity to noise in training data occurs at boundary so the complete behaviour of SVM depends on the choice of the width parameter (Thai, Hai, and Thuy 2012). Initially, the optimal values were found by hyperparameter optimization in classification learner app of MATLAB but observed slowly leading to overfitting. So, Bayesian optimization technique was applied to just optimize few parameters such as sigma, box constraint etc.

Then, the SVM model developed was allowed to find posterior probabilities by training parameters of an additional sigmoid function to map the outputs into probabilities. Constructing classifier to produce a posterior probability is very useful in practical recognition situations. For example, a posterior probability allows to make decisions using the utility model. Posterior probabilities play an important role in making overall decision when classifier has limitation of making a small part of an overall decision (Guo et al. 2019)

Linear Mixing Model

Linear mixing model is necessary when the pixel comprises of materials with different reflectance properties and the spectral variability within the scene results from varying proportions of the endmembers (Manolakis, Siracusa, and Shaw 2001; Heinz, Chang, and Althouse 2003). The spectrum of mixed pixel can be represented as linear combination of component spectra (endmembers) in LMM. The weight of each endmember (abundance) is proportional to the fraction of the pixel area covered by the endmember(Gewali, Monteiro, and Saber 2018). If there are L

spectral bands, the spectra of the endmembers and the spectrum of the pixel can be represented by L-dimensional vectors.

The general equation (Heinz, Chang, and Althouse 2003; Manolakis, Siracusa, and Shaw 2001)can be given as in (13), (14) and (15).

$$x = \sum_{k=1}^{M} a_k s_k + \omega \triangleq Sa + \omega \tag{13}$$

$$S \triangleq [s_1, s_2 \ldots s_M] \tag{14}$$

$$a \triangleq [a_1, a_2 \ldots a_M] \tag{15}$$

Where x = spectrum of the mixed pixel; s_k = spectra of the endmember; a_k = abundances of the endmembers; M = number of the endmembers; ω = L-dimensional error vector accounting for the lack-of-fit and noise effects. In this work, fully constrained LMM was implemented in which the LMM was with a following additivity constraint (Heinz, Chang, and Althouse 2003; Wei and Wang 2020) as shown in (16).

$$\sum_{k=1}^{M} a_k = 1 \tag{16}$$

3.3.5. Dataset Preparation

The flowchart shown in Fig. 17 illustrates the procedure followed to generate and pseudo-label the samples for the dataset preparation and is as follows:

Step 1: Pre-processing of PRISMA data was carried out as explained in section 3.2.

Step 2: HSI was denoised using the Guided image filtering technique as explained in section 3.5.2. It was performed on MATLAB software, giving the degree of smoothness parameter as 0.01.

Step 3: Spectral signatures corresponding to the pixels extracted following the procedure explained in section 3.4 were collected for all 18 classes. Since one of the

main objectives of this work is to create a dataset using a single spectral signature as input, only one pixel per class was extracted, and one spectral signature per class was considered.

Step 4: JM-SAM (TAN) was applied to collect similar and dissimilar spectral signatures from the image. This technique has provided us with a score map with values ranging from lower to higher according to the similarity of the given spectral profile. The score map was used to extract similar profiles by visually inspecting and giving a threshold, but an unsupervised clustering technique (K-means) was preferred to remove the threshold system.

Step 5: K-means clustering technique was applied to JM-SAM (TAN) scores to cluster the obtained values into three groups. Though we need only two groups (similar and dissimilar), three groups were formed referring to the literature as explained in section 3.5.3.

Step 6: A dataset of 500 samples was planned to be prepared for each class/fuel type by pseudo-labelling, as shown in Fig. 5. Spectral signatures corresponding to the pixels having up to 300 scores in group-1 (similar profiles) were collected and labelled 's''1', which refers to pure samples. Then, 200 spectral profiles were randomly collected using the scores of group-2 (dissimilar) and group-3 (noisy) and labelled 's''0', which refers to impure samples. This process of dataset preparation was repeated for each fuel type.

Step 7: This pseudo-labelled dataset was used for training and testing the SVM model (one vs all) for binary classification, due to which it is named a semi-supervised learning approach.
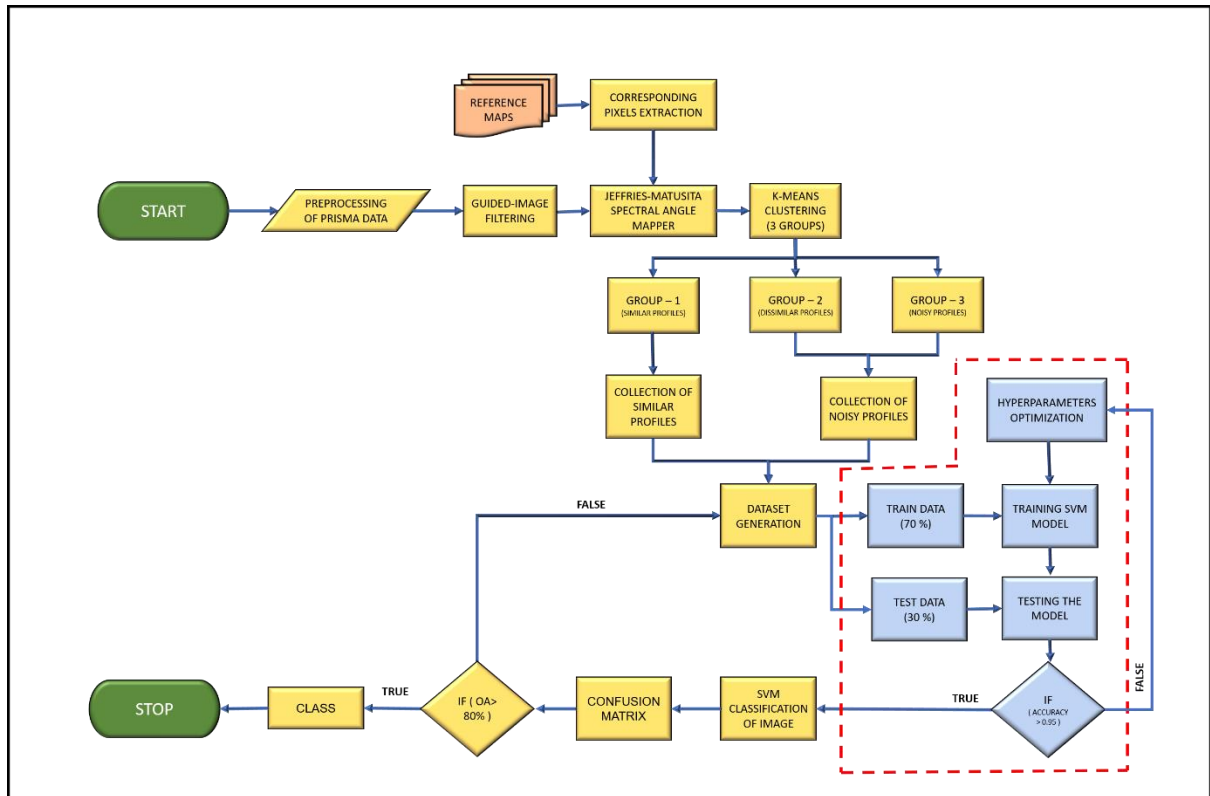
Fig 17. Process Flowchart of Dataset Preparation

3.4. Results and Discussions

3.4.1. Fuel Types Classification

Support Vector Machine classifier was considered for training using the generated dataset on MATLAB R2021b with Machine Learning Toolbox. In addition, accuracy implemented to assess the trained model performance is the ratio of correctly classified testing samples to the total number of testing samples. The procedure followed to perform training, testing, and predicting is as follows:

Step 1: Dataset was divided into two datasets: 70% dataset as training dataset and 30% dataset as testing dataset.

Step 2: K-fold cross-validation was performed with k as 10 to fit the model with a minor error.

Step 3: Hyperparameters given for tuning are as follows: Radial Basis Function as kernel, sigma of range [1e-5 1e+5], and Box constraint of range [1e-5 1e+5].

Step 4: Defined hyperparameters were optimized with Bayesian optimization on MATLAB Statistical Tool Box.

Step 5: The SVM classifier model was trained using the optimal hyperparameters and RBF as the kernel.

Step 6: The SVM posterior probability model was trained using the trained SVM classifier model as input. This step created the score-to-posterior transformation function (sigmoid function) and computed posterior probabilities for the samples classified as the positive class.

Step 7: The cross-validation classification model was trained to perform 10-fold cross-validation and to find classification (kfoldLoss). For every class, less than 5% of classification loss was obtained.

Step 8: The trained SVM posterior probability model was validated using the testing dataset for accuracy. If accuracy is greater than 0.95, the model was considered for prediction.

The same steps were repeated for every class, and classes obtained as output from the SVM classifier is shown in Fig. 18.
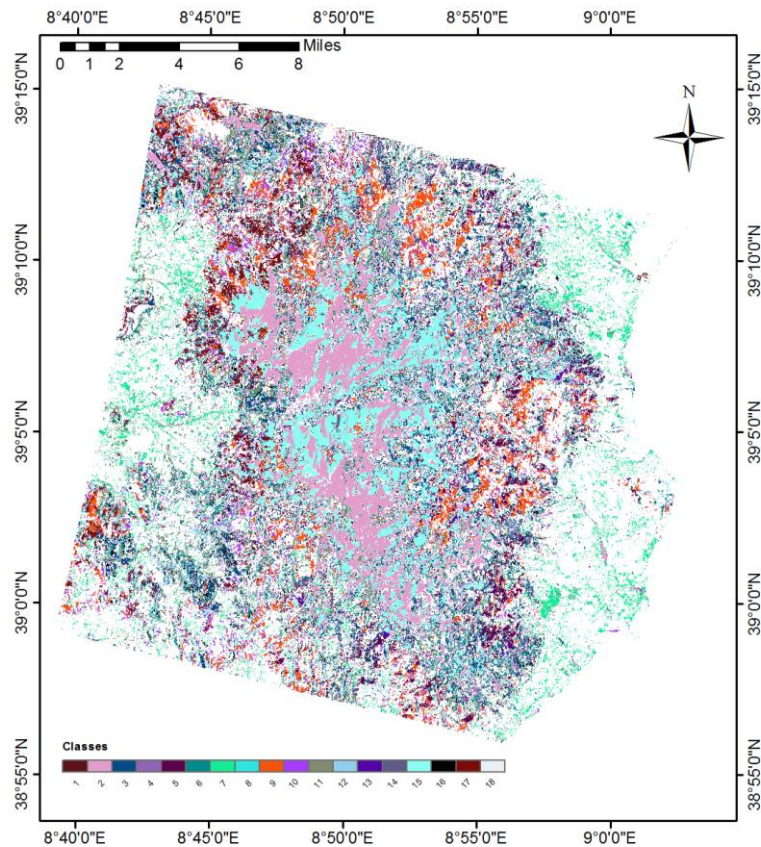
Fig 18. Classification Map of 18 classes

Fully constrained LMM was applied to unmix the unclassified pixels as per the method described in section 3.5.5. Before unmixing, classes (1 to 18) were categorized into three groups as forests comprising of classes (12, 14, 15, and 17), shrubs comprising of classes (1, 2, 3, 4, 5, 6, 7, 8, 9, 13 and 18) and grasslands comprising of classes (10, 11 and 16). Then, unmixing was carried out to identify the percentage of forests, shrubs, and grasslands in each pixel. The value for each pixel was assigned by knowing the percentage of each group in a pixel. Accordingly, mixed pixels were classified into six classes as, 111 – pixel with 50% forests and 50% unvegetated area, 112 – pixel with 50 % shrubs and 50% unvegetated area, 113 – pixel with 50 % of grasslands and 50% unvegetated area, 123 – pixel with 50 % forests, 20 % shrubs and 30 % grasslands, 231 – pixel with 50% shrubs, 20%

grasslands and 30 % forests and 312 – pixel with 50 % grasslands, 20 % forests and 30% shrubs. Fig. 19. shows the classification map obtained from fully constrained LMM.
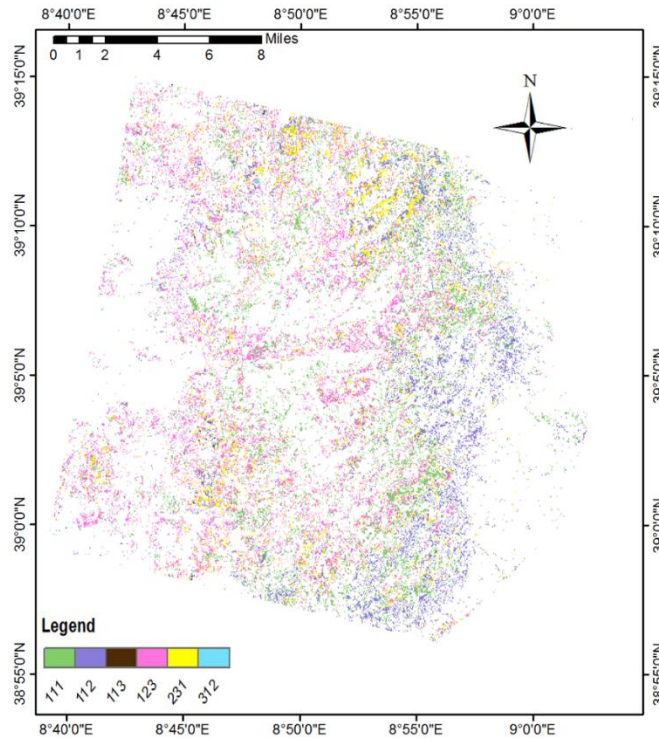
Fig 19. Classification Map of Mixed Pixels

3.4.2. Stability Analysis

In order to evaluate the robustness of the machine learning classifier algorithm, PRISMA hyperspectral imagery on the same region of interest for the different dates i.e., 27-06-2021 and 31-07-2021 were selected from the archive for fuel mapping.

Fig. 18. shows the fuel maps developed for two different dates according to the Anderson fuel models. Fig. 20 [left] shows the fuel map developed for 27-06-2021 on the imagery acquired on Lazio (Rome) comprising Castel Porziano. Fig. 20 [right] shows the fuel map developed for 31-07-2021 and is slightly rotated with respect to

the Fig. 20 [left]. Fuel values were assigned in the range of [1-10] for both the maps and the similarity between the maps can be observed.
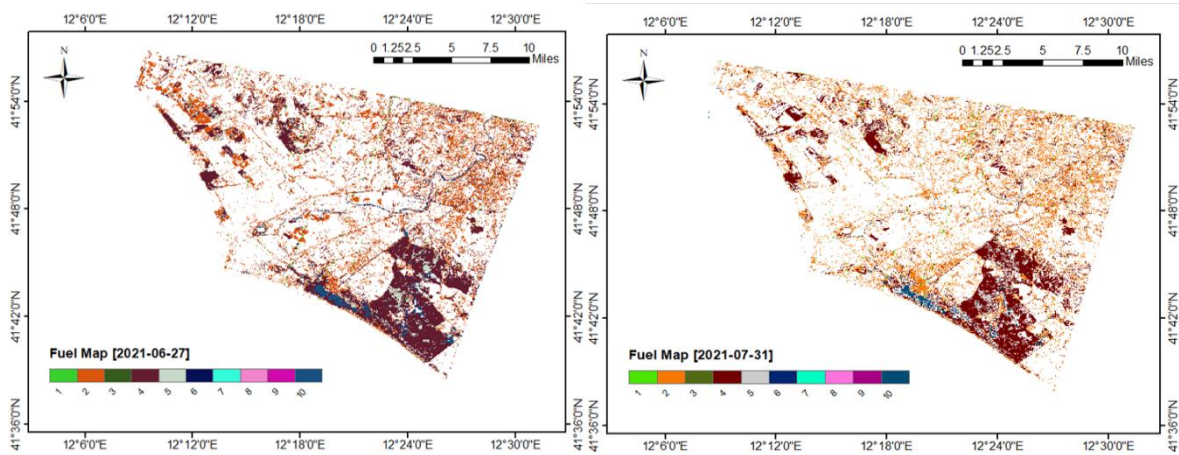
Fig 20. (left) Fuel Map [27-06-2021] and (right) Fuel Map [31-07-2021]

Since Fig 20 [right] is slightly rotated, a common region from both the images were selected for stability analysis. Images covering Castel Porziano clipped from both these images are shown in Fig 21 [left] and 21 [right]. Similarity between these two images can be observed from the Fig 21 and in terms of numerical values was given in the Table 10. NDVI was calculated for the ROI to compare the number of vegetated pixels among the two images as shown in Fig 22 and are mentioned in the same Table 10.

Stability of a learning algorithm refers to the changes in the output of the system when we change the training dataset. A learning algorithm is said to be stable if the learned model doesn't change much when the training dataset is modified. When selecting a training dataset from the same image in classification problem of PRISMA hyperspectral imagery, using cross validation, kfloss of less than 5 % was obtained which refers to greater than 95% stable. But this alone cannot be considered when the algorithm is developed generally for different images.

Mathematically, there are many ways for stability analysis such as hypothesis stability, cross validation etc.

Here, cross validation was performed between the two fuel maps developed using images on same region of interest but acquired on different dates.
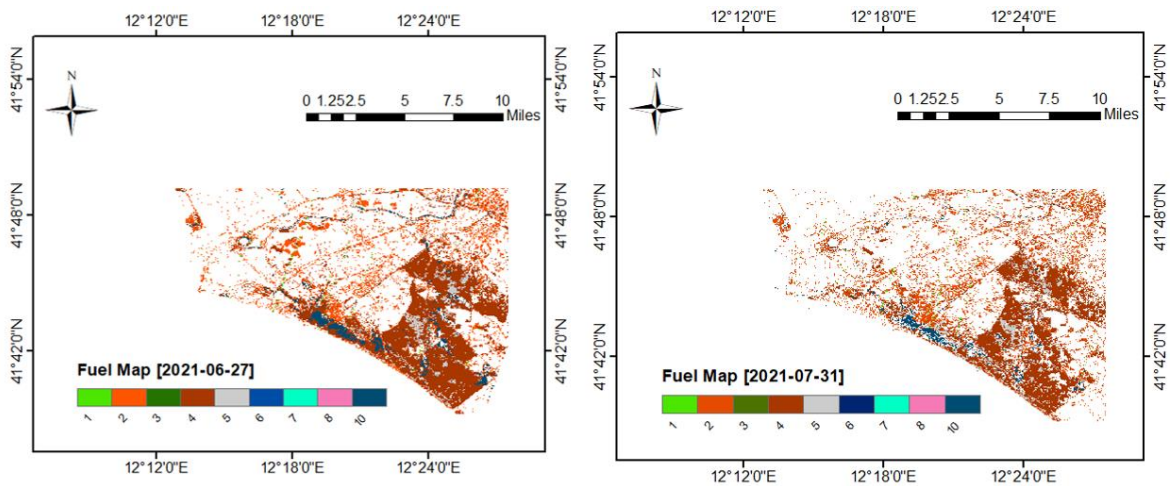
Fig 21. (left) Castel Porziano [27-06-2021] and (right) Castel Porziano [31-07-2021]
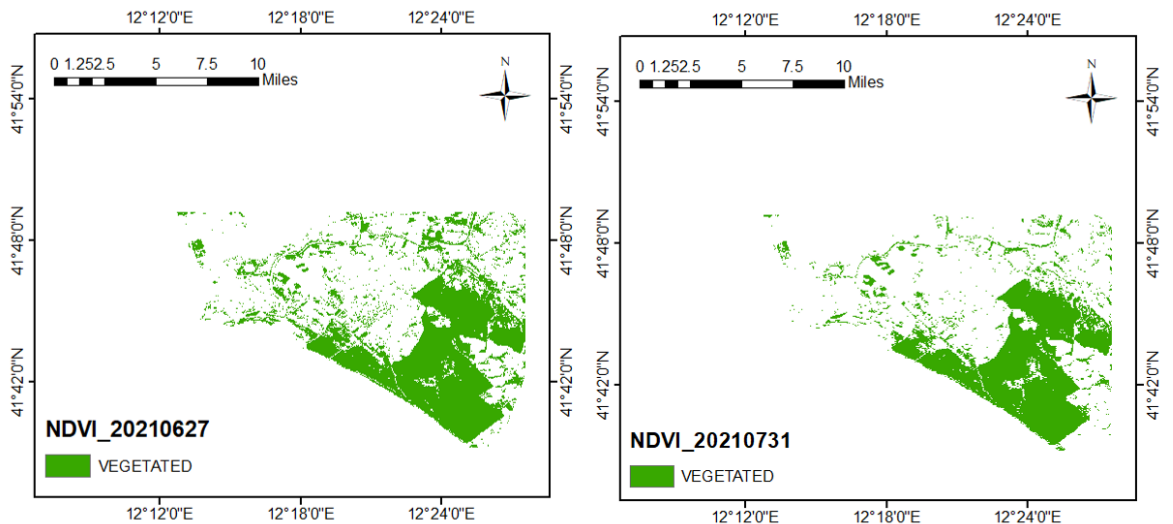
Fig 22. (left) NDVI Castel Porziano [27-06-2021] and (right) NDVI Castel Porziano [31-07-2021]

Table 8. Cross Validation of Images

Fuel Types Value	Number of Pixels on 27-06-2021 image	Number of Pixels on 31-07-2021 image	Difference (in %)

2	33255	32234	~ 3
4	57339	49117	~ 14
5	8259	7813	~ 5.4
10	7472	6155	~ 17
Vegetated	144030	118064	~ 18

Table 10 shows the number of pixels and difference between two images for each fuel type. Difference in number of pixels ranged from less than one percent to seventeen percent for specific classes. From the RGB of two images, it was observed that image acquired in July is not as dense as the image in June and it was proved by extracting the number of vegetated pixels in both the images using NDVI. Image acquired for 31-07-2021 has 18% less vegetated pixels than the image of 26-06-2021. Variation in density of vegetated pixels is in line with difference percentage of specific classes. Considering these difference percentages, it can be observed that overall stability / robustness of this algorithm can be given around 90%.

Apart from the variation in vegetated pixels, the other major difference between these two images is number of bands. Image on 31-07-2021 has higher number of noisy bands (22) in comparison with the previous image (4) which was also one of the reasons for variation in classification.

ANDERSON-BASED FUEL MAPPING

4.1. Introduction to Anderson fuel models

In the EFFIS and FUELMAP projects under JRC (Toukiloglou et al. 2013a), (Scott and Burgan 2005a), the correlation of vegetation types in Europe to Anderson fuel models was obtained. Under these projects, fuel of 42 types (as shown in Table 9) available in Europe were categorized into 9 groups as Peat bogs (FT_1 and FT_2), Grasslands (FT_3 to FT_6), Shrublands (FT_7 to FT_12), Transitional Shrubland/Forest (FT_13 to FT_19), Coniferous Forest (FT_20 to FT_28), Broadleaved Forest (FT_29 to FT_34), Mixed Forest (FT_35 to FT_38), Aquatic Vegetation (FT_39 to FT_41) and Agro-Forestry areas (FT_42). Then, the correlation of fuel types to the fuel models of Anderson (1982)(San-Miguel-Ayanz et al., n.d.) was made, as shown in the Table 11. A fuel map was generated by referring to these JRC-Anderson Codes in this work. This correlation was used in this work to correlate the classified fuel types to Anderson Codes (Anderson 1982), (San-Miguel-Ayanz et al., n.d.), (Toukiloglou et al. 2013a), (Scott and Burgan 2005a).

Table 9. Fuel Models (With correspondence to JRC)

FT Code	FT Description	Anderson Code
FT_1	Peat bogs	5
FT_2	Wooded peatbogs	6
FT_3	Pastures	1
FT_4	Sparse grasslands	1
FT_5	Mediterranean grasslands and steppes	2
FT_6	Temperate, Alpine and Northern grasslands	1
FT_7	Mediterranean moors and heathlands	5
FT_8	Temperate, Alpine and Northern moors and heathlands	5
FT_9	Mediterranean open shrublands (sclerophyllous)	2
FT_10	Mediterranean shrublands (sclerophyllous)	4
FT_11	Deciduous broadleaved shrublands (thermophilus)	5

Ft_12	Alpine open shrublands (conifers)	6
FT_13	Shrublands in Mediterranean conifer forest	7
F_T14	Shrublands in Mediterranean sclerophyllous forest	4
FT_15	Shrublands in Mediterranean mountain conifers forest	7
FT_16	Shrublands in thermophilus broadleaved forest	5
FT_17	Shrublands in beach and meso-phytic broadleaved forest	5
FT_18	Northern open shrublands in broadleaved forest	5
FT_19	Shrublands in Alpine and Northern conifers forest	7
FT_20	Mediterranean long needled conifer forest (Mediterranean pines)	10
FT_21	Mediterranean scaled needled open woodlands (Juniperus, Cupressus)	8
FT_22	Mediterranean mountain long needled conifer forest (black and Scots pines)	10
FT_23	Mediterranean mountain short needled conifer forest (firs, cedar)	8
FT_24	Temperate conifer plantation	8
FT_25	Alpine long needled conifer forest (pines)	10
FT_26	Alpine short needled conifer forest (fir, alp, spruce)	8
FT_27	Northern long needled conifer forest (Scots pines)	10
FT_28	Northern short needled conifer forest (spruce)	8
FT_29	Mediterranean evergreen broadleaved forest	4
FT_30	Thermophilus broadleaved forest	9
FT_31	Meso-phytic broadleaved forest	9
FT_32	Beach forest	9
FT_33	Mountain beach forest	10
FT_34	White birch boreal forest	10
FT_35	Mixed Mediterranean evergreen broadleaved with conifer forest	4
FT_36	Mixed meso-phytic broadleaved with conifer forest	9
FT_37	Mixed meso-phytic broadleaved with conifer forest	10
FT_38	Mixed beach with conifer forest	9
FT_39	Riparian vegetation	5
FT_40	Coastal inland and halophytic vegetation and dunes	1
FT_41	Aquatic Marshes	3
FT_42	Agroforestry areas	2

4.2. Further classification

Concerning the JRC-Anderson correlation [Table 9], Anderson codes differ for sparse grasslands from typical grasslands. According to the EFFIS project, sparse grasslands will have 1.83 tons/hectare of biomass (San-Miguel-Ayanz et al., n.d.). So, a biomass map was obtained from EU Copernicus and differentiated spare grasslands from grasslands. Fig. 23., shows the classification of sparse grasslands (class 2) from grasslands (class 1).
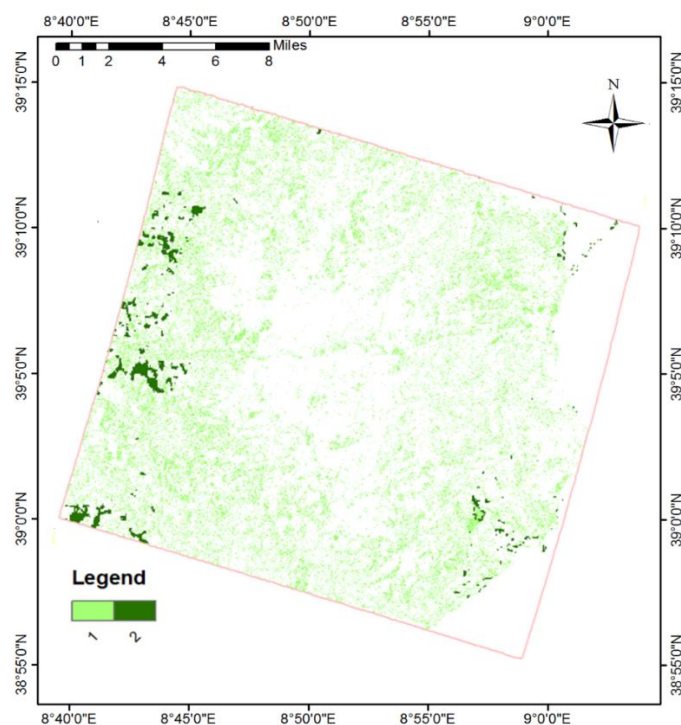
Fig 23. Classification of Sparse Grasslands

4.3. Fuel map generation

By referring to the correlation of JRC-Anderson Codes as shown in Table 11, Anderson codes were assigned to the pixels of classified map with respect to the fuel types as tabulated in Table 12. For mixed pixel, whichever the fuel type has higher percentage of occupancy, Anderson code corresponding to that fuel type was assigned.

Table 10. Fuel Types with correspondence to Anderson Codes

Class	JRC Fuel Type	Anderson Code
1	FT_40	1
2	FT_29	4
3	FT_10	4
4	FT_14	4
5	FT_14	4
6	FT_9	2
7	FT_9	2
8	FT_10	4
9	FT_10	4
10	FT_4	1
11	FT_4	1
12	FT_32	9
13	FT_42	2
14	FT_29	4
15	FT_29	4
16	FT_4	1
17	FT_20	10
18	FT_15	7

Fig. 24. shows the wildfire fuel map obtained by following the procedure described. The fuel map has values ranging from 1 to 10, representing the fuel models of Anderson's classification. By associating the classified fuel types to standard fuel models, each fuel type in this map is correlated to the attributes of fuel models such as fuel load [t/ha] for the living and dead component of the vegetation, the height of the fuel (litter) to the ground, extinction humidity [%], flame height [m] and propagation rate [m/sec] (San-Miguel-Ayanz et al., n.d.).
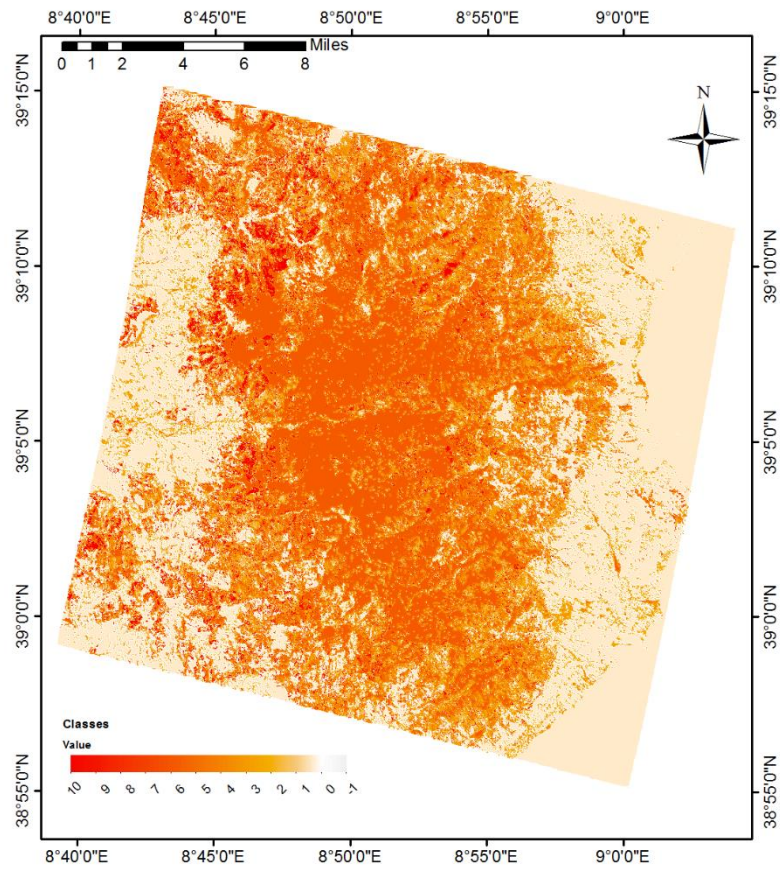
Fig 24. Wildfire Fuel Map

SCOTT/BURGAN-BASED FUEL MAPPING

5.1. Introduction to Scott/Burgan dynamic fuel models

In this chapter, Scott and Burgan's standard fire behavior fuel model (Scott and Burgan 2005b) was followed for dynamic fuel mapping. Their standard fire behavior fuel models were based on Rothermel's surface fire behavior fuel models. There are 52 fuel types as per the Scott/Burgan fuel model with the combination of 7 main fuel types as follows: Non-burnable (NB), Grass (GR), Grass-Shrub (GS), Shrub (SH), Timber – Understory (TU), Timber – Litter (TL) and Slash – Blowdown (SB). To facilitate both communication and computation, fuel types were represented with three-part reference scheme as fuel model number (between 1 to 256), fuel model code (three digits) and fuel model name (description with any number of characters) as shown in Table 13. For example, number – 102, code – GR2 and name – Low load, dry climate grass. The naming of the fuel model represents the dead fuel moisture extinction content and the climatic condition which is very useful while correlating the classified fuel types to the standard fire behavior fuel models. By correlating with these standard fuel models, it is possible to obtain fuel parameters such as fuel bed depth (ft), fine fuel load (t/ha), characteristic SAV (1/m), packing ratio (dimensionless), heat content (KJ/kg) and extinction moisture content (percent) (Scott and Burgan 2005b).

Table 11. Scott/Burgan Standard Fire Behaviour Models, Fuel Types and Fuel Numbers

Fuel Types	Fuel Codes	Fuel Number
Short, Sparse, Dry Climate Grass	GR1	1
Low Load, Dry Climate Grass	GR2	2

Low Load, Very Coarse, Humid Climate Grass	GR3	3
Moderate Load, Dry Climate,	GR4	4
Low Load, Humid Climate Grass	GR5	5
Moderate Load, Humid Climate Grass	GR6	6
High Load, Dry Climate Grass	GR7	7
High Load, Very Coarse, Humid Climate Grass	GR8	8
Very High Load, Humid Climate Grass	GR9	9
Low Load, Dry Climate Grass-Shrub	GS1	10
Moderate Load, Dry Climate Grass-Shrub	GS2	11
Moderate Load, Humid Climate Grass-Shrub	GS3	12
High Load, Humid Climate Grass-Shrub	GS4	13
Low Load, Dry Climate Shrub	SH1	14
Moderate Load, Dry Climate Shrub	SH2	15
Moderate Load, Humid Climate Shrub	SH3	16
Low Load, Humid Climate Timber-Shrub	SH4	17
High Load, Dry Climate Shrub	SH5	18
Low Load, Humid Climate Shrub	SH6	19

Very High Load, Dry Climate Timber-Shrub	SH7	20
High Load, Humid Climate Shrub	SH8	21
Very High Load, Humid Climate Shrub	SH9	22
Low Load Dry Climate Timber-Grass-Shrub	TU1	23
Moderate Load, Humid Climate Timber-Shrub	TU2	24
Moderate Load, Humid Climate Timber-Grass-Shrub	TU3	25
Dwarf conifer with understory	TU4	26
Very High Load, Dry Climate Timber-Shrub	TU5	27
Low Load, Compact Conifer Litter	TL1	28
Low Load Broadleaf Litter	TL2	29
Moderate Load Conifer Litter	TL3	30
Small downed logs	TL4	31
High Load Conifer Litter	TL5	32
Moderate Load Broadleaf Litter	TL6	33
Large Downed Logs	TL7	34
Long-Needle Litter	TL8	35
Very High Load Broadleaf Litter	TL9	36
Load Load Activity Fuel	SB1	37

Moderate Load Activity Fuel or Low Load Blowdown	SB2	38
High Load Activity Fuel or Moderate Load Blowdown	SB3	39
High Load Blowdown	SB4	40
Dwarf Conifer with Understory deciduous	TU4	126
Low Load Compact Conifer Litter Deciduous	TL1	128
Low Load Broadleaf Litter Deciduous	TL2	129
Moderate Load Conifer Litter Deciduous	TL3	130
High Load Conifer Litter Deciduous	TL5	132
Moderate Load Broadleaf Litter Deciduous	TL6	133
Long-Needle Litter Deciduous	TL8	135
Very High Load Broadleaf Litter Deciduous	TL9	136
Not burnable	-	50
Water bodies	-	51
Sea Water	-	52

The main objective of this work is to develop a dynamic fuel map with reference to the Scott/Burgan standard fire behaviour fuel models. Concerning this, PRISMA hyperspectral data were used to classify fuel types available in our area of study and then a Relative Greenness map was developed considering Sentinel – 2 multispectral data over the past 5 years. Referring to the iso-bioclimatic map

accessed from regional geoportal and fuel model naming, classified fuel types were correlated to Scott/Burgan fuel models. Procedure followed to develop dynamic fuel map is shown in Fig. 25.
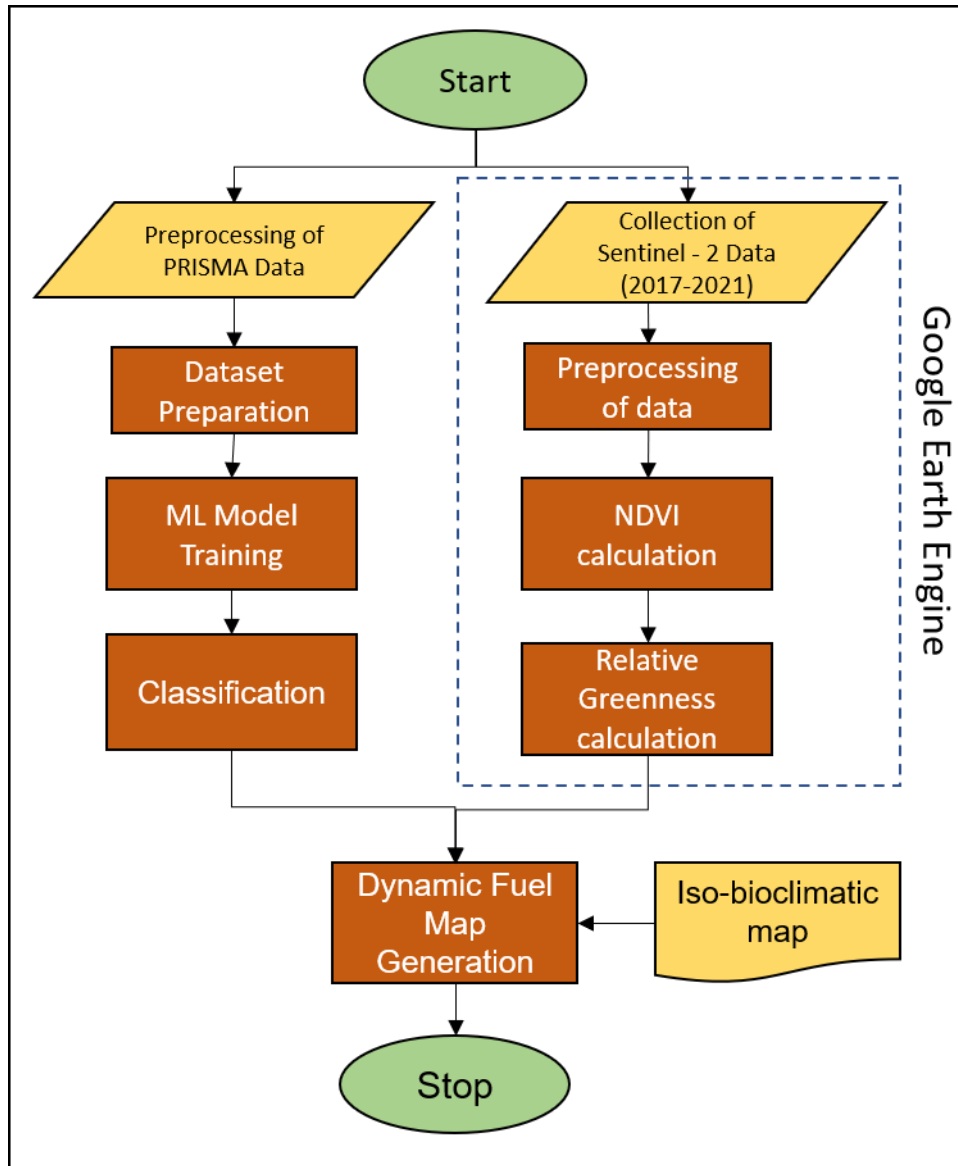
Fig 25. Procedure of dynamic fuel mapping

5.2. Study Area and Classification

An image [acquired on 26-06-2021] on the west of Latium was selected for demonstration purposes due to the availability of relevant data in the archive, as

shown in Fig. 26. This area is located between many small towns of Italy such as Tivoli, Olevano Romano etc., and is covered mainly by Oak trees. This is also the region with subhumid to humid climatic conditions, and the temperature in this area varied from 3.5° C to 30.5° C from winter to summer, respectively.
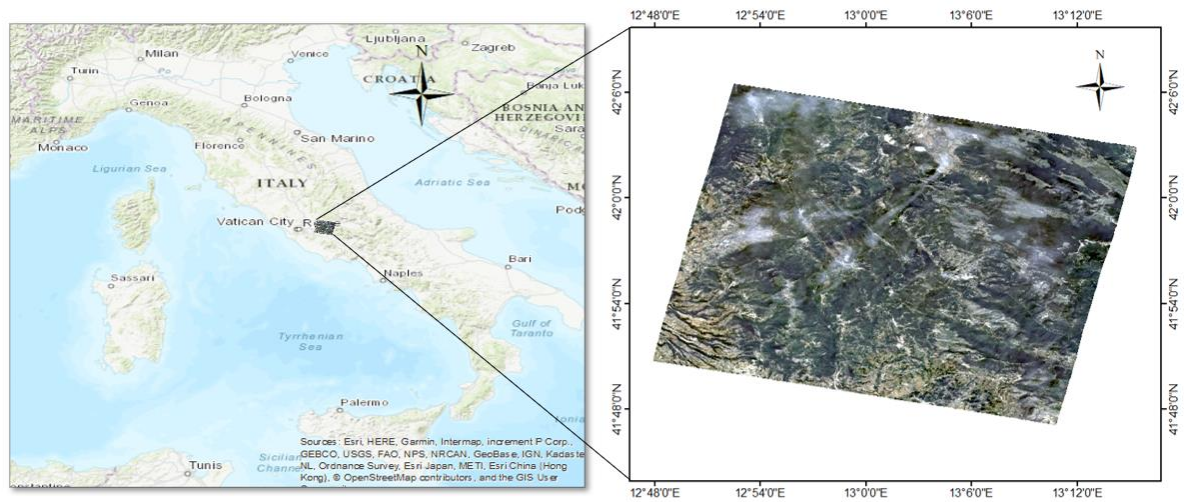
Fig 26. PRISMA Image of the Study Area.

5.3. Relative Greenness

Knowledge of the proportion of live and dead herbaceous fuel is essential in determining the fire danger. (Burgan, 1998 and Glenn, 2011) and has suggested that the relative greenness map can support us in finding the proportion of live and dead herbaceous in the area of study. Relative Greenness (RG) index can be represented as equation (17).

$$RG = \frac{NDVI - min_{5y}NDVI}{max_{5y}NDVI - min_{5y}NDVI} \cdot 100 \qquad (17)$$

Where $min_{5y}NDVI$ and $max_{5y}NDVI$ are the minimum and maximum NDVI values registered in each pixel in the past five years (Laneve, Pampanoni, and Shaik 2020). Whereas Normalized Difference Vegetation Index (NDVI) can be computed using equation (18).

$$NDVI = \frac{NIR - RED}{NIR + RED} \qquad (18)$$

Where NIR and RED are the reflectance values of near infrared and red channels.

Relative greenness map was generated in Google Earth Engine considering Sentinel–2 multispectral data over the past 5 years as shown in Fig 27. One image per month with a cloud pixel percentage of less than 10 was chosen for processing. Initially, maximum, minimum and on-date NDVI was calculated, and then the RG index as shown in equation (17) was applied to generate an RG map for the area of study. In Fig 27., RG value of 100 signifies that this is the highest greenness level ever reached during the multiyear period and vice versa. This map is further classified into three levels as low (1 - 30%), moderate (31 – 60%) and high (61 – 100%) RG levels according to the Scott/Burgan fuel model naming which is required for correlating to the fuel models appropriately.
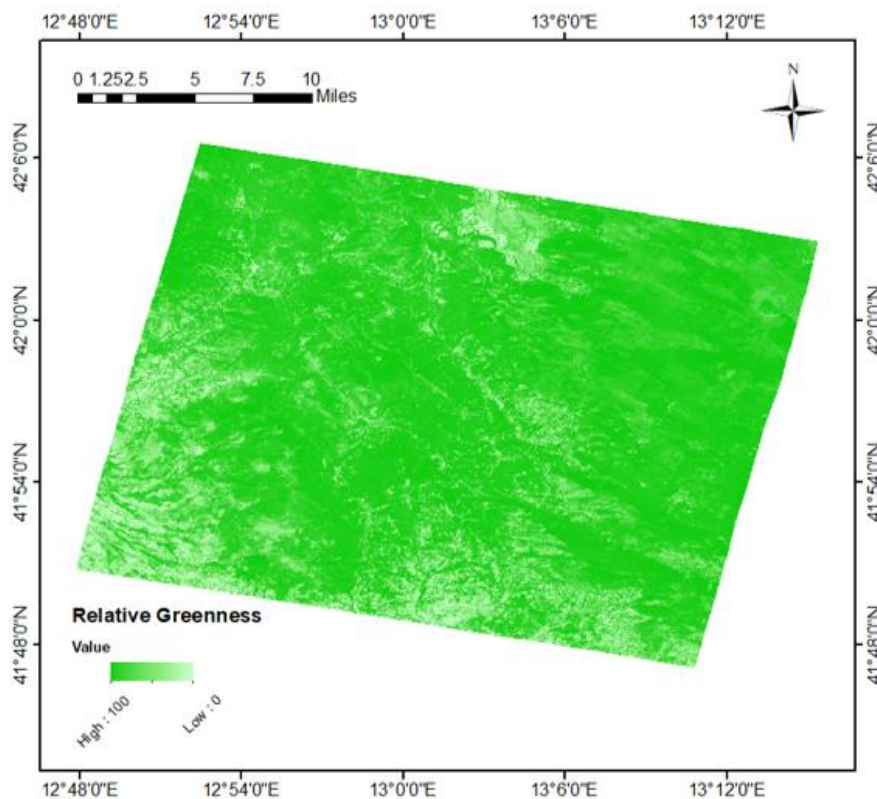
Fig 27. Relative Greenness Map

5.4. Fuel Map Generation

In order to generate dynamic fuel map with reference to the naming of Scott/Burgan standard fire behaviour fuel model, information from both classified and RG map was taken. Along with this, iso-bioclimatic map obtained from regional geoportal provided us the climatic condition of the study area. Considering these three inputs, dynamic fuel map was generated by assigning the fuel model number (between 1 to 256).

Fig. 28 shows the classified map for West-Latium of Italy, and classes labelled in the figure represents as follows: Not-burnable (-1), Beech Forest (1), Hornbeam (2), Chestnut (3), Downy Oak (4), Shrubland (5), Holm Oak (6), Oak Forest (7), Riparian Forest (8), Grasslands (9), Trees – Shrubs – Grasslands (123), Major Shrubs – Minor Grasslands (231) and Major Grasslands - Minor Shrubs (321).
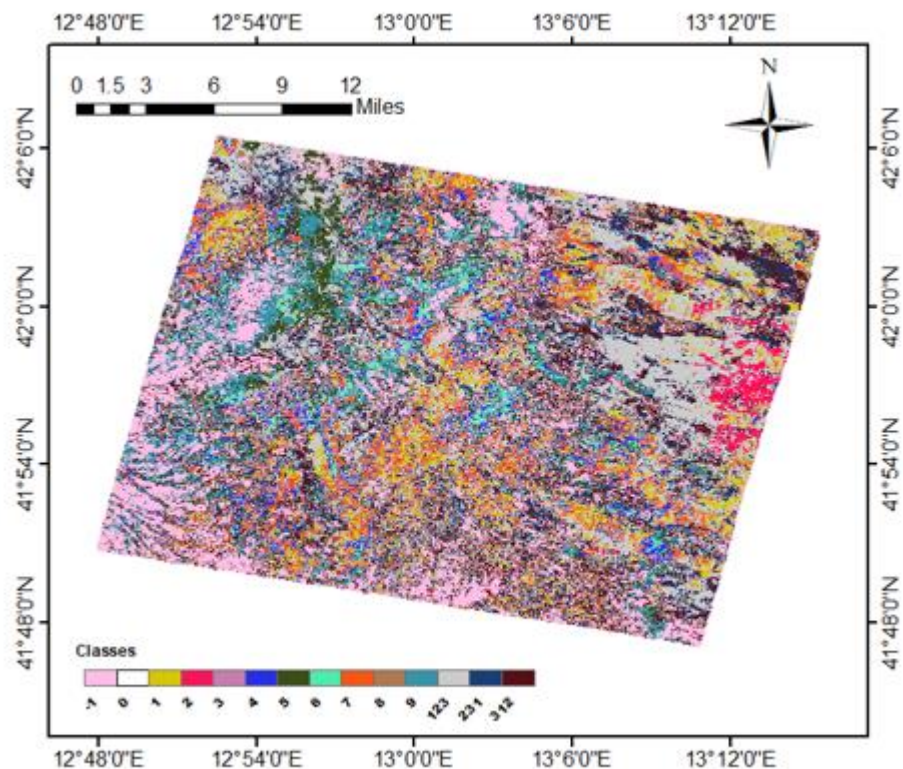
Fig 28. Classified Map for West-Latium

Fig. 29 depicts the dynamic fuel map generated as explained in section 5.4. The values of the fuel models in this map were assigned according to the fuel types available in this study area. Using this map, it is possible to correlate the standard fuel models (Scott/Burgan) parameters (Uddien Shaik, Giovanni, and Fusilli 2021). In addition, Scott/Burgan also considers the mixed fuel types, which is an advantage when using remote sensing systems to map fuel types.
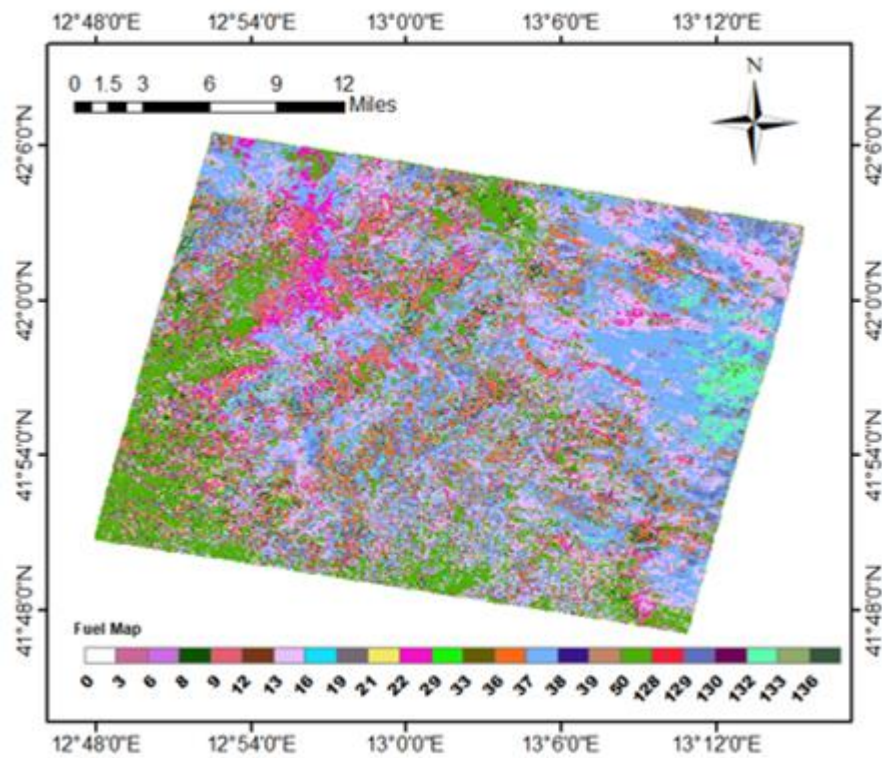
Fig 29. Dynamic Fuel Map

VALIDATION OF ALGORITHM

6.1. Validation with reference data

As per the methodology explained in the previous section, hyperspectral imagery of PRISMA on the south of Sardinian Island comprising of Monte-Arcosu Forest has been classified into 18 classes and 6 mixed-pixel classes as shown in Fig. 23 & 24. Details of classes are mentioned in section 3.3.3. (pixel extraction). It can be observed from the obtained maps that the significant fuel types available in this region of interest are fuel type 2 (evergreen oak), fuel type 15 (holm oak), and fuel type 5 (mastic scrubs/bushes), which is in align with the literature stating that this forest has these three vegetations majorly at different altitudes (L. Mossa et al. 2016; Caudullo et al. 2016). This region also contains Eucalyptus plantations (fuel type 18) which are highly flammable than the majorly covered broadleaved forest. Eucalyptus plants contain a high concentration of volatile compounds and accumulate larger amount of flammable litter from the leaves and barks (Pettinari and Chuvieco 2016).

One of the main factors of fire behaviour is how the fuels are distributed but understanding the fuel density heterogeneity effect on fire behaviour is limited. A study concluded that increased fuel density had decreased forward fire spread due to a combination of fuel discontinuities and increased fine-scale turbulent wind structures. In contrast, a decrease in local fuel continuity and wind entrainment into the forest canopy maintained near-surface wind speeds had driven forward fire spread. Considering this point, mixed pixels with partial vegetation are also necessary to be considered as fuel-containing pixels. In this work, mixed pixels were classified into six types as explained among which class 111 (50% forests and 50% unvegetated area) were in higher amount.

Table 12. Confusion Matrix of Classified Map

S.No	1	2	3	4	5	6	7	8	9	10	11	12	13	14	15	16	17	18	FN	Row Total	Commission Error (%)
1	20	0	0	0	1	1	2	0	0	0	2	1	0	0	1	2	0	0	9	30	30
2	1	26	0	0	0	0	0	0	0	0	0	0	0	0	3	0	0	0	4	30	13.33
3	0	3	24	0	2	0	0	0	0	0	1	0	0	0	1	1	1	0	9	30	20
4	0	2	0	26	0	0	0	0	2	0	0	0	0	0	0	0	0	0	4	30	13.33
5	0	0	2	0	26	1	1	0	0	0	0	0	0	0	0	0	0	0	4	30	13.33
6	0	0	0	0	0	25	3	0	1	0	0	0	0	0	0	0	1	0	5	30	16.67
7	0	0	0	0	0	0	28	0	2	0	0	0	0	0	0	0	0	0	2	30	6.67
8	0	0	0	2	0	0	0	27	1	0	0	0	0	0	0	0	0	0	3	30	10
9	0	0	0	0	0	0	2	0	26	0	2	0	0	0	0	0	0	0	4	30	13.33
10	0	0	0	1	0	1	0	0	0	26	0	0	0	0	0	0	0	2	4	30	13.33
11	0	0	0	0	0	0	0	0	0	2	27	0	0	0	0	0	0	1	3	30	10
12	0	0	0	0	0	0	0	0	1	0	0	28	0	0	0	0	1	0	2	30	6.67
13	0	0	2	1	0	0	0	0	0	0	0	0	26	0	0	0	0	1	4	30	13.37
14	0	1	0	0	0	0	0	0	1	0	0	0	0	28	1	0	0	0	2	30	6.67
15	0	0	0	0	0	0	0	0	2	0	0	0	0	0	27	1	0	0	3	30	10
16	0	0	0	0	0	0	0	0	1	0	0	0	0	0	0	27	1	1	3	30	10
17	0	0	0	0	0	0	0	0	0	0	0	0	0	0	0	0	29	0	1	30	3.33
18	0	0	0	0	0	2	0	0	0	0	0	0	1	0	0	1	0	26	4		13.33
FP	1	5	4	4	3	5	7	0	11	2	5	1	1	0	6	5	4	6	70/68		
Column Total	22	31	28	30	29	30	35	27	37	28	32	29	27	28	33	32	33	32		510	
Omission Error (%)	4.54	16.12	14.28	13.33	10.34	16.67	20	0	29.72	7.14	15.62	3.44	3.73	0	18.18	15.625	12.12	18.75			OA = 86%

The classified map was validated using different sources, i.e., the nature system map of Sardinia, CLC, and grasslands maps, accessed from regional/or EU Copernicus geoportals as described. Each class was validated by randomly taking 30 points to measure the classification accuracy, which is the ratio of correctly classified points to the total number of points. Table 14 shows the confusion matrix validated using 30 points for each class and the overall accuracy of 86% was achieved.

Table 15. Performance Metrics

Class	Precision	Recall	F1 Score	Accuracy (%)
1	0.95	0.70	0.80	70
2	0.83	0.86	0.85	86
3	0.85	0.72	0.78	80
4	0.86	0.86	0.86	86
5	0.89	0.86	0.88	86
6	0.83	0.83	0.83	83
7	0.80	0.93	0.86	93
8	0.86	0.90	0.94	90
9	1	0.86	0.77	86
10	0.70	0.86	0.89	86
11	0.92	0.90	0.87	90
12	0.84	0.93	0.94	93
13	0.96	0.86	0.91	86
14	0.96	0.93	0.96	93
15	1	0.90	0.85	90
16	0.81	0.90	0.87	90
17	0.84	0.96	0.92	96
18	0.87	0.86	0.83	86

Performance metrics for each class was identified to check the accuracy of the machine learning model. Performance metrics involve precision, recall, and F1 score for analyzing. Therefore, these scores take false positives and false negatives together into account. Understanding F1 score is intuitively not easy as accuracy, but F1 is usually more beneficial than accuracy, especially if the uneven class

distribution is present. Accuracy works best if false positives and false negatives have similar costs. In the case of different false positives and false negatives, it is better to look at Precision and Recall.

Table 13 shows each class's precision, recall, and F1 score. This image's major fuel types (class 2, 5, and 15) have obtained 86%, 86%, and 90% accuracy. Almost every class has obtained an accuracy of above 80% except class 1. It was observed that halophyte vegetation (class 1) is spread over the forest in small areas, but the reference map shows only near the Mediterranean coast, leading to less accuracy.

The validation details showed an Overall Accuracy of 87.10%, which is the ratio of correctly classified points for all classes to the total number of points. Due to the lack of recent reference/ground truth data to validate, the uncertainty of ±5 % inaccuracy can be expected. EFFIS pan-European fuel map was prepared using CLC having 8 vegetation classes/fuel types with 250m of spatial resolution and at an accuracy of around 85% (San-Miguel-Ayanz et al., n.d.). Fuel map under the framework of the ArcFuel project was prepared using CLC and Landsat – 7 data with eight fuel types at a resolution of 50m and obtained an accuracy of 76% in Italian pilot sites (Bonazountas et al. 2014; Toukiloglou et al. 2013b). Comparison with other fuel products is problematic since regional fuel maps use many different classification systems to produce (Pettinari and Chuvieco 2016).

6.2. Validation with ground data

To evaluate the repeatability and reproducibility of the algorithm, an image (of 19th January 2022) on the part of Bulgaria was selected since a fuel map acquired from the local authorities is available as a reference. The classification and fuel map are generated for this image with six classes, as shown in table 16. The input for this image was taken from the specified reference map, as shown in Fig 30a.

Table 16. Fuel Types and its corresponding Anderson Fuel Models

S.No.	Fuel Types	Anderson fuel models
1	Winter Oak	Mesophytic Broadleaved Forest (9)
2	White Pine	Broadleaved with Coniferous Forest (9)
3	Black Pine	Broadleaved with Coniferous Forest (6)
4	Hairy Oak	Agroforestry (2)
5	Pasture and Meadows	Pastures / Sparse grasslands (1)
6	Mixed Land Use	Pastures / Grasslands (1)

Fig. 30b shows the classification map with six classes and its corresponding fuel map in Fig. 30c. Again, the fuel Map based on PRISMA is clipped for the region of interest. Details of classes and the Anderson codes are shown in table 16.
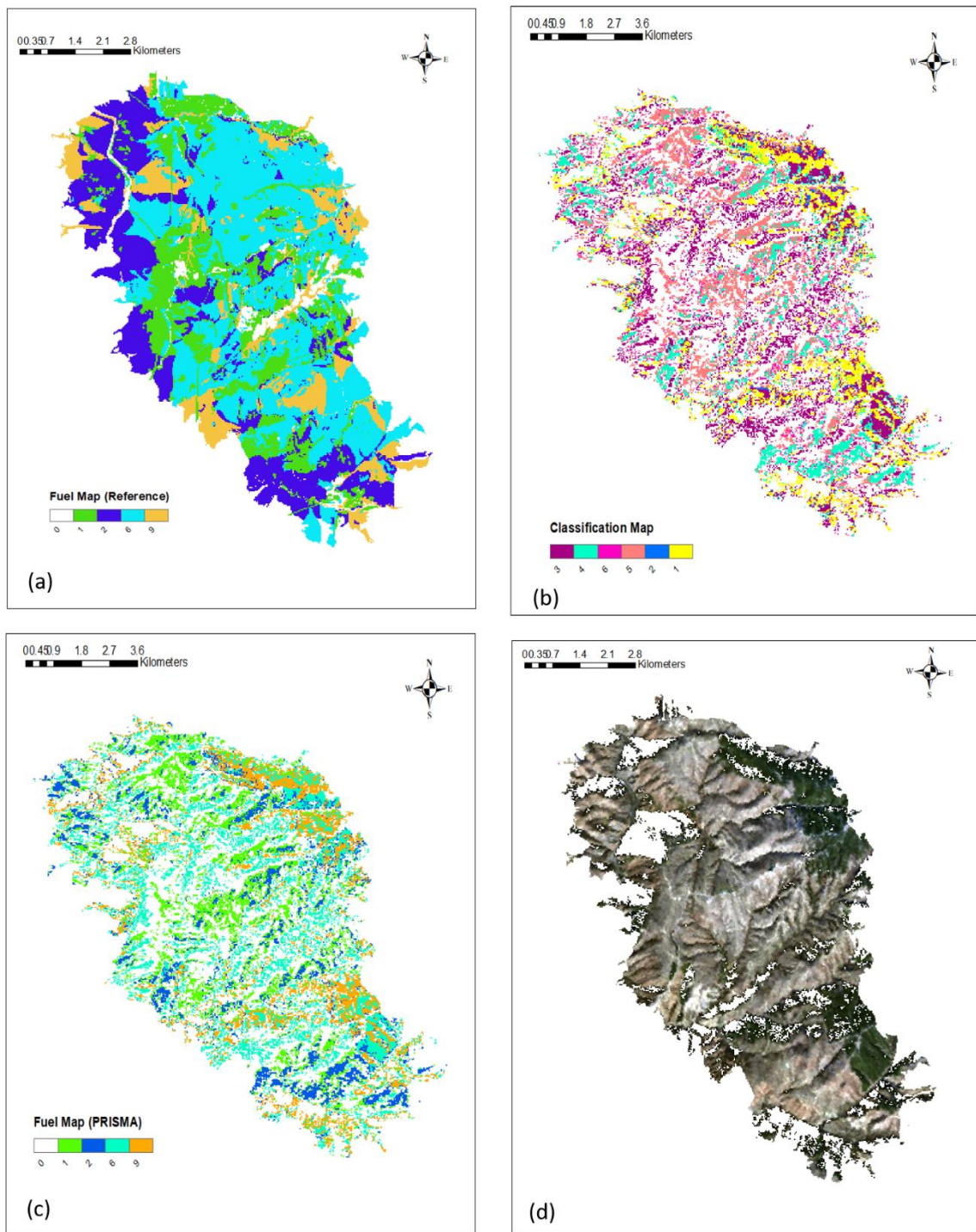
Fig 30. (a) Reference Fuel Map (Courtesy of FirEUrisk project) (b) Classification Map (from PRISMA) (c) Fuel Map (from PRISMA) and d) RGB (from PRISMA)

Reference fuel map has fuel types assigned to only four fuel models (1,2,6, and 9). The major vegetation available in this area is Black Pine (coniferous forest), followed

by other fuel types, as shown in table 16. This scenario is also similar to PRISMA based fuel map except that the fuel types assigned to fuel model 9 have sparse vegetation, which is inadequately classified due to the dark pixels in the hyperspectral data (as shown in RGB of PRISMA image).

Table 17. Confusion Matrix for Fuel Types

S.No.	1	2	6	9	User's Accuracy	Commission Error (%)
1	27	2	1	0	0.90	10
2	2	24	4	0	0.80	20
6	0	1	26	3	0.86	13.33
9	0	1	3	25	0.86	13.33
Producer's Accuracy	93.10	85.17	76.47	89.65		
Omission Error (%)	6.89	14.28	23.52	10.34		OA ≅ 84%

Detailed evaluation, including misclassifications, can be shown only by the confusion matrix in Table 17. A confusion matrix was created by considering 30 points for each category in the fuel map and obtained an overall accuracy of ≅ 84 %. It can be observed from the overall accuracies that the degree of confidence obtained is greater than 95%.

6.3. Validation with field data

Field campaigns were conducted to collect information on the fuel/vegetation types in the areas. Three areas within Lazio and Sardinia were selected for field campaign are (i) north-east Latium, (ii) south-east Sardinia and (iii) north Sardinia and the images for them were acquired on 28-06-2021, 16-06-2021 and 12-08-2021 respectively. Fig. 31 shows the ROIs on map and details of them are explained in the following sections.

Fig 31. Validation Areas

6.3.1. North - East Latium

The area, around the lake Bracciano comprises the Parco Naturale Regione of Bracciano-Martignano. The forest, which occupy more than 30% of the entire surface of the park, is distributed above all in the northernmost part and is characterized by a stand with a clear prevalence of chestnut and Turkey oak coppices as well as by areas with high trunk of Turkey oak and beech. On very steep and often rocky slopes and, in particular, on the hills facing north and west of the lakes of Bracciano and Martignano, among the evergreen species is the holm oak (Quercus ilex). The holm oak groves are sometimes interrupted by small groups of deciduous trees consisting of downy oak (Quercus pubescens), black hornbeam (Ostrya carpinifolia), ash (Fraxinus ornus), elm (Ulmus minor) and hackberry (Celtis australis). However, there is no lack of areas invaded by dense thicket of blackthorn (Prunus spinosa), hawthorn (Crategus monogyna), dogwood (Cornus

mas), broom of charcoal burners (Citysus scoparius) and the common broom (Spartium junceum) whose blooms in spring turn yellow intense these areas. Turkey oak (Quercus cerris) is the most widespread oak in the area and represents the main constituent component of extensive wooded areas governed by coppice, which form the backdrop to the northern and western shores of Lake Bracciano.

6.3.2. South-East Sardinia

The area comprises Monte Arcosu Forest, one of the largest holm oak forests of the Mediterranean region, which is east of Cagliari. The region of interest is hilly with an altitude of around 800 m and a total area of 32 km². The primary vegetation in this forest is holm oak (Quercion ilicis) and mastic shrubs of two different families (Ericion arboreae and Oleo ceratonian). The highest areas have low vegetation, specifically meadows of two different families (Teucrion mari and Periballio-Trifolion subterranei), whereas the lowest areas (around 200–300 m altitude) have evergreen broadleaved trees (Quercetalia ilicis).

The three PRISMA images corresponding to the above-described test sites were trained using the input data from three different reference maps such as fire fuel map (for Bulgaria), CNAT (for Sardinia) and forest types map (for Latium) respectively.

6.3.3. North-Sardinia

This area comprises of a commune of Alghero and the major vegetation found in this area are different types of shrubs mainly the large juniper bushes. This area has a Mediterranean coast on one side due to which the sand is more saline and can

observe discontinuous vegetation. The Figure (Fig 32) shows the areas visited during field campaigns.
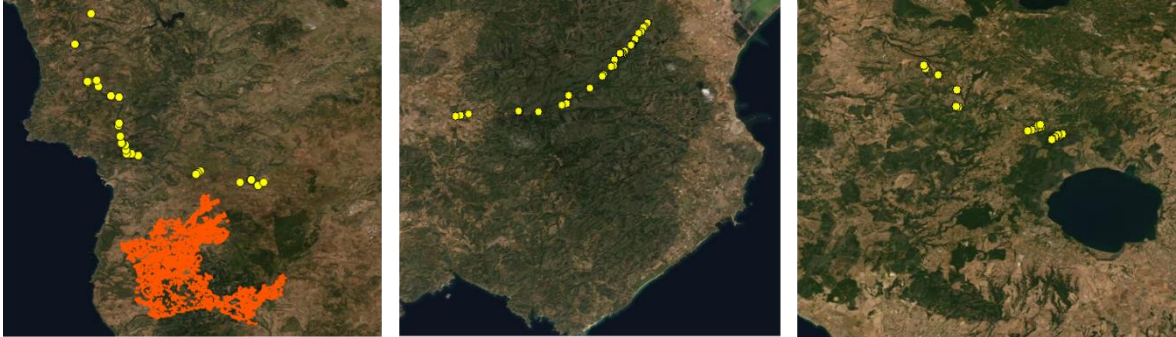
Fig 32. Validation Points for (i) North-West Sardinia, (ii) South-West Sardinia and (iii) West Latium

The following table list the fuel types (according to Anderson) encountered in the field campaign.

Table 13. Fuel models encountered during the field campaigns

Fuel model	FT description	Photo
0	Agriculture land	
1	Pastures	

2	Mediterranean Grasslands and Steppes	
4	Mediterranean shrublands (sclerophyllous)	
7	Shrublands in Mediterranean coniferous Forest	
9	Mesophytic broadleaved forest	
10	Mesophytic broadleaved forest with conifer forest	

Point based validation was also carried out for the three fuel maps by conducting the field visits. Totally 82 points were collected for the validation and they are organized into confusion matrix. Photographs were taken on four different

directions (North/East/West/South) and the visits were carried between February and March 2022.

Three images corresponding to this validation points are on South-West Sardinia, West Latium and North-West Sardinia. South-West Sardinia has classified the vegetation types corresponding to fuel models as follows: Cropland (0), Mediterranean grasslands and steppes (2), Mediterranean shrublands (sclerophyllous) (4), Deciduous broadleaved shrublands - thermophilus (5), Shrublands in Mediterranean coniferous forest (7) and Mixed mesophytic broadleaved with conifer forest (10). West Latium has vegetation types corresponding to Cropland (0), Mediterranean grasslands and steppes (2), Mediterranean shrublands (sclerophyllous) (4), Deciduous broadleaved shrublands - thermophilus (5), Mesophytic broadleaved forest (9). Whereas North-Sardinia has vegetation types corresponding to pastures (2) and Mediterranean shrublands (sclerophyllous)/ Mediterranean broadleaved forest (4).

Error! Reference source not found.14 shows the confusion matrix based on fuel model for the algorithm. It can be observed from the confusion matrix that the main misclassification has occurred between pastures, grasslands and shrublands. Totally, 70 validation points were correctly classified out of 82 that leads to an overall accuracy of around 85%.

Table 14. Confusion Matrix for field campaign

Number of Points	Fuel Model	(0)	(1)	(2)	(4)	(7)	(9)	(10)
2	Cropland (0)	2	0	0	0	0	0	0
1	Pastures (1)	0	1	0	0	0	0	0
8	Mediterranean grasslands and steppes (2)	0	1	6	1	0	0	0
62	Mediterranean shrublands (sclerophyllous)/ Mediterranean evergreen broadleaved forest (4)	0	0	1	53	2	5	2
2	Shrublands in Mediterranean coniferous forest (7)	0	0	0	0	2	0	0
3	Mesophytic broadleaved forest (9)	0	0	0	0	0	3	0
4	Mesophytic broadleaved forest with conifer forest (10)	0	0	0	0	0	0	3

SYSTEM ARCHITECTURE

6.1. MATLAB based Graphic User Interface

Graphical user interfaces (GUIs), also known as apps, provide point-and-click control of software applications, eliminating the need for others to learn a language or type commands in order to run the application. GUIs can be shared for use within MATLAB and also as standalone desktop or web apps. A good GUI makes an application easy, practical, and efficient to use, and the marketplace success of today's software programs depends on good GUI design.

In this work, Graphic User Interface for the wildfire fuel mapping was developed on MATLAB GUIDE. There are four stages of creating the GUI in MATLAB.

1. Designing the GUI

Prior to start creating GUI, a creative design should be prepared on paper considering the inputs and outputs. In our case, file paths of the georeferenced images extracted from the PRISMA hyperspectral package is to be given. Followingly, details of the spectral signatures including the pixel [X, Y], type of vegetation [Forests / Shrubs / Grasslands], Anderson fuel models [0-10] and Scott / Burgan fuel models [1-256] have to be given.

2. Laying out the GUI

MATLAB GUIDE have provided a blank GUI template with different options such as push button, radio button, edit text, static text etc., which was used to place the required attribute on the template. At the end, a RUN attribute was placed to transfer all the input given for the processing. Call-back functions were programmed in GUI's M-file after the layout was designed. Fig 33 shows the layout that will be used to form the GUI.
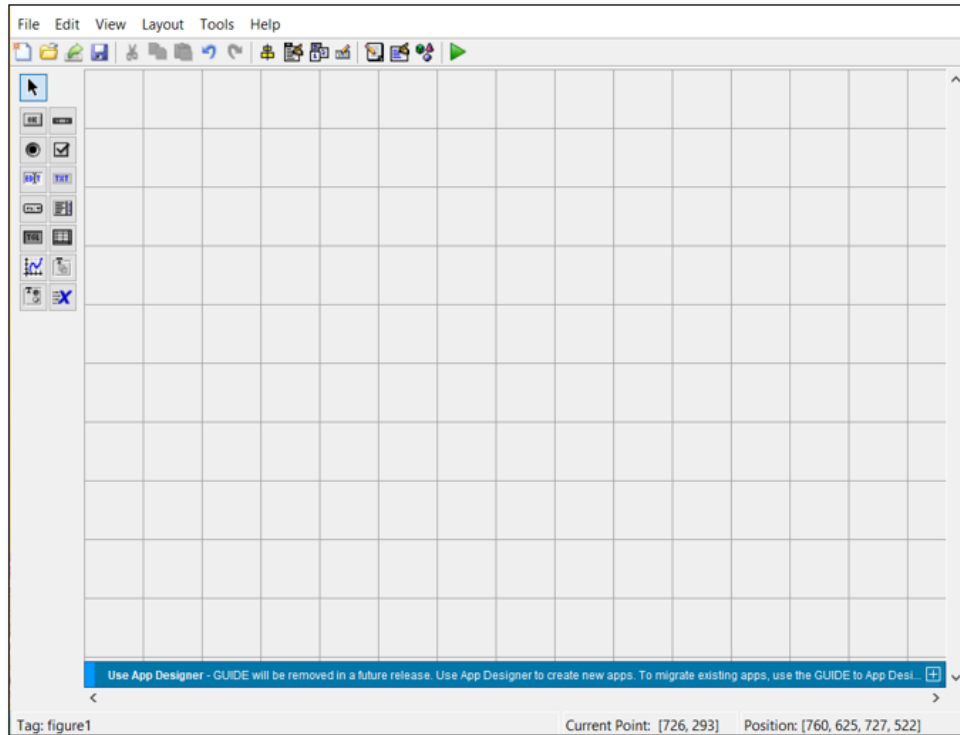
Fig 33. MATLAB GUI Layout

3. Programming the GUI

A *callback* is a sequence of commands that are execute when a graphics object is activated. It is stored in the GUI's M-file and is a property of a graphic object (e.g., CreateFcn, ButtonDwnFcn, Callback, DeleteFcn). This is also called as event handler in some programming languages. Callbacks were programmed after creation of layout to access the inputs from the Graphic User Interface of MATLAB.

4. Saving and Running the GUI

After designing the layout and programming the *callbacks*, layout can be saved and can Run using the developed GUI. Fig 34 shows the MATLAB based GUI developed for mapping wildfire fuel types using PRISMA Hyperspectral Imagery. For better understanding of the inputs to be given in this GUI, a README file as shown in Fig 33, Anderson fuel models chart and Scott/Burgan fuel models chart will be provided in the package.
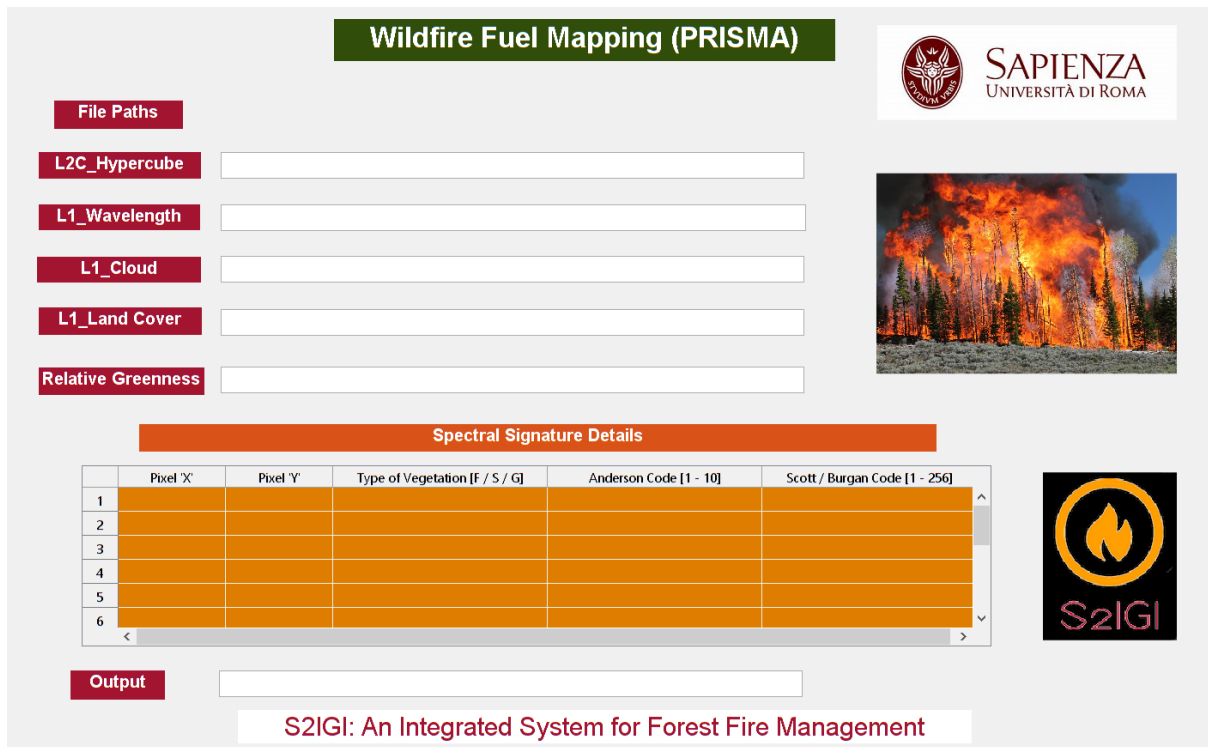
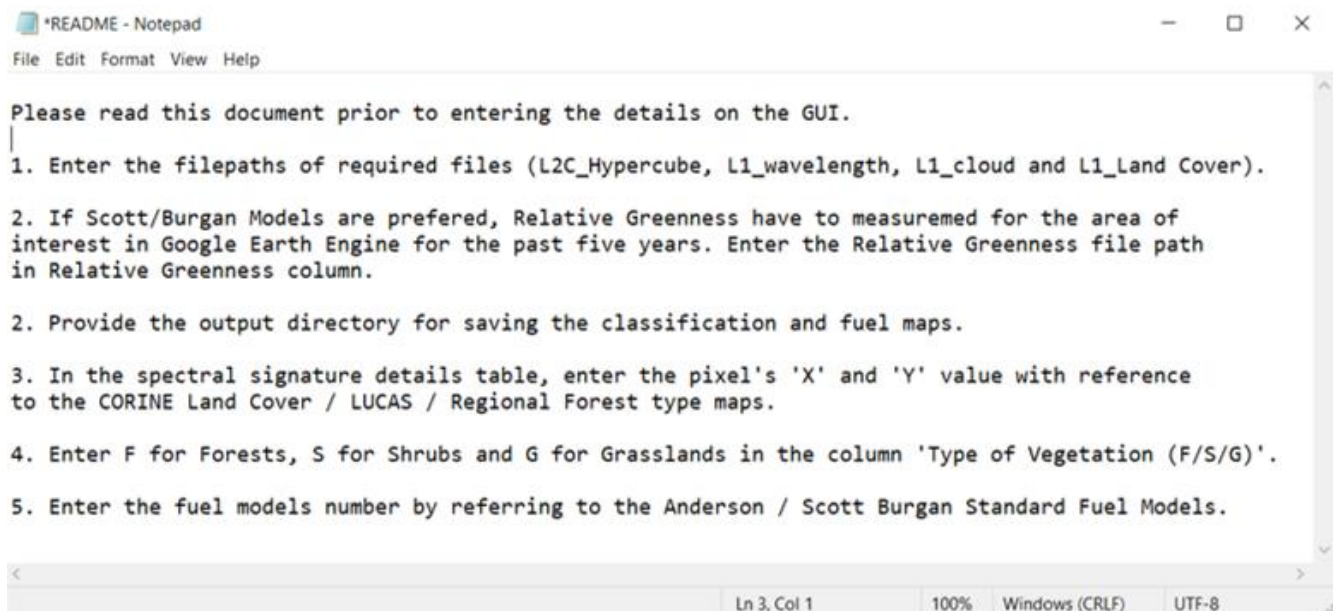*Fig 34. MATLAB based Graphic User Interface for Wildfire Fuel Mapping*

Fig 35. README file for using GUI

SWOT ANALYSIS OF HYPERSPECTRAL REMOTE SENSING FOR WILDFIRE FUEL MAPPING

To conduct a proper SWOT analysis, firstly, the internal and external factor evaluation matrices, IFE and EFE, need to be prepared. Then, a SWOT analysis needs to be conducted based on which the positives and negatives can be understood. In the following, we first explain IFE and EFE and then the SWOT analysis.

The external factors evaluation (EFE) matrix is a tool that allows strategists in urban planning to analyse external factors such as environmental, economic, social, political, cultural and technological factors relevant to a specific issue at a certain period of time. On the other hand, the internal factors evaluation (IFE) matrix is a tool for analysing the internal factors of a city. The matrices are usually developed based on expert opinion and yield an assessment of the opportunities and threats (for EFE), and strengths and weaknesses (for IFE) of a city.

SWOT analysis is an efficient structured method of planning that identifies each factor of strength, weakness, opportunity and threat, and reports the corresponding possible strategies to deal with an issue.

The aim of a SWOT analysis is to classify the main internal and external factors relevant for the issue. In normal mode, the SWOT analysis consists of a 2 × 2 table as shown in Table 14 (SWOT Matrix) and each of its four cells shows a group of strategies with each group targeting an objective as follows:

SWOT analysis is a cognitive process studying the interrelations between internal and external surroundings of a processing, based on a mixed (subjective–objective) evaluation of strengths, weaknesses, opportunities, and threats. Combining these

analysis strategies will serve to provide an exhaustively and updated picture and a detailed assessment of the situation being examined.

Table 15. SWOT Matrix

Technology	Internal	External
	Strengths	*Opportunities*
Positives	- Better accuracy in Fuel Types Classification - Possibility of automation using machine learning - Extension to any part of earth	- Saves time and cost by avoiding field-based fuel types detection - Technology can be transferred between organizations/research labs. - Possibility of image fusion with multispectral, radar, lidar etc.,
	Weaknesses	*Threats*
Negatives	- PRISMA is an on-demand mission and acquisition are not so easy. - The availability of data in archive is limited - Revisiting time of ~16 days. - Long processing time - High computational power is required - Unstable noisy bands - Unstable noisy lines on few bands	- Interdisciplinary knowledge is required for processing. - Lifetime of satellite. - Satellite based environmental issues

7.1. Breakdown of SWOT category

Strengths:

(1) One of the major strengths in using PRISMA hyperspectral imagery is its accuracy in detecting wildfire fuel types in comparison with multispectral imagery. Because of the higher number of bands and with the support of

machine learning, it is possible to detect all the available fuel types in the area of interest with better accuracy.

(2) Since it is a spaceborne data with global coverage, the algorithm developed for one region can be implemented on other parts of world to extract the wildfire fuel types.

(3) By providing the inputs for one specific region, it is possible to automize the procedure for continuous monitoring of forests which could be one of the key strategies for preventing wildfires.

Weaknesses:

(1) PRISMA is an on-demand mission and the acquisition of data for the specific date is not easy due to the high traffic of requests.

(2) Moreover, the availability of data in the archive is limited due to which the analysis cannot be performed for the complete desired region.

(3) The revisiting time of the satellite is ~16 days which is also one of the constraints of this satellite.

(4) Regarding the processing of data, due to the large number of bands (239), the processing carried out using machine learning techniques will take longer hours.

(5) In order to automate the process or for predicting the wildfire fuel types for a complete region, high computation power is required.

(6) Hyperspectral data has unstable noisy bands in the hyper cube.

(7) PRISMA data has dead/noisy lines on some of the bands in the hypercube.

Opportunities:

(1) Though the processing time is longer for hyperspectral data, it is better in comparison with traditional approach of field-based fuel types detection.

(2) Once the algorithm/procedure is developed, it could be transferred between institutions/research centres.

(3) Image fusion with other remote sensing data such as multispectral, radar, lidar etc., can support in extracting wildfires fuel types in more accurately. For examples, Lidar data can help in extracting understory forest vegetation which has high proneness to fire.

Threats:

(1) Prediction of forest fuel types with hyperspectral data is an interdisciplinary field and the personnel employed on this topic have to have interdisciplinary knowledge (about forests, remote sensing data, machine/deep learning etc.,).

(2) Since PRISMA is not a constellation of satellites, is only as single satellite, procedure developed would be useful only till the lifetime of satellite (5 to 7 years) if there is no degradation in sensor.

CONCLUSIONS

This final chapter summarises the goals, methodologies and the most relevant results presented in this thesis. It describes the contributions of this thesis in the prevention and management of wildfires. Finally, it proposes possible lines of research derived from this work.

8.1. Contributions of this Dissertation

Vulnerability Analysis- Vulnerability assessment is of utmost importance in wildfire management and scientific research can provide valuable tools useful in other sectors. In this context, a holistic vulnerability assessment was carried for Sardinian Island of Italy, one of the largest islands of Mediterranean Sea. This work followed a stepwise procedure that allows for local or regional adjustments while maintaining consistent and comparable steps. Also, it provided a set of cartographic tools and different outputs besides the overall vulnerability map, such as exposure maps, environmental sensitivity or coping capacity evaluation, depending on users' needs and considering current institutional procedures. Therefore, the map developed has a strong relevance for fire managers and civil protection activities, contributing to define a systematic evaluation of wildfire vulnerability that can be easily translated into operational practices.

Wildfire Fuel Mapping- In the thesis, wildfire fuel mapping procedure using machine learning on hyperspectral imagery of PRISMA satellite has been put forward. All the necessary fuel types in the image covering the southern part of Sardinian Island were detected. However, there is no suitable dataset or literature available, so a semi-supervised learning approach was proposed for fuel mapping. Support Vector Machine classifier was implemented to identify the fuel types using the posterior probabilities and obtained an Overall Accuracy of 87% by validation. The stability of the procedure and machine learning model was checked by

repeating the same procedure on HSI of PRISMA covering the north of Latium, Italy, and by validation, an Overall Accuracy of 88% was obtained. A degree of confidence greater than 95% was obtained concerning stability analysis for this procedure.

Dynamic Fuel Mapping- A methodology to develop a dynamic wildfire fuel map using PRISMA hyperspectral, Sentinel-2 multispectral data and iso-bioclimatic map was presented. Initially, a fuel types classification map was generated using PRISMA data and then Relative Greenness map was generated using the 5 years' time-series data on Google Earth Engine. Scott/Burgan standard fire behaviour fuel models were referred for converting classified map to dynamic fuel map considering classification and relative greenness map.

System Architecture- Algorithm of wildfire fuel mapping was automated using the MATLAB GUI. In order to provide the input for pixel extraction, LUCAS maps can be referred.

SWOT- SWOT analysis of PRISMA hyperspectral data for wildfire fuel mapping was performed to understand the Strengths, Weaknesses, Opportunities and Threats of this imagery.

8.2. Future Research Developments

This thesis has developed the vulnerability map for Sardinia and automatic procedure of wildfire fuel mapping using PRISMA hyperspectral data for the Europe.

- Further, the vulnerability map of Sardinia can be updated with the fuel map prepared using PRISMA hyperspectral imagery if the satellite can acquire data for the complete Island. All the three components of vulnerability assessment can be improved considering various other dimensions and variables.
- The validation of the outputs and the full implementation of the framework in context-specific areas require further research. The application of efficient fire

prevention and coping strategies depend on robust and consistent evaluations of damage potential.

- Scott / Burgan standard fuel models have some of the fuel types specifically assigned for understory vegetation which is not possible to be predicted using Hyperspectral Imagery. Fusing hyperspectral data with LiDAR data can predict both overstorey and understorey vegetation.

- An interlink between overstorey vegetation, climatic condition and understorey vegetation can be formed to predict the understorey vegetation using hyperspectral data and iso-bioclimatic map.

REFERENCES

Anderson. 1982. "Fire Behavior Fuel Model Descriptions." *Fire and Fuels*, B-1-B-7.

A.A Ager, M.A. Day, C.W. McHugh, K. Short, J. Gilbertson-Day, M.A. Finney, D.E. Calkin Wildfire exposure and fuel management on western US national forests J. Environ. Manage., 145 (2014), pp. 54-70, 10.1016/j.jenvman. 2014.05.035

Alexandra stefanidou, Ioannis Z. Gitas & Thomas katagis (2020). A national fuel type mapping method improvement using Sentinel-2 satellite data, Geocarto International, DOI: 10.1080/10106049.2020.1756460

Arbez, Michel., Yves. Birot, and Jean-Michel. Carnus. 2002. *Risk Management and Sustainable Forestry: Bordeaux, France, 8 September 2001*. European Forest Institute.

Aretano, Roberta, Teodoro Semeraro, Irene Petrosillo, Antonella de Marco, Maria Rita Pasimeni, and Giovanni Zurlini. 2015. "Mapping Ecological Vulnerability to Fire for Effective Conservation Management of Natural Protected Areas." *Ecological Modelling* 295 (January). Elsevier: 163–75. doi:10.1016/j.ecolmodel.2014.09.017.

Arroyo, Lara A., Cristina Pascual, and José A. Manzanera. 2008. "Fire Models and Methods to Map Fuel Types: The Role of Remote Sensing." *Forest Ecology and Management*. doi:10.1016/j.foreco.2008.06.048.

Atiya Khan, Amol D. Vibhute, Shankar Mali, C.H. Patil, A systematic review on hyperspectral imaging technology with a machine and deep learning methodology for agricultural applications, Ecological Informatics, Volume 69, 2022, 101678, ISSN 1574-9541, https://doi.org/10.1016/j.ecoinf.2022.101678.

Badola, Anushree, Santosh K. Panda, Dar A. Roberts, Christine F. Waigl, Uma S. Bhatt, Christopher W. Smith, and Randi R. Jandt. 2021. "Hyperspectral Data

Simulation (Sentinel-2 to Aviris-Ng) for Improved Wildfire Fuel Mapping, Boreal Alaska." *Remote Sensing* 13 (9). MDPI AG. doi:10.3390/rs13091693.

Birkmann, J., O. D. Cardona, M. L. Carreño, A. H. Barbat, M. Pelling, S. Schneiderbauer, S. Kienberger, et al. 2013a. "Framing Vulnerability, Risk and Societal Responses: The MOVE Framework." *Natural Hazards* 67 (2). Kluwer Academic Publishers: 193–211. doi:10.1007/s11069-013-0558-5.

Birkmann J Cardona. 2013b. "Framing Vulnerability, Risk and Societal Responses: The MOVE Framework." *Natural Hazards* 67 (2). Kluwer Academic Publishers: 193–211. doi:10.1007/s11069-013-0558-5.

Boer, Matthias M., Craig Macfarlane, Jaymie Norris, Rohan J. Sadler, Jeremy Wallace, and Pauline F. Grierson. 2008. "Mapping Burned Areas and Burn Severity Patterns in SW Australian Eucalypt Forest Using Remotely-Sensed Changes in Leaf Area Index." *Remote Sensing of Environment* 112 (12): 4358–69. doi:10.1016/j.rse.2008.08.005.

Bonazountas, M., A. Astyakopoulos, G. Martirano, A Sebastian, D. de la Fuente, L.M. Ribeiro, D.X. Viegas, G. Eftychidis, I. Gitas, and P. Toukiloglou. 2014. "LIFE ArcFUEL: Mediterranean Fuel-Type Maps Geodatabase for Wildland & Forest Fire Safety." In *Advances in Forest Fire Research*, 1723–35. Imprensa da Universidade de Coimbra. doi:10.14195/978-989-26-0884-6_189.

Bond, William J., and Jon E. Keeley. 2005. "Fire as a Global 'Herbivore': The Ecology and Evolution of Flammable Ecosystems." *Trends in Ecology and Evolution*. doi:10.1016/j.tree.2005.04.025.

Bowman, David M J S, Jennifer K Balch, Paulo Artaxo, William J Bond, Jean M Carlson, Mark A Cochrane, Carla M d'Antonio, et al. 2009. "Fire in the Earth System." https://www.science.org.

Bowman, David M.J.S., Jennifer Balch, Paulo Artaxo, William J. Bond, Mark A. Cochrane, Carla M. D'Antonio, Ruth Defries, et al. 2011. "The Human Dimension of Fire Regimes on Earth." *Journal of Biogeography*. doi:10.1111/j.1365-2699.2011.02595.x.

Burgan, R.; Klaver, R.W.; Klaver, J.M. Fuel models and fire potential from satellite and surface observations. Int. J. Wildland Fire 1998, 8, 159–170.

Büttner, György, Barbara Kosztra, Gergely Maucha, Róbert Pataki, Stefan Kleeschulte, Gerard Hazeu, Marian Vittek, and Andreas Littkopf. n.d. "Copernicus Land Monitoring Service CORINE Land Cover User Manual CORINE Land Cover Product User Manual (Version 1.0) Lead Service Provider for Data Production: NT (National Teams) within EIONET National Reference Centres Land Cover (NRC) with Support from EEA/ETC ULS (European Environment Agency/European Topic Centre Urban Land and Soil) User Manual Prepared By." https://land.copernicus.eu/.

Caudullo, G., S. Pasta, F. Giannetti, A. Barbati, and G. Chirici. 2016. "European Forest Classifications." *European Atlas of Forest Tree Species.*

Cervantes, Jair, Farid Garcia-Lamont, Lisbeth Rodríguez-Mazahua, and Asdrubal Lopez. 2020. "A Comprehensive Survey on Support Vector Machine Classification: Applications, Challenges and Trends." *Neurocomputing*, no. xxxx. Elsevier B.V. doi:10.1016/j.neucom.2019.10.118.

Chang, Chein-I. 2004. "New Hyperspectral Discrimination Measure for Spectral Characterization." *Optical Engineering* 43 (8). SPIE-Intl Soc Optical Eng: 1777. doi:10.1117/1.1766301.

Cutter, Mike A. 2006. "A Small Satellite Hyper-Spectral Mission." *JBIS - Journal of the British Interplanetary Society* 59 (5): 153–57.

Cutter, Susan L. 2011. "A Ciência Da Vulnerabilidade: Modelos, Métodos e Indicadores." *Revista Crítica de Ciências Sociais*, no. 93 (June). OpenEdition: 59–69. doi:10.4000/rccs.165.

Dalponte, Michele, Lorenzo Bruzzone, Loris Vescovo, and Damiano Gianelle. 2009. "The Role of Spectral Resolution and Classifier Complexity in the Analysis of Hyperspectral Images of Forest Areas." *Remote Sensing of Environment* 113 (11): 2345–55. doi:10.1016/j.rse.2009.06.013.

Dennison, Philip E., Kraivut Charoensiri, Dar A. Roberts, Seth H. Peterson, and Robert O. Green. 2006. "Wildfire Temperature and Land Cover Modeling Using Hyperspectral Data." *Remote Sensing of Environment* 100 (2): 212–22. doi:10.1016/j.rse.2005.10.007.

Duguy, Beatriz, José Antonio Alloza, M. Jaime Baeza, Juan de La Riva, Maite Echeverría, Paloma Ibarra, Juan Llovet, Fernando Pérez Cabello, Pere Rovira, and Ramon v. Vallejo. 2012. "Modelling the Ecological Vulnerability to Forest Fires in Mediterranean Ecosystems Using Geographic Information Technologies." *Environmental Management* 50 (6): 1012–26. doi:10.1007/s00267-012-9933-3.

Duveau, Sophie. 2021. "Frozen Data? Polar Research and Fieldwork in a Pandemic Era." *Polar Record* 57. Cambridge University Press (CUP). doi:10.1017/s0032247421000541.

F., Martini, Ronconi D., Onder G., Liperoti R., and Bernabei R. 2017. "Guided Image Filtering Kaiming." *European Geriatric Medicine* 8: S69. http://www.embase.com/search/results?subaction=viewrecord&from=export&id=L618532105.

F.J. Alcasena, M. Salis, A.A. Ager, B. Arca, D. Molina, D. Spano Assessing landscape-scale wildfire exposure for highly valued resources in a Mediterranean area Environ. Manage., 55(2015), pp. 1200 – 1216,

G. F. Hughes. 1968. "On the Mean Accuracy of Statistical Pattern Recognizers. Information Theory." *IEEE Transactions*, 55–63.

Gewali, Utsav B., Sildomar T. Monteiro, and Eli Saber. 2018. "Machine Learning Based Hyperspectral Image Analysis: A Survey," February. http://arxiv.org/abs/1802.08701.

Ghorbanzadeh, O., Blaschke, T., Gholamnia, K., Aryal, J., 2019. Forest Fire Susceptibility and Risk Mapping Using Social/Infrastructural Vulnerability and Environmental Variables. Fire 2. https://doi.org/10.3390/fire2030050

Glenn J. Newnham, Jan Verbesselt, Ian F. Grant, Stuart A.J. Anderson, Relative Greenness Index for assessing curing of grassland fuel, Remote Sensing of Environment, Volume 115, Issue 6, 2011, Pages 1456-1463, ISSN 0034-4257, https://doi.org/10.1016/j.rse.2011.02.005.

Global Development Lab, Us. n.d. "Guide for Adopting Remote Monitoring Approaches During COVID-19."

Goodenough, David G., Andrew Dyk, K. Olaf Niemann, Jay S. Pearlman, Hao Chen, Tian Han, Matthew Murdoch, and Chris West. 2003. "Processing Hyperion and ALI for Forest Classification." *IEEE Transactions on Geoscience and Remote Sensing* 41 (6 PART I): 1321–31. doi:10.1109/TGRS.2003.813214.

Guo, Yanhui, Xijie Yin, Xuechen Zhao, Dongxin Yang, and Yu Bai. 2019. "Hyperspectral Image Classification with SVM and Guided Filter." *Eurasip Journal on Wireless Communications and Networking* 2019 (1). EURASIP Journal on Wireless Communications and Networking. doi:10.1186/s13638-019-1346-z.

He, Kaiming, Jian Sun, and Xiaoou Tang. 2012. "Guided Image Filtering (Presentation)." *2012 European Confenrence on Computer Vision*, no. 7: 1–14.

He K, Sun J. 2013. "Guided Image Filtering." *IEEE Transactions on Pattern Analysis and Machine Intelligence* 35 (6): 1397–1409. doi:10.1109/TPAMI.2012.213.

Heinz, D., C.-I. Chang, and M.L.G. Althouse. 2003. "Fully Constrained Least-Squares Based Linear Unmixing [Hyperspectral Image Classification]." In , 1401–3. Institute of Electrical and Electronics Engineers (IEEE). doi:10.1109/igarss.1999.774644.

J. A. Richards, and X. Jia. 2006. "Remote Sensing Digital Image Analysis: An Introduction." *Springer-Verlag Berlin Heidelberg, Berlin Heidelberg, 4th Edition.*

J. R. Schott. 2007. "Remote Sensing: The Image Chain Approach."

J, San-Miguel-Ayanz, Durrant T, Boca R, Maianti P, Liberta' G, Artes Vivancos T, Jacome Felix Oom D, et al. 2021. "Forest Fires in Europe, Middle East and North Africa 2020," no. KJ-NA-30862-EN-N (online),KJ-NA-30862-EN-C (print). Luxembourg (Luxembourg): Publications Office of the European Union. doi:10.2760/216446 (online),10.2760/059331 (print).

Jain, Theresa B, Graham, Russell T, Pilliod, and David S. 2004. "Tongue-Tied: Confused Meanings for Common Fire Terminology Can Lead to Fuels Mismanagement." www.wildfiremag.com.

Jawak, Shridhar D., Bo N. Andersen, Veijo Pohjola, Øystein Godøy, Christiane Hübner, Inger Jennings, Dariusz Ignatiuk, et al. 2021. "Sios's Earth Observation (Eo), Remote Sensing (Rs), and Operational Activities in Response to Covid-19." *Remote Sensing* 13 (4). MDPI AG: 1–31. doi:10.3390/rs13040712.

Jones, Petra J., Matthew K. James, Melanie J. Davies, Kamlesh Khunti, Mike Catt, Tom Yates, Alex v. Rowlands, and Evgeny M. Mirkes. 2020. "FilterK: A New

Outlier Detection Method for k-Means Clustering of Physical Activity." *Journal of Biomedical Informatics* 104 (October 2019). Elsevier: 103397. doi:10.1016/j.jbi.2020.103397.

Kang, Xudong, Shutao Li, and Jon Atli Benediktsson. 2014. "Spectral-Spatial Hyperspectral Image Classification with Edge-Preserving Filtering." *IEEE Transactions on Geoscience and Remote Sensing* 52 (5). Institute of Electrical and Electronics Engineers Inc.: 2666–77. doi:10.1109/TGRS.2013.2264508.

Keeley, Jon E. 2009. "Fire Intensity, Fire Severity and Burn Severity: A Brief Review and Suggested Usage." *International Journal of Wildland Fire* 18 (1): 116–26. https://doi.org/10.1071/WF07049.

Keramitsoglou, Iphigenia, Chris T. Kiranoudis, Haralambos Sarimveis, and Nicolaos Sifakis. 2004. "A Multidisciplinary Decision Support System for Forest Fire Crisis Management." *Environmental Management* 33 (2): 212–25. doi:10.1007/s00267-003-0092-4.

L. Bruzzone, and B. Demir. 2014. "A Review of Modern Approaches to Classification of Remote Sensing Data." In *Land Use and Land Cover Mapping in Europe*, 18:127–43. Springer Netherlands,.

L. Mossa, G. Bacchetta, C. Angiolino, and M. Ballero. 2016. "A Contribution to the Floristic Knowledge of the Monti Del Sulcis: Monte Arcosu (S. W. Sardinia)." *Flora Mediterranea* 6.

Laliberte, A. S., D. M. Browning, and A. Rango. 2012. "A Comparison of Three Feature Selection Methods for Object-Based Classification of Sub-Decimeter Resolution UltraCam-L Imagery." *International Journal of Applied Earth Observation and Geoinformation* 15 (1). Elsevier B.V.: 70–78. doi:10.1016/j.jag.2011.05.011.

Laneve, Giovanni, Valerio Pampanoni, and Riyaaz Uddien Shaik. 2020. "The Daily Fire Hazard Index: A Fire Danger Rating Method for Mediterranean Areas." *Remote Sensing* 12 (15). MDPI AG. doi:10.3390/RS12152356.

Lentile, Leigh B., Zachary A. Holden, Alistair M.S. Smith, Michael J. Falkowski, Andrew T. Hudak, Penelope Morgan, Sarah A. Lewis, Paul E. Gessler, and Nate C. Benson. 2006. "Remote Sensing Techniques to Assess Active Fire Characteristics and Post-Fire Effects." *International Journal of Wildland Fire*. doi:10.1071/WF05097.

Manolakis, D., C. Siracusa, and G. Shaw. 2001. "Hyperspectral Subpixel Target Detection Using the Linear Mixing Model." *IEEE Transactions on Geoscience and Remote Sensing* 39 (7): 1392–1409. doi:10.1109/36.934072.

Maxwell, Aaron E., Timothy A. Warner, and Fang Fang. 2018. "Implementation of Machine-Learning Classification in Remote Sensing: An Applied Review." *International Journal of Remote Sensing*. Taylor and Francis Ltd. doi:10.1080/01431161.2018.1433343.

Morgan, Penelope, Robert E. Keane, Gregory K. Dillon, Theresa B. Jain, Andrew T. Hudak, Eva C. Karau, Pamela G. Sikkink, Zachary A. Holden, and Eva K. Strand. 2014. "Challenges of Assessing Fire and Burn Severity Using Field Measures, Remote Sensing and Modelling." *International Journal of Wildland Fire* 23 (8). CSIRO: 1045–60. doi:10.1071/WF13058.

M.P. Thompson, J. Scott, J.D. Kaiden, J.W. Gilbertson-Day A polygon-based modeling approach t assess the exposure of resources and assets to wildfire Nat. Hazards, 67 (2013), pp. 627-644,

M.P. Thompson, J.R. Haas, J.W. Gilbertson-Day, J.H. Scott, P. Langowski, E. Bowne, D.E. Calkin Development and application of a geospatial wildfire exposure and risk calculation tool Environ. Model. Softw., 63 (2015), pp. 61 – 72,

M. Salis, A.A. Ager, B. Arca, M.A. Finney, V. Bacciu, P. Duce, D. Spano Assessing exposure of human and ecological values to wildfire in Sardinia, Italy Int. J. Wildl. Fire, 22 (2013), pp. 549-565,

M. Salis, A.A. Ager, F.J. Alcasena, B. Arca, M.A.Finney, G. Pellizzaro, D. Spano Analyzing seasonal patterns of wildfire exposure factors in Sardinia, Italy Environ. Monit. Assess., 187 (2015), pp. 1-20,

Niroumand-jadidi, Milad, Francesca Bovolo, and Lorenzo Bruzzone. 2020. "Water Quality Retrieval from PRISMA Hyperspectral Images : First Experience in a Turbid Lake and Comparison with Sentinel-2."

Oliveira, S. Felix, F. Nunes, A., Lourenco, L., Laneve, G., Sebastian-Lopex, A., 2018. Mapping wildfire vulnerability in Mediterranean Europe. Testing a stepwise approach for operational purposes. Journal of Environmental Management 206, 158-169. https://doi.org/10.1016/j.jenvman.2017.10.003

Padma, S., and S. Sanjeevi. 2014. "Jeffries Matusita Based Mixed-Measure for Improved Spectralmatching in Hyperspectral Image Analysis." *International Journal of Applied Earth Observation and Geoinformation* 32 (1). Elsevier B.V.: 138–51. doi:10.1016/j.jag.2014.04.001.

Parsons, Annette, Peter R Robichaud, Sarah A Lewis, Carolyn Napper, and Jess T Clark. 2010. "Field Guide for Mapping Post-Fire Soil Burn Severity." http://www.fs.fed.us/rmrs.

Pepe, Monica, Loredana Pompilio, Beniamino Gioli, Lorenzo Busetto, and Mirco Boschetti. 2020. "Detection and Classification of Non-Photosynthetic Vegetation from Prisma Hyperspectral Data in Croplands." *Remote Sensing*. MDPI AG. doi:10.3390/rs12233903.

Pettinari, M. Lucrecia, and Emilio Chuvieco. 2016. "Generation of a Global Fuel Data Set Using the Fuel Characteristic Classification System." *Biogeosciences* 13 (7). Copernicus GmbH: 2061–76. doi:10.5194/bg-13-2061-2016.

R. A. Schowengerdt. 2007. "Remote Sensing: Models and Methods for Image Processing."

Rodrigues, Marcos, Sandra Oliveira, Francisco Moreira, Jesús San Miguel, and Andrea Camia. 2013. "An Insight into Spatial-Temporal Trends of Fire Ignitions and Burned Areas in the European Mediterranean Countries PREDFIRE: Climate Monitoring and PREDictions to Forecast Global FIRE Activity View Project PERIURBAN-PERI-URBAN AREAS FACING SUSTAINABILITY CHALLENGES: SCENARIO DEVELOPMENT IN THE METROPOLITAN AREA OF LISBON View Project An Insight into Spatial-Temporal Trends of Fire Ignitions and Burned Areas in the European Mediterranean Countries." *Journal of Earth Science and Engineering*. Vol. 3. https://www.researchgate.net/publication/261355556.

Rodríguez Silva, Francisco, Juan Ramón Molina Martínez, and Miguel Castillo Soto. 2012. "Methodological Approach for Assessing the Economic Impact of Forest Fires Using MODIS Remote Sensing Images 1."

Román, María Victoria, Diego Azqueta, and Marcos Rodrígues. 2013. "Methodological Approach to Assess the Socio-Economic Vulnerability to Wildfires in Spain." *Forest Ecology and Management* 294 (April): 158–65. doi:10.1016/j.foreco.2012.07.001.

Sabat-Tomala, Anita, Edwin Raczko, and Bogdan Zagajewski. 2020. "Comparison of Support Vector Machine and Random Forest Algorithms for Invasive and Expansive Species Classification Using Airborne Hyperspectral Data." *Remote Sensing* 12 (3). doi:10.3390/rs12030516.

San-Miguel-Ayanz, Jesús., Tracy. Durrant, Roberto. Boca, Giorgio. Libertà, Alfredo. Branco, Daniele. de Rigo, Davide. Ferrari, et al. n.d. *Advance EFFIS Report on Forest Fires in Europe, Middle East and North Africa 2017.*

Santarsiero, Valentina, Gabriele Nolè, Antonio Lanorte, Biagio Tucci, Giuseppe Cillis, Francesco Scorza, and Beniamino Murgante. 2021. "A Remote Sensing Methodology to Assess the Abandoned Arable Land Using NDVI Index in Basilicata Region." In *Computational Science and Its Applications – ICCSA 2021,* edited by Osvaldo Gervasi, Beniamino Murgante, Sanjay Misra, Chiara Garau, Ivan Blečić, David Taniar, Bernady O Apduhan, Ana Maria A C Rocha, Eufemia Tarantino, and Carmelo Maria Torre, 695–703. Cham: Springer International Publishing.

Scott, Joe H., and Robert E. Burgan. 2005a. "Standard Fire Behavior Fuel Models: A Comprehensive Set for Use with Rothermel's Surface Fire Spread Model." *USDA Forest Service - General Technical Report RMRS-GTR*, no. 153 RMRS-GTR: 1–76. doi:10.2737/RMRS-GTR-153.

Scott, Joe H, and Robert E Burgan. 2005b. "Standard Fire Behavior Fuel Models: A Comprehensive Set for Use with Rothermel's Surface Fire Spread Model." http://www.fs.fed.us/rm/publications.

Smith, Christopher William, Santosh K. Panda, Uma Suren Bhatt, and Franz J. Meyer. 2021. "Improved Boreal Forest Wildfire Fuel Type Mapping in Interior Alaska Using Aviris-Ng Hyperspectral Data." *Remote Sensing* 13 (5). MDPI AG: 1–15. doi:10.3390/rs13050897.

Stavros, E. Natasha, John T. Abatzoglou, Donald McKenzie, and Narasimhan K. Larkin. 2014. "Regional Projections of the Likelihood of Very Large Wildland Fires under a Changing Climate in the Contiguous Western United States."

Climatic Change 126 (3–4). Kluwer Academic Publishers: 455–68. doi:10.1007/s10584-014-1229-6.

Susan L. Cutter. 2015. "Pool Knowledge to Stem Losses from Disasters." *NATURE* 522.

Thai, Le Hoang, Tran Son Hai, and Nguyen Thanh Thuy. 2012. "Image Classification Using Support Vector Machine and Artificial Neural Network." *International Journal of Information Technology and Computer Science* 4 (5): 32–38. doi:10.5815/ijitcs.2012.05.05.

Toukiloglou, Pericles, George Eftychidis, Ioannis Gitas, and Maria Tompoulidou. 2013a. "ArcFuel Methodology for Mapping Forest Fuels in Europe." *First International Conference on Remote Sensing and Geoinformation of the Environment (RSCy2013)* 8795 (August): 87951J. doi:10.1117/12.2028213.

Toukiloglou, Pericles, George Eftychidis, Ioannis Gitas, and Maria Tompoulidou. 2013b. "ArcFuel Methodology for Mapping Forest Fuels in Europe." In *First International Conference on Remote Sensing and Geoinformation of the Environment (RSCy2013)*, 8795:87951J. SPIE. doi:10.1117/12.2028213.

Tucci, Biagio, Gabriele Nolè, Antonio Lanorte, Valentina Santarsiero, Giuseppe Cillis, Francesco Scorza, and Beniamino Murgante. 2021. "Assessment and Monitoring of Soil Erosion Risk and Land Degradation in Arable Land Combining Remote Sensing Methodologies and RUSLE Factors." In *Computational Science and Its Applications – ICCSA 2021*, edited by Osvaldo Gervasi, Beniamino Murgante, Sanjay Misra, Chiara Garau, Ivan Blečić, David Taniar, Bernady O Apduhan, Ana Maria A C Rocha, Eufemia Tarantino, and Carmelo Maria Torre, 704–16. Cham: Springer International Publishing.

Uddien Shaik, Riyaaz, Laneve Giovanni, and Lorenzo Fusilli. 2021. "New Approach of Sample Generation and Classification for Wildfire Fuel Mapping on

Hyperspectral (Prisma) Image; New Approach of Sample Generation and Classification for Wildfire Fuel Mapping on Hyperspectral (Prisma) Image." doi:10.1109/IGARSS47720.2021.9554652.

United Nations. 2015. "Marco de Sendai Para La Reducción Del Riesgo de Desastres 2015-2030."

Vakalis, D., H. Sarimveis, C. Kiranoudis, A. Alexandridis, and G. Bafas. 2004a. "A GIS Based Operational System for Wildland Fire Crisis Management I. Mathematical Modelling and Simulation." *Applied Mathematical Modelling* 28 (4). Elsevier Inc.: 389–410. doi:10.1016/j.apm.2003.10.005.

Vakalis, D., H. Sarimveis, C. T. Kiranoudis, A. Alexandridis, and G. Bafas. 2004b. "A GIS Based Operational System for Wildland Fire Crisis Management II. System Architecture and Case Studies." *Applied Mathematical Modelling* 28 (4). Elsevier Inc.: 411–25. doi:10.1016/j.apm.2003.10.006.

Veraverbeke, Sander, Philip Dennison, Ioannis Gitas, Glynn Hulley, Olga Kalashnikova, Thomas Katagis, Le Kuai, Ran Meng, Dar Roberts, and Natasha Stavros. 2018a. "Hyperspectral Remote Sensing of Fire: State-of-the-Art and Future Perspectives." *Remote Sensing of Environment*. Elsevier Inc. doi:10.1016/j.rse.2018.06.020.

———. 2018b. "Hyperspectral Remote Sensing of Fire: State-of-the-Art and Future Perspectives." *Remote Sensing of Environment*. Elsevier Inc. doi:10.1016/j.rse.2018.06.020.

———. 2018c. "Hyperspectral Remote Sensing of Fire: State-of-the-Art and Future Perspectives." *Remote Sensing of Environment*. Elsevier Inc. doi:10.1016/j.rse.2018.06.020.

Vishnu, Sennaraj, Rama Rao Nidamanuri, and R. Bremananth. 2013. "Spectral Material Mapping Using Hyperspectral Imagery: A Review of Spectral

Matching and Library Search Methods." *Geocarto International*. doi:10.1080/10106049.2012.665498.

Wei, Jiaojiao, and Xiaofei Wang. 2020. "An Overview on Linear Unmixing of Hyperspectral Data." *Mathematical Problems in Engineering*. Hindawi Limited. doi:10.1155/2020/3735403.

Werf, Guido R. van der, James T. Randerson, Louis Giglio, Thijs T. van Leeuwen, Yang Chen, Brendan M. Rogers, Mingquan Mu, et al. 2017. "Global Fire Emissions Estimates during 1997-2016." *Earth System Science Data*. Copernicus GmbH. doi:10.5194/essd-9-697-2017.

Whelan, Robert J. 2009. "The Ecology of Fire-Developments since 1995 and Outstanding Questions Long-Term Trends in Flowering and Fruit Set in Banksia View Project Pollination of Diuris (Orchidaceae) View Project." https://www.researchgate.net/publication/30387859.

Wooster, Martin J., G. Roberts, G. L.W. Perry, and Y. J. Kaufman. 2005. "Retrieval of Biomass Combustion Rates and Totals from Fire Radiative Power Observations: FRP Derivation and Calibration Relationships between Biomass Consumption and Fire Radiative Energy Release." *Journal of Geophysical Research Atmospheres* 110 (24). Blackwell Publishing Ltd: 1–24. doi:10.1029/2005JD006318.

Yeosang Yoon, and Yongseung Kim. 2007. "Application of Hyperion Hyperspectral Remote Sensing Data for Wildfire Fuel Mapping." *Korean Journal of Remote Sensing* 23 (1): 21–32. https://www.koreascience.or.kr/article/JAKO200712242534560.pdf.